3D Additive Manufacturing: Microstructural Evolution of HSLA Steel in WAAM process

KUO-HAO (Howard) WU

TU Delft

3D Additive Manufacturing: Microstructural Evolution of HSLA Steel in WAAM process

By

KUO-HAO (Howard) WU

in partial fulfilment of the requirements for the degree of

Master of Science
in Materials Science and Engineering

at the Delft University of Technology,
to be defended publicly on Wednesday November 25, 2020 at 02:00 PM.

Thesis committee:	Prof. dr. ir. Marcel Hermans,	TU Delft
	Ir. Aravind Babu,	TU Delft
	Prof. dr. ir. Can Ayas,	TU Delft

TU Delft

Abstract

This research mainly investigates the relationship between the process condition, the microstructural evolution and the mechanical properties of the low carbon S690 steel in complex WAAM deposited structures. Besides, the optimum process parameters for improving the quality of the multi-pass multi-layer structure are also the research topic in the thesis.

With a decreased heat input, achieved by a higher travel speed or a lower wire feed rate, the cooling rate became higher in the single bead. A larger amount of martensite formed in the bead due to the higher cooling rate, which led to a higher hardness. When the heat input became smaller, less metal was deposited per unit length, which decreased both the width and the height of the bead.

Two-layers structures were deposited with the different process parameters, and their qualities were evaluated based on defects, surface roughness, and geometry. Step over increments were set to two-thirds of the width of each bead to improve the surface quality. Wire feed rate 4.5 m/min and travel speed 8 mm/s are the optimized parameters to fabricate the sample with the highest quality.

Functional grading was achieved in a component by depositing with different process conditions. In the functionally graded component, the high heat input zone, having a lower hardness, included a large fraction of ferrite and bainite because it was fabricated with higher heat input, resulting in the lower cooling rate. The low heat input zone, having a higher hardness, included a large fraction of martensite due to higher cooling rate, caused by the lower heat input. The microstructure in the low heat input zone was not homogeneous due to the occurrence of the softer white line region, including a large amount of ferrite.

The crossing structures fabricated with the interlayer temperature of 100 °C and the interlayer time of 90 sec showed the similar microstructures and hardness result. Due to the impact of a cold substrate and thermal accumulation, the varying microstructure existed from the bottom region to the top region, leading to the hardness level along the building direction became: Bottom region > Middle region ≈ Top region. The higher cooling rate at the centre was observed because there was more area for heat produced at the centre to diffuse.

Keywords: Wire arc additive manufacturing (WAAM), Low carbon steel, Microstructure, Mechanical properties

Acknowledgement

First and foremost, I would like to express my sincerest gratitude to my supervisors Prof. dr. ir. Marcel Hermans and Ir. Aravind Babu for leading me into the fantastic world of materials science. They have been so inspirational and gave me the freedom to work on my interested areas. Not only have I acquired professional knowledge from them, but I have also obtained the skill for cooperating with other experts in a team. Being a member in Joining and Additive Manufacturing team is definitely the most memorable experience in my life.

Many thanks to Prof. dr. ir. Can Ayas. He provided me with good suggestions and feedback for my experiments. I have also learnt how to solve the scientific problems during the discussion with him. I would also like to thank Rutger Schreurs. All methodology and the result of the thermal simulation in this thesis have been designed and provided by Rutger Schreurs. He introduced me to the application of thermal simulations in additive manufacturing. With the simulation, this thesis became more complete.

Special thanks should be given to Remko Seijffers. The experiments have been done smoothly and safely with his assistance. He was always willing to offer great suggestions when I met some problems in the laboratory.

Finally, I must express my deepest thankfulness to my family for their unconditional love and continuous support. This journey would not have been possible without the support of my family.

Contents

1 Introduction

1.1. Additive manufacturing

Additive manufacturing (AM) processes build 3D components by progressively adding materials guided by a digital model, allowing that production of complex or customized parts is directly from the design without the need for expensive processes such as punches, dies or casting molds and the need for more conventional processing steps [1].

AM can be classified in seven groups: (a) VAT Photopolymerisation: A vat of liquid photopolymer resin is cured via selective exposure to light which then initiates polymerization and converts the exposed areas to a solid part. (b) Powder Bed Fusion: Powdered materials are selectively consolidated by melting it together by laser or electron beam. (c) Material Jetting: Droplets of material are deposited layer by layer to make components. (d) Binder Jetting: Liquid bonding agents are selectively applied onto thin layers of powdered material to make parts layer by layer. (e) Material Extrusion: Material is extruded through a nozzle or an orifice in tracks or beads, which are then combined into multi-layer components. (f) Sheet Lamination: Sheets of material are stacked and laminated together to form a component. The lamination method can be adhesives or chemical, ultrasonic welding, or brazing. (g) Directed Energy Deposition: In the directed Energy Deposition process, the feedstock, which is in a form of powder or wire, is going through a feed nozzle where it is melted by a energy source (laser, electron beam or arc) and successively added onto the working platform [2].

1.2. Wire and arc additive manufacturing

WAAM is a technology which combines an electric arc (heat source) and a wire (feedstock material), to deposit large and complex parts. WAAM includes the fundamental concepts of automatized or robotized processes and arc welding processes such as gas metal arc welding (GMAW) and gas tungsten arc welding (GTAW) [3].

Gas Metal Arc Welding (GMAW) is created by an electric arc welding process producing coalescence of metallic materials by heating them with an arc between a continuous filler metal electrode and the work-piece. Shielding from atmospheric contamination is obtained entirely from an externally supplied shielding gas [4]. GMAW can be used to weld all commercially important metals, including steel, aluminium, copper, and stainless steel. The GMAW process can be utilized to weld in any position, including flat, vertical, and horizontal. It's usually connected to use direct current electrode positive (DCEP) [4].

Gas tungsten arc welding (GTAW), also known as tungsten inert gas (TIG) welding, is an arc welding process that uses a non-consumable tungsten electrode. The weld area and electrode are protected from oxidation or other atmospheric contamination by an inert shielding gas, and a filler metal is normally used,

though some welds, known as autogenous welds, do not require it. As helium is applied, it is known as heliarc welding. A constant-current welding power supply produces electrical energy, and it is conducted across the arc through a column of highly ionized gas and metal vapours known as a plasma [5].

1.3. S690 steel

S690 steel is a low-carbon low-alloy high strength steel, and it is typically applied in structures bearing high loads. Moreover, S690 steel has an excellent balance of strength and toughness, which can be achieved by quenching and tempering processes in steels. After prior heat treatment processes, the steel is quenched to the room temperature and tempered below the eutectoid temperature. The fine grains steel can be characterized by a high hardness and strength [6][7].

S690 steel has a minimum yield strength 690 N/mm², which is around two to three times the yield strength of commonly used structural steel materials. Because of the high strength-to-weight ratio, S690 steel is one of the most suitable materials for heavily loaded structures. For example, S690 steel has been widely used in crane constructions, components for offshore structures, pressure vessels, load-handling equipment, and mining equipmentt [8].

However, even though S690 steel can have great balance of strength and toughness through heat treatments, the excellent mechanical properties of S690 could be affected if the steel is subsequently subjected to various processes [9]. For example, when S690 steel is utilized in additive manufacturing, the microstructure and properties of S690 will be affected by the complex thermal field, which is a characteristic of the AM process. Therefore, there is still a lot of research on the influence of processes like welding or additive manufacturing on S690 steel microstructures and properties. Besides, it is worth noting that most of these research mainly focused on wall structures rather than other complex structures. Nevertheless, complex structures are commonly used to be formed for applying them to further applications. Hence, it is a potential and important research topic to investigate microstructures and properties of S690 steel complex structures fabricated by WAAM.

1.4. Structure of the thesis

The remaining parts of the thesis include the following chapters:

- Chapter 2 provides an overview of previous research on WAAM and applications of low carbon steels to WAAM and explores the potential research topics which are not addressed in the existing research.
- Chapter 3 describes the setup of the experiments and the methods of characterization.
- Chapter 4 provides the results obtained from the experiments and discussions of the results.
- Chapter 5 provides the conclusion of the report and the recommendations for future research.

2 Literature review

The initial part of this literature review includes the studies on geometrical features of deposited structures fabricated by WAAM, and these studies are presented to put forward the limitation of depositing different geometries of parts. Finally, the previous studies on the microstructures and the mechanical properties of low carbon steels utilized in WAAM are discussed.

2.1. Geometrical features

In order to improve the usability and efficiency of WAAM, providing appropriate deposition toolpath to manufacture the deposited product with desirable geometrical features is important. Hence, there have been numerous studies to investigate WAAM deposition strategies for different geometrical features.

Mehnen et al. [10] have studied some complex geometries fabricated by WAAM. Many types of designs for stiffened panels have been investigated for its applications to the aerospace industry. The stiffened panel includes plates and beams to support high loading. The plate receives loading, and the beam supports the loading from the plate. The various geometries of stiffened panels fabricated by WAAM can improve buckling performance significantly.

The buckling index of WAAM stiffened panels with various geometrical features was explored through the experiments. Through these experiments, the supporting ability of stiffened panels with different geometrical features can be compared. The five different WAAM panel designs are shown in Figure 2.1, and these panels are made of Ti-6Al-4V and generic mild steel respectively. Furthermore, Figure 2.1 also shows the buckling index of each panel design. The buckling index is defined as the buckling load per kilogram (kN/kg). As the weights of the structures are the same, a higher buckling index means the structure can afford higher buckling load. According to Figure 2.1, the wave structure only has a slightly higher buckling index than the plate. Hence, it's not an effective strategy to use the wave structure to replace the simple plate for supporting application. However, the blade structure, open bend structure, closed bend structure and the corrugation structure all increase the buckling index significantly. Among these structures, the corrugation structure has the highest positive impact on buckling index [10].

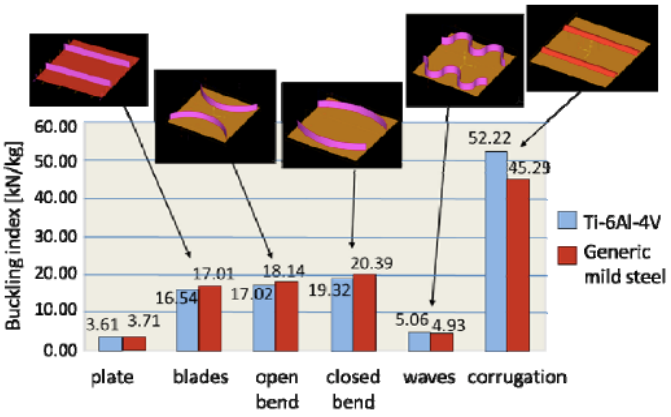

Figure 2.1: buckling index of various WAAM panel [10]

Another experimental result is shown in Figure 2.2, the experimental setting and purpose are similar to the experiment of Figure 2.1, but the experiment of Figure 2.2 introduced crossing structures. According to Figure 2.2, the improvement in buckling index by crossing structures can be proven. Compared to a simple plate, straight crossing structure, both open crossing structure, open-closed crossing structure and both closed crossing structure increase buckling index significantly [10].

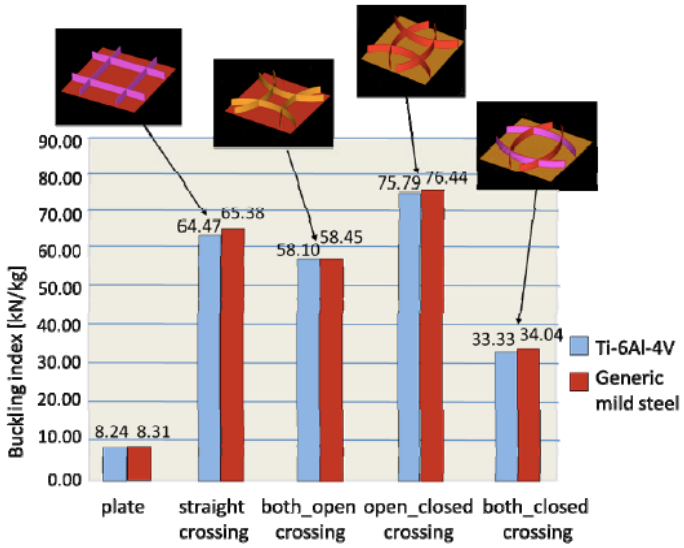

Figure 2.2: buckling index of various WAAM panel [10]

Even though buckling performance can be improved by using WAAM to deposit crossing structures, some defects like excessive camber (peak development) and deposition failure can possibly occur in crossing structures [11]. Figure 2.3 shows the peak development [10]. The peak development results from the overlapping of perpendicular beads in the crossing structure. If peak development exists then the excess machining is needed to remove the peak for getting a flat top surface, and more processing time is consumed and more material waste is produced.

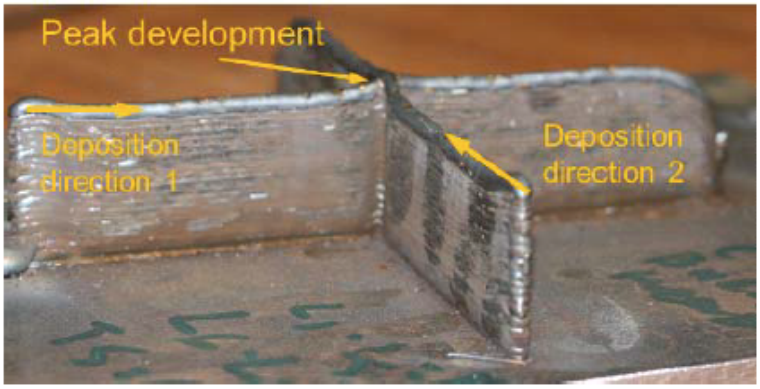

Figure 2.3: Peak development at the centre of the crossing structure [10]

Deposition failure is observed in Figure 2.4. The accumulation of depression on one side of the crossing, caused by single direction pattern for each layer, results in the deposition failure. When the welding torch passes the deposition failure, the arc becomes unstable, and this problem becomes worse as number of the layers of weld beads increases. Arc failure occurs when an obvious gap is generated due to deposition failure [10].

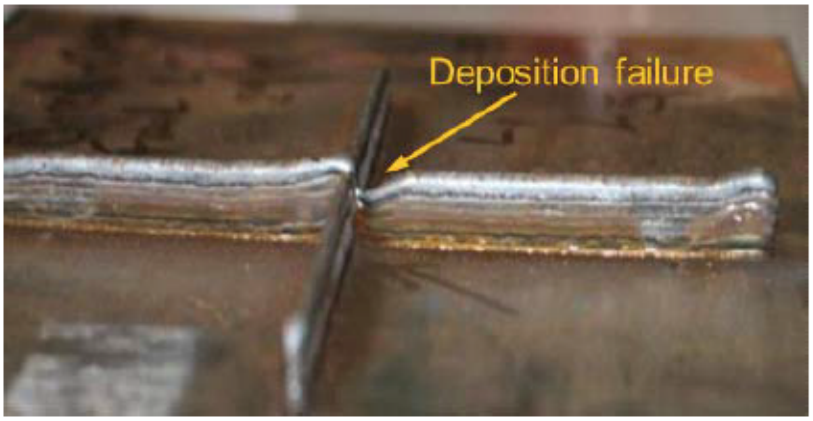

Figure 2.4: Deposition failure on the crossing structure [10]

From the previous research, the disadvantages of peak development and deposition failure have been found. Hence, Mehnen et al. [10] have further fabricated four crossing structures by using WAAM to investigate peak development and deposition failure. Figure 2.5 shows the four deposition strategies for crossing structures. Height measurements were carried out after every five layers in the locations indicated in Figure 2.6.

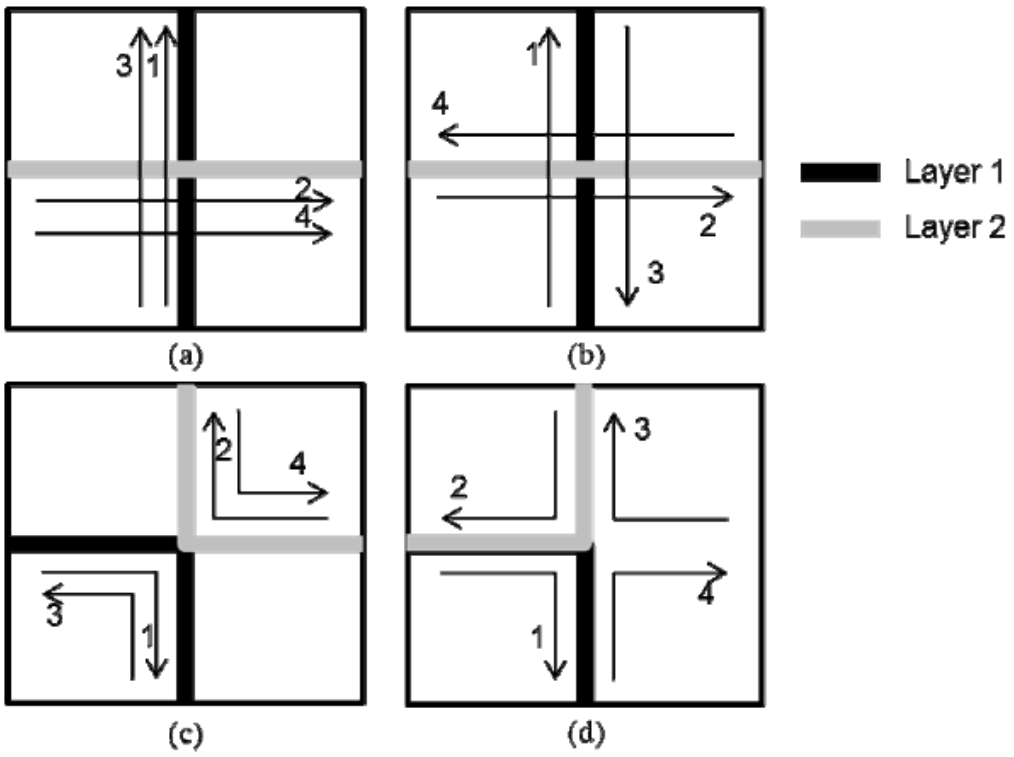

Figure 2.5: Four deposition strategies for crossing structures: (a) Direct Crossing, (b) Direct Crossing 2, (c) Opposite Angles, (d) Opposite Angles 2 [10]

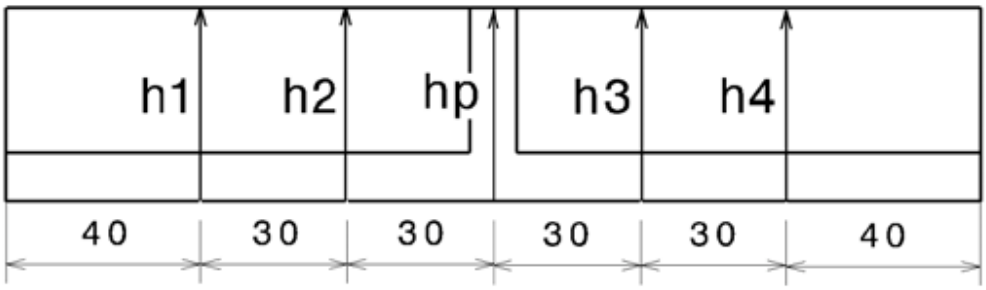

Figure 2.6: Locations of height measurement [10]

Figure 2.7 shows the result of the height measurements for a total of 30 layers. The comparison of the peak value (hp) and the average wall height for each layer has been presented. The height of the peak of the Opposite Angles build pattern keeps increasing for all 30 layers. The height of the peak of the Direct crossing build pattern increases for 15 layers. The peak of the Direct Crossing 2 build pattern achieves stability and keeps below 1.8 mm after 5 layers. The peak of the Opposite Angles 2 build pattern also achieves a stable peak and keeps below 0.55 mm after 5 layers. For practical application, the results of the Direct Crossing 2 and the Opposite Angles 2 are more acceptable than the Opposite Angles and the Direct Crossing. Figure 2.8 shows the example manufactured using the Opposite Angles 2 build pattern. Compared to the peak in Figure 2.3, the peak in Figure 2.8 is much smaller by applying the Opposite Angles 2 to decrease the height at the centre region [10].

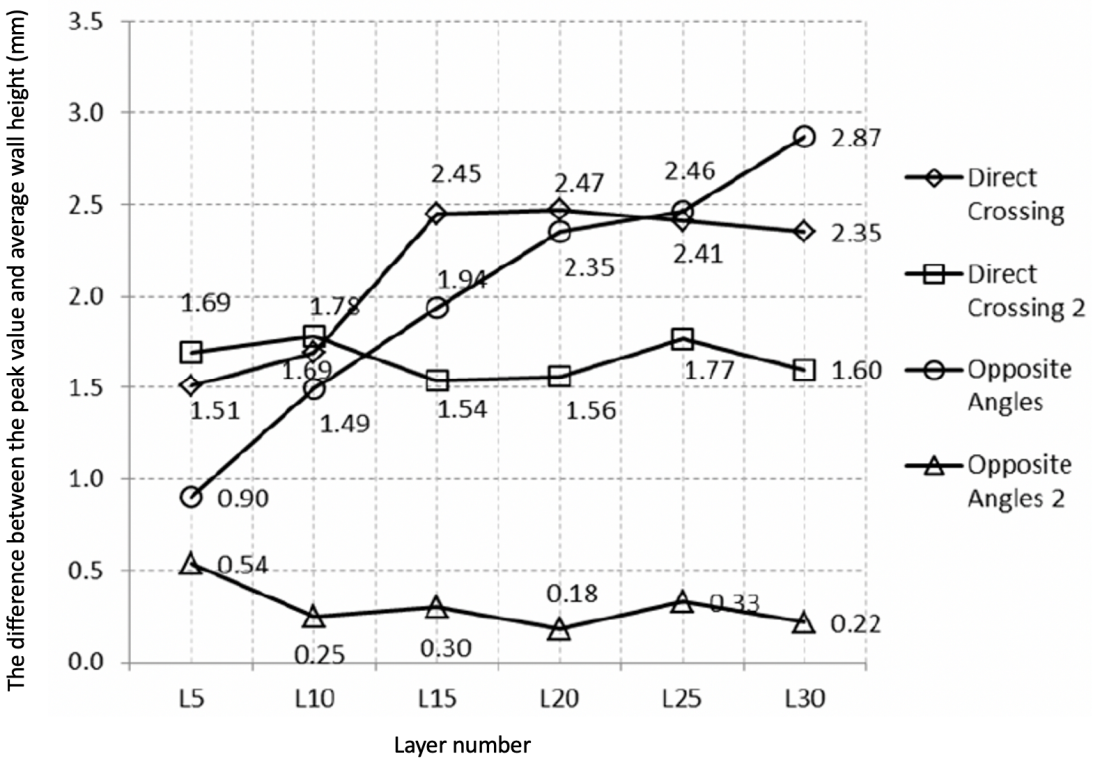

Figure 2.7: The difference between the peak value and average wall height for different crossing build patterns [10]

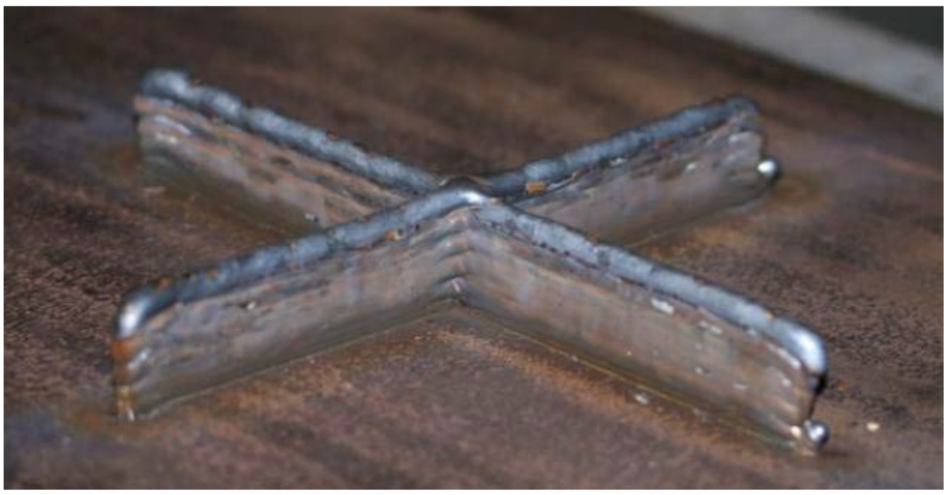

Figure 2.8: the example manufactured using the Opposite Angles 2 build pattern [10]

Figure 2.9(a) shows the development of deposition failure, which is caused by the accumulated depression when the single direction deposition pattern for each layer is applied. Mehnen et al. [10] have researched the deposition strategy to improve this deposition failure. Figure 2.9(b) shows the elimination of the deposition failure occurs when Direct Crossing 2 build pattern is applied. The explanation for the elimination of the deposition failure is that the depression generated in one layer is levelled out with the next deposited layer due to the reverse deposition of the next deposited layer.

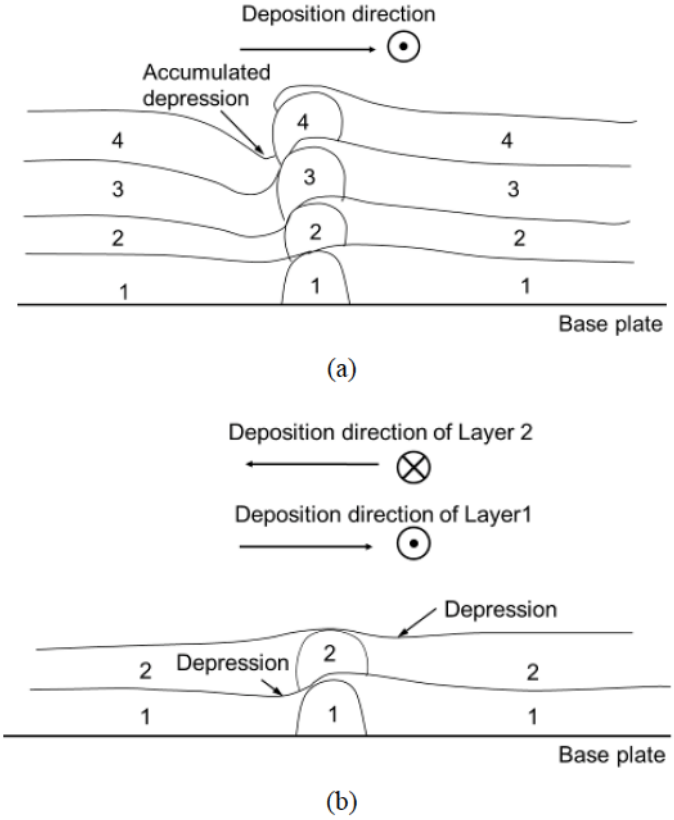

Figure 2.9: Illustrative diagram of (a) development of deposition failure; (b) elimination of deposition failure [10]

Venturini et al. [12] have investigated WAAM deposition patterns for T-crossing features by using a wire of carbon steel (AWS ER70S-6). Because the combination of WAAM and traditional machining processes is vital to meet requirements for functional components [13], the shape which facilitates the machining operations is one of the important issues addressed in the research of Venturini et al. The key issue for post-machining of T-crossing structure is internal sharp corners because these sharp corners are not accessible for post-machining. Hence, the accessibility of the corners for machining can be improved with the presence of fillets on the corners. Figure 2.10 illustrates the sharp internal corners (Figure 2.10(a)) and the internal corners with fillets (Figure 2.10(b)).

Figure 2.10: Internal corners of T crossing structures; (a) sharp (b) with fillet [12]

Venturini et al. evaluated the T-crossing structures manufactured by six deposition strategies. Figure 2.11 shows the six deposition patterns. The fillets can be formed on the internal corners through strategies S3, S3_I1 and S3_I2. Besides, by applying the strategies to form the fillets on the internal corners, it can achieve a continuous toolpath with less amount of start/stop phases and sharp internal corners. Because spatter usually comes from arc ignition and stop phases, decreasing as much as possible the number of arc start/stop phases is important [12].

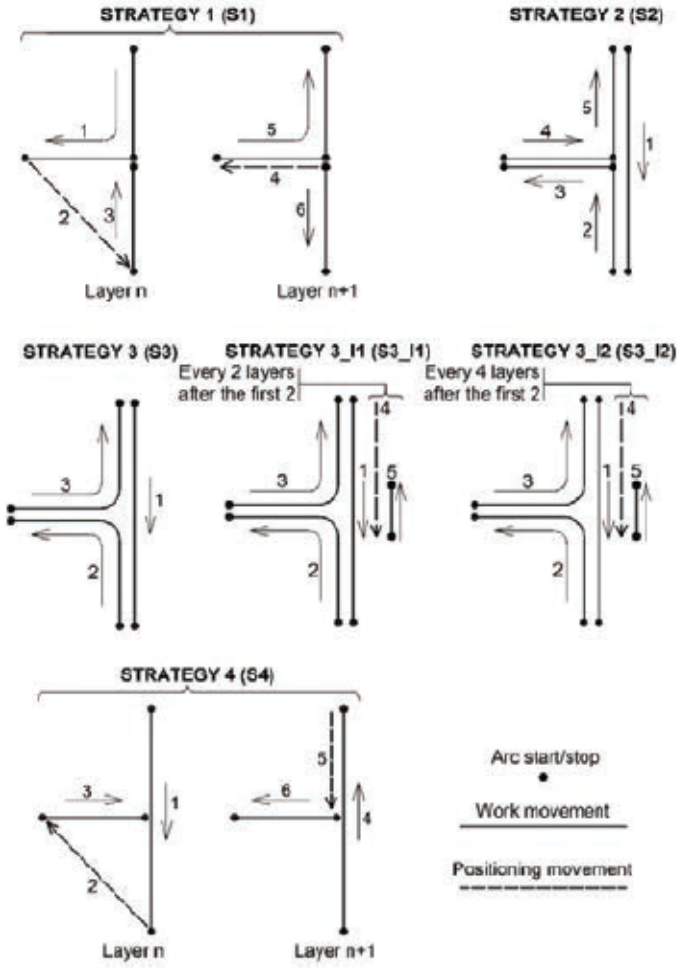

Figure 2.11: Strategies of T-crossing: S1 to S4 [12]

Figure 2.12 shows the measured points for height on the structures manufactured by these strategies. Figure 2.13 shows the difference D between the height of the central point C and the average value of the heights of the points A1, A2, B1, B2, L1 and L2 for these strategies. The difference D is calculated for every two layers. However, Figure 2.14 shows that the deposited structure of structure strategy 3 (S3) has a severe deposition failure. Hence, strategy 3 (S3) is not considered to be evaluated by the difference D. When the height in the C point is very close to the height of the points A1, A2, B1, B2, L1 and L2, the amount of material needed to

be removed becomes less, which is related to the higher deposition efficiency. Hence, according to Figure 2.13, strategy S3_I2 leads to the highest deposition efficiency because of the lowest difference D [12].

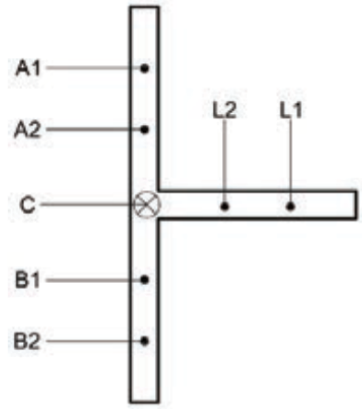

Figure 2.12: Locations of height measurements [12]

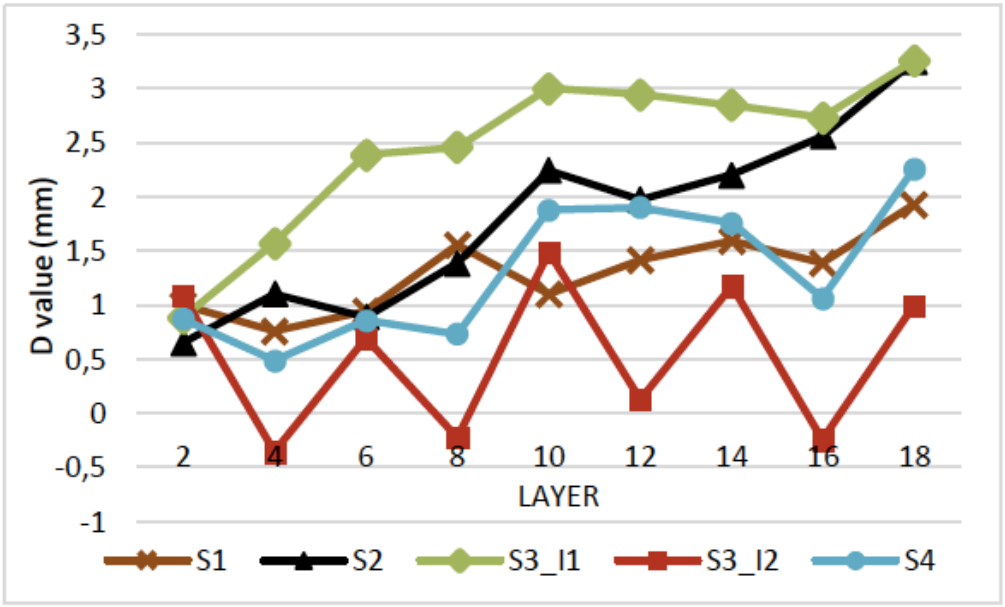

Figure 2.13: The D value for the five proposed strategies [12]

Figure 2.14: T-crossing structure built by strategy 3 (S3); the red arrow points at the deposition failure in the central zone [12]

Geng et al. [14] investigated the geometric limitation for depositing sharp-angle shape structures and curve shape structures of 5A06 Aluminum by using WAAM.

Figure 2.15 shows the beads with the designed angles of 20°, 15° and 10° deposited using WAAM. In Figure 2.15(a), path planning is to obtain the shape with a sharp angle 20°. The angle between the two axes of weld beads is 19° and the intersection angle of the inner outline is 18°. Hence, the angle between two axes of weld beads and the intersection angle of the inner outline both are close to the designed angle 20°. In Figure 2.15(b), path planning is to obtain the shape with a sharp angle of 15°. The angle between the two axes of weld beads is 15°. However, the intersection angle of the inner outline is 9°, and it is much smaller than 15°. Hence, for the shape in Figure 2.15(b), machining is needed to obtain the desired shape. In Figure 2.15(c), path planning is to obtain the shape with a sharp angle of 10°. The angle between the two axes of weld beads is 7°, and the inner outline of the angle can not be observed. The different results of these angles could be caused by the overlapping of the weld pools. Therefore, the depositing angle which is equal to or larger than 20° is preferred to be used for WAAM [14].

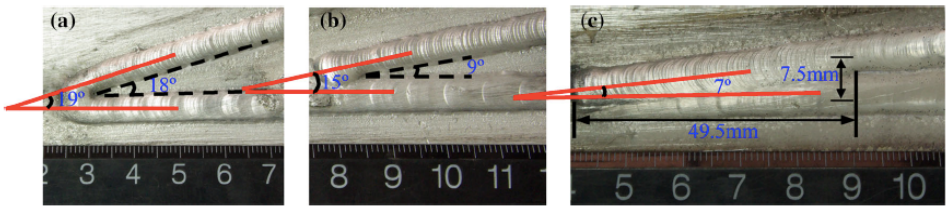

Figure 2.15: Shapes of the designed angle of (a) 20°, (b) 15° and (c) 10° deposited using WAAM [14]

Figure 2.16 shows the curve shape of the designed curvature radius of 20, 10 and 5 mm. In Figure 2.16(a), the designed curvature radius is 20 mm, and the actual curvature radius is 20.25 mm, which is close to the designed value. In Figure 2.16(b), the designed curvature radius is 10 mm, and the actual curvature radius is 9.25 mm, and it is slightly smaller than the designed value. In Figure 2.16(c), the curved shape of depositing strategies with curvature radius 5 mm shows the inner outline is distorted significantly. Hence, the preferred curvature radius for curved shape is equal to or larger than 10 mm [14].

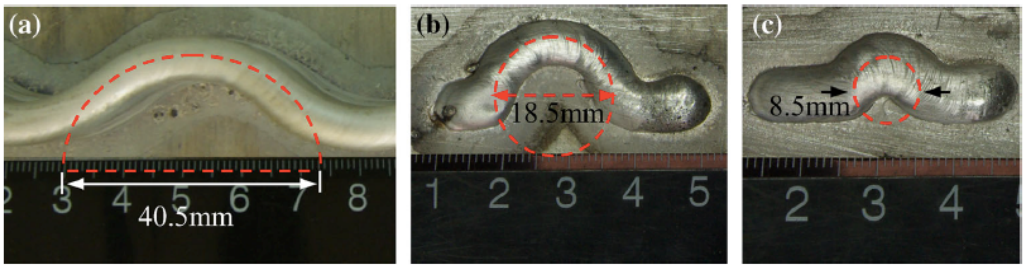

Figure 2.16: Curve shapes of the designed curvature radius of (a) 20 mm, (b) 10 mm and (c) 5 mm [14]

2.2. Microstructural evolution

There have been numerous studies to investigate the microstructural evolution of deposited materials in WAAM. Tiago et al. [3] have researched the mechanical properties, the effect of the heat input on the thermal history, and the subsequent changes induced in the microstructures at different locations in the deposited wall (shown in Figure 2.17) by using low-carbon HSLA steel AWS A5.28 ER110S-G wire (also known as S690 HSLA steel) for WAAM. The composition of the ER110S-G wire is shown in Table 2.1. In this research, WAAM walls P1 and P2 were respectively made with heat inputs of 511 J/mm and 221 J/mm by changing the travel speed from 3.9 mm/s to 9 mm/s.

Table 2.1: Chemical composition of the ER110S-G wire electrode [wt.%] [3]

Element	C	Mn	Si	Ni	Cr	Mo	V	Cu
Weight Percentage (wt%)	0.08	1.70	0.44	1.35	0.23	0.30	0.08	0.25

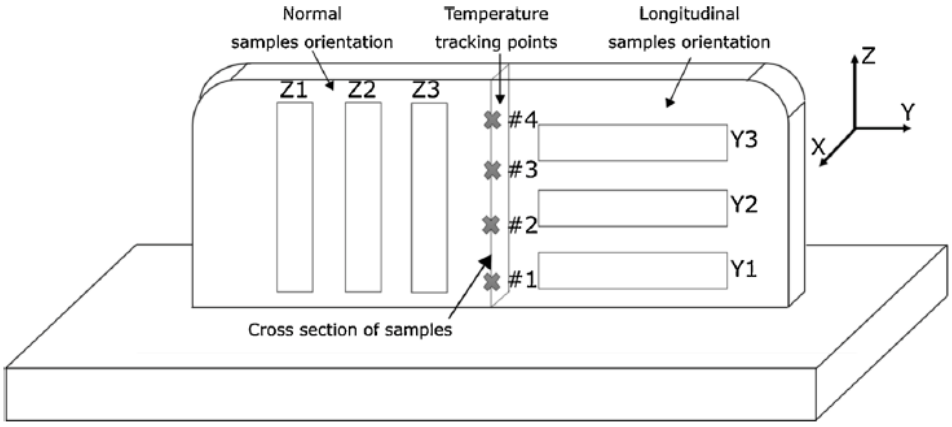

Figure 2.17: Illustrative diagram showing the temperature measurement points, location of specimens used for uniaxial tensile and impact testing, and cross-section of samples. [3]

Rafieazad et al. [15] have also presented a detailed study of the microstructure and mechanical properties of the WAAM thin-wall parts using an ER70S-6 low-carbon low-alloyed steel wire. Additionally, the influence of the manufacturing process on the anisotropy of the mechanical properties was investigated. The fabricated wall is schematically shown in Figure 2.18. Each deposited layer on the x-y plane has six beads, and each bead has a length of 135 mm. The total height of the wall is about 150 mm, and it includes 50 consecutive layers.

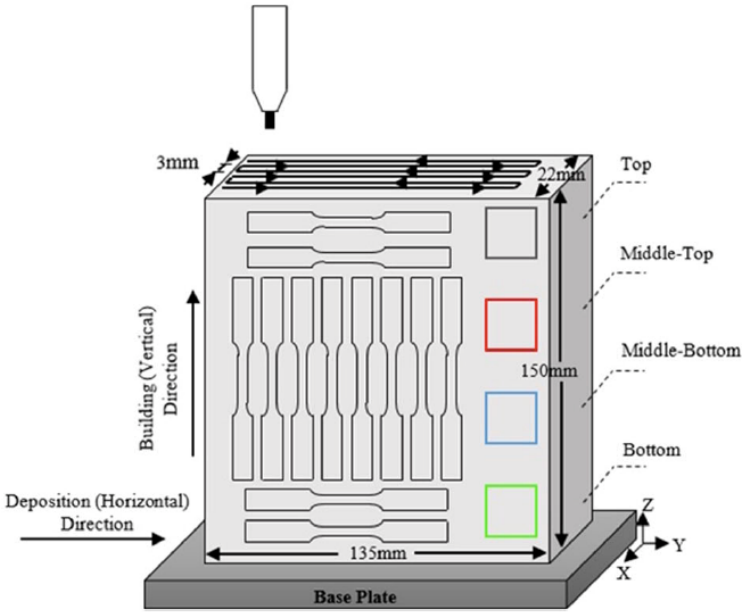

Figure 2.18: Schematic illustration of the steel wall. [15]

The thermal history is one of the most essential elements to explore the microstructural evolution. In the research of Tiago et al. [3], the temperature was monitored along the z-direction of the wall, and there are totally four different tracking points (shown in Figure 2.17). With these tracking points, the evolution of the cooling rate along a wall being deposited can be explored. The heat transferring from the deposition of a new layer to the previously deposited layer can impact microstructure because the heat transfer affects the cooling rate and thermal cycles of both the previously and currently deposited layers, leading to microstructural changes along the part [3]. At these tracking locations (shown in Figure 2.17), cross-sections were cut out for researching the microstructure and mechanical properties further, which will also be illustrated further below [3].

The thermal histories of the experiments of Tiago et al. [3] have been shown in Figure 2.19 and Figure 2.20. Figure 2.19 shows the thermal cycles on the second tracking point of sample P1 and sample P2 [3]. Cooling rates were calculated from the average temperature gradient from 800 to 500 °C. Between 800 to 500 °C, the cooling rates significantly influence the microstructure of the steel [16]. The peak temperature and cooling rate both decrease with the increase in the distance to the weld pool. Higher heat input for sample P1 increased the number of times of surpassing the austenitization temperature, which is about 800 °C [17]. However, for sample P2, this occurred only twice.

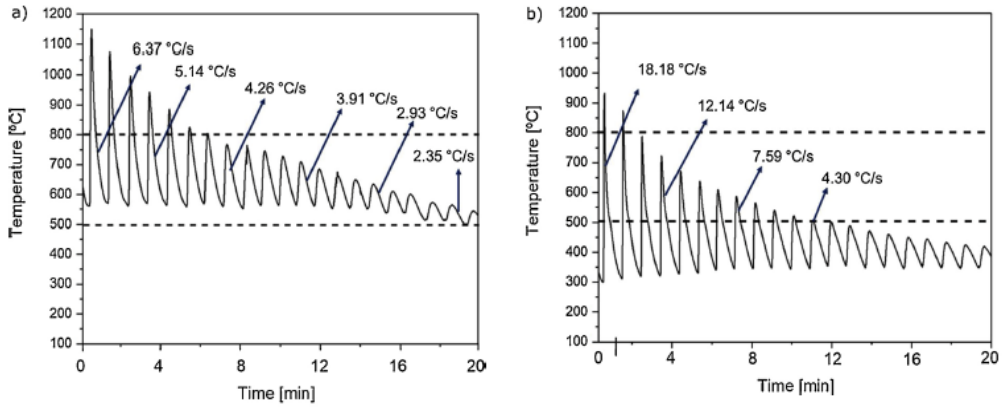

Figure 2.19: Thermal histories of the second tracking point of samples: a) P1 and b) P2 [3]

Figure 2.20 depicts the cooling rates which changed with the subsequent passes above the tracking points for samples P1 and P2, respectively [3]. The sample P1 manufactured with a higher heat input has lower cooling rates than the sample P2 because of the higher heat accumulation in the sample P1. Moreover, the fast cooling rate in the first deposited layers is aided by the cold substrate which has a good capacity for heat dissipation [3].

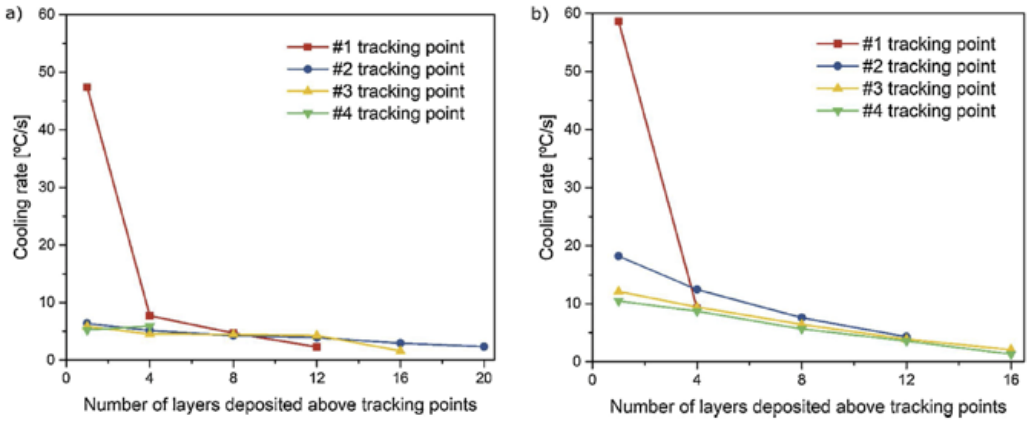

Figure 2.20: Cooling rates [°C /s] of samples: a) P1; b) P2. [3]

In the experiment of Rafieazad et al. [15], a 10-min interval was set up between each layer. Hence, all layers have undergone nearly consistent heating and cooling cycles. Furthermore, a 10-min interval between each layer can decrease the effect of heat accumulation and prevent microstructural variations in different layers along the z-direction [15].

Tiago et al. [3] have shown the observation of microstructures. Figure 2.21 shows sample P1 and sample P2 of the microstructural pictures captured by optical microscopy [3]. In Figure 2.21, for each tracking point, the grain size of sample P1 is larger than the grain size of sample P2 because sample P1 is manufactured with the higher heat input, which facilitates grain growth. Due to the repeated reheating and thermal accumulation, it can be observed in Figure 2.21 that the grain size becomes coarser along the building direction of sample P1 and sample P2.

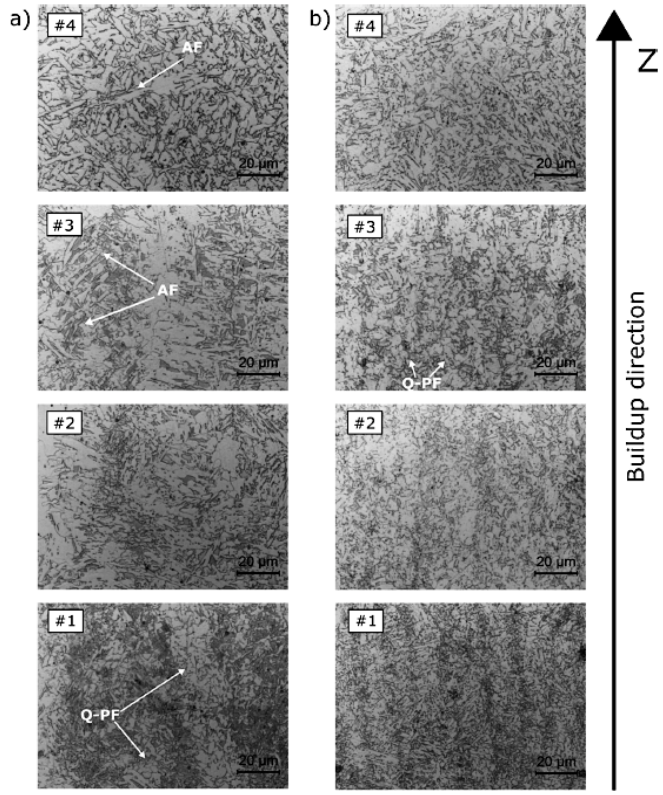

Figure 2.21: Microstructures of cross-section: a) P1 and b) P2 along the height (AF: acicular ferrite; PF: polygonal ferrite). [3]

Because of the several reheating cycles that each layer experiences, the microstructures of the deposited parts are similar to the microstructure of a heat-affected zone in HSLA steel. For HSLA steel, the transformations of the microstructure can be categorized according to two temperature regions: 1300°C to 800 °C and 800°C to 500 °C. During 1300 to 800 °C, austenite grain grows. In the 800 to 500 °C range, austenite transforms into various ferrite morphologies and bainite, which also contains ferrite morphology [17]. Upon cooling from the high-temperature region, austenite starts to transfer to ferrite, with the occurring of grain boundary ferrite, also known as allotriomorphic ferrite, at the prior austenite grain boundaries. Then, at the austenite/ferrite boundaries, nucleation of widmanstatten ferrite, also known as side-plate ferrite, may evolve and extend into the untransformed austenite grains. Nucleation of the plate of acicular ferrite occurs on small non-metallic inclusions, such as oxide inclusions. Moreover, during further cooling, bainite may form and carbon may diffuse into remaining austenite [18]. The carbon content in the remaining austenite can influence the Ms and Mf of martensite transformation temperatures in carbon steels [19]. When further cooling to room temperature, the remaining austenite fully or partially transforms into martensite. When austenite partially transforms into martensite, the product called martensite-austenite (M-A) is formed.

Figure 2.22 illustrates the SEM images of the microstructure of the sample P1 [3]. Figure 2.22(a) shows an overview of SEM images of sample P1 in zone #3 illustrating the three different microstructures: acicular ferrite (AF), quasi-polygonal ferrite (Q-PF), and bainite. These microstructures can be predicted by the

continuous cooling transformation (CCT) diagram (shown in Figure 2.23) of HSLA steel with a similar chemical composition of the feeding material used in this work [20]. Here the attention is given to sample P1 but the same microconstituents are also observed in sample P2. The martensite-austenite (M-A) can be observed in Figure 2.22(b) and Figure 2.22(c) with higher SEM magnification. Figure 2.22(c) also shows granular bainite in a high-contrast image [3].

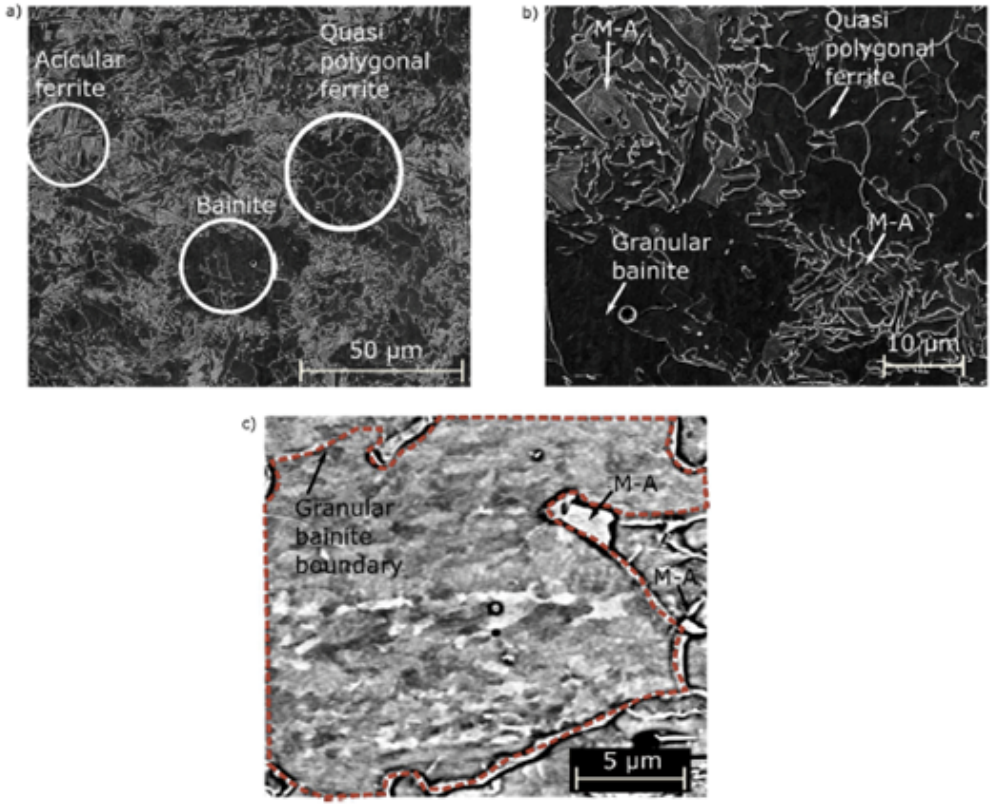

Figure 2.22: SEM images of the samples: a) overview; b) image with high magnification; c) close-up of granular bainite [3]

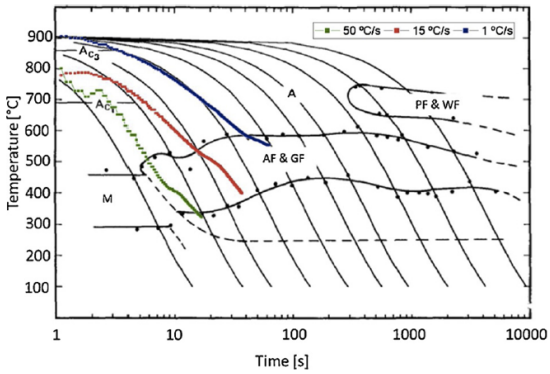

Figure 2.23: CCT diagram for HSLA steel with a similar chemical composition of the feeding material. [18]

In the research of Rafieazad et al. [15], to perform microstructural characterization and investigate possible microstructural anisotropy in the deposited wall, four samples from different locations of the wall, including the bottom, middle bottom, middle top and the top, were sectioned along the building direction (shown in

Figure 2.18). Figure 2.24 demonstrates the overall microstructure of the ER70S-6 steel wall in different regions. Figure 2.24 (b) and (d) show that the primary phase is the typical fine polygonal ferrite (F), and a low-volume fraction of the lamellar pearlite (P) phase also can be observed, which has primarily formed along the ferrite grain boundaries. Haden et al. [21] also presented similar microstructural features for a WAAM fabricated ER70S-6 wall. Furthermore, Figure 2.24 (c) and Figure (e) show the formation of acicular ferrite as well as bainite regions (AF + B). The aforementioned microstructural features can be observed throughout all layers from the bottom to the top zones of the wall, and it is because, in the experiment, a 10-min interval between each layer can decrease the effect of heat accumulation, and avoid microstructural variations in different layers. Furthermore, approximately consistent heating and cooling cycles across all layers result in a uniform microstructure along the building direction [15].

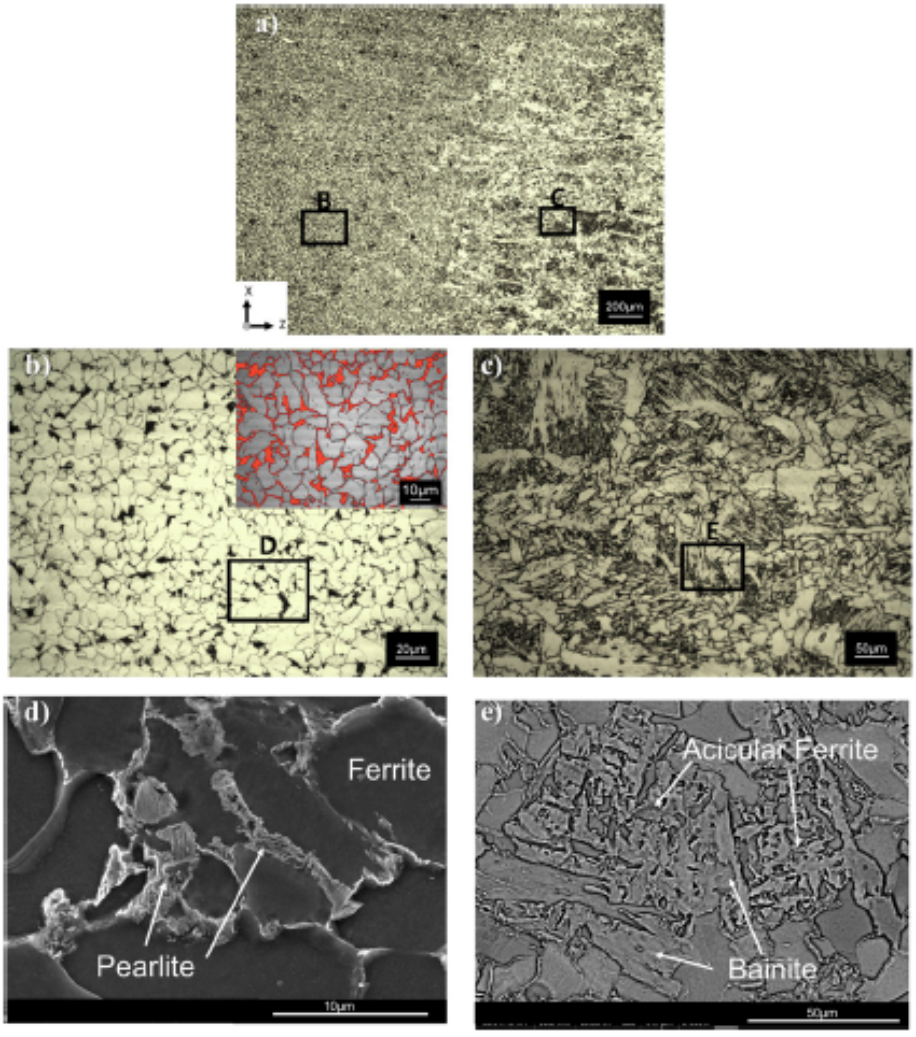

Figure 2.24: Optical images taken from a) at the fusion line and centre of the melt pool of the WAAM-ER70S-6 steel wall. b) Higher magnification of the enclosed area B in a), presenting the distribution of the pearlite phase (in red) along the ferrite grain boundaries. c) The enclosed area C in a). d) the enclosed area D in b). e) The enclosed area E in c). [15]

In Figure 2.22 and Figure 2.24(e), bainite occupies a large percentage in the microstructure. Different types of bainite will be discussed further below. Generally, bainite is an aggregate of carbides(cementite) and dislocation-rich and plate-shaped ferrite but there are still various types of bainite. In Table 2.2, bainite is classified into five types of bainite based on the morphology of bainitic ferrite and the type and distribution of the second phase [22]. Furthermore, Figure 2.25 shows the illustrative diagram of the microstructural evolution of upper bainite and lower bainite. Figure 2.25 illustrates that at high temperature, most carbon will diffuse away from the ferrite to austenite and participate as carbides in the residual austenite between the ferritic plates, finally evolving into upper bainite. Besides, at low temperatures, the carbon will diffuse more slowly and more carbides precipitate in ferrite, leading to the microstructure of lower bainite [23].

Table 2.2: Morphological classification of bainite [22]

Bainite	Morphology	Bainite description
Granular bainite	Irregular ferrite with M/A	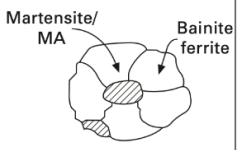
Lath-like upper bainite	Lath-like ferrite with cementite on lath boundaries	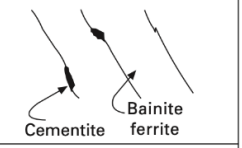
Cementite-free lath-like bainite	Lath-like ferrite with M/A on lath boundaries	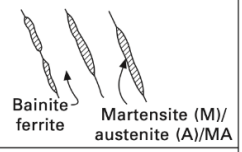
Lath-like lower bainite	Lath-like ferrite with cementite inside the ferrite laths	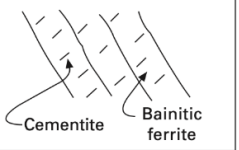
Plate-like lower bainite	Plate-like ferrite with cementite inside the ferrite plates	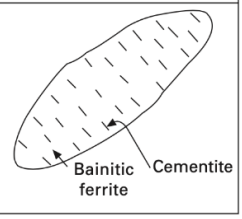

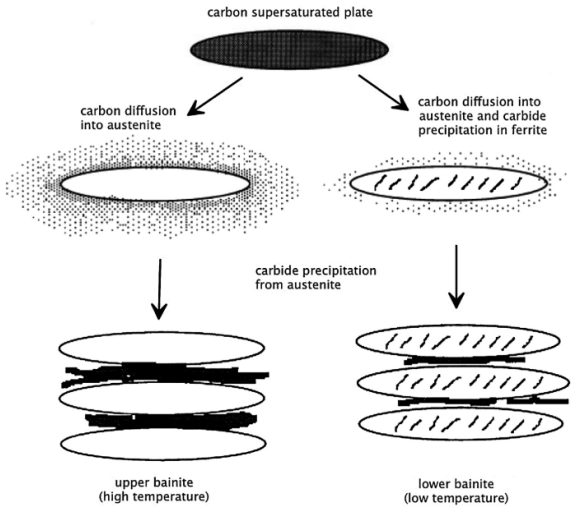

Figure 2.25: The schematic representation of the microstructural evolution of upper bainite and lower bainite [23]

Figure 2.26(a) shows the picture of upper bainite, including the sheaves of bainite (dark) and the retained austenite (white) between sheaves. Bhadeshia et al. [23] stated that the formation of upper bainite occurs at about 400–550 °C in the form of sheaves, and sheaves include parallel plates of ferrite. Each plate is around 0.2 μm thick and about 10 μm long. Figure 2.26(b) shows the microstructure of lower bainite, including the sheaves of lower bainite. Lower bainite forms at about 400–250 °C. The microstructure of lower bainite and that of upper bainite are similar but more carbides can be observed inside the ferritic plates [23] [24] [25].

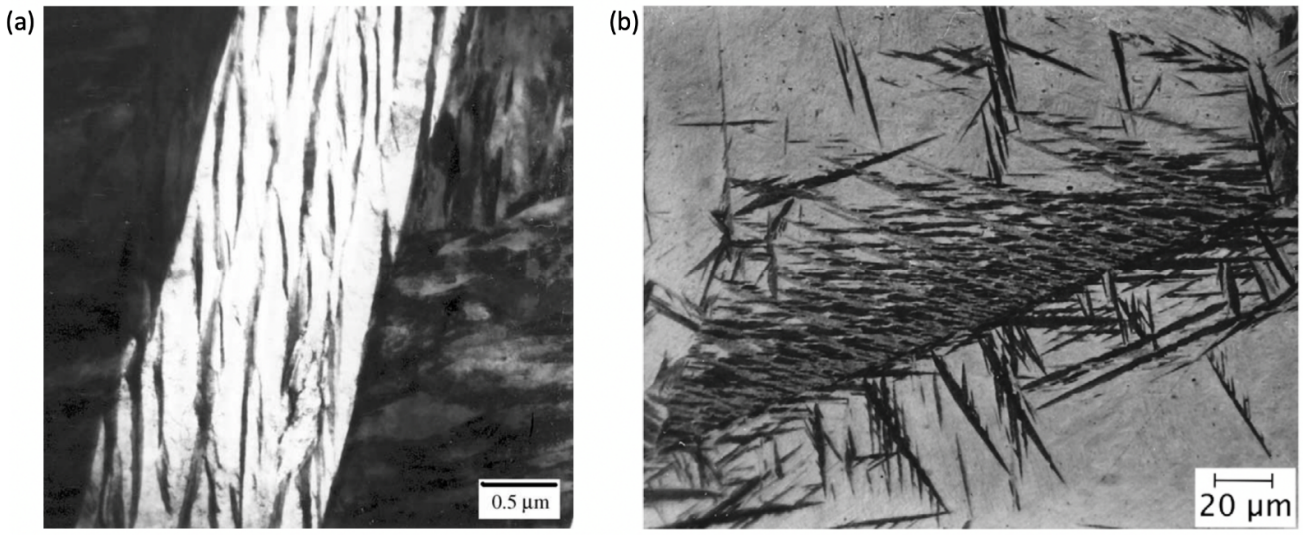

Figure 2.26: Optical images of bainite: (a) upper bainite (b) lower bainite [23]

Besides, Tiago et al. [3] mentioned another type of bainite shown in Figure 2.22: Granular bainite. The major mechanism of the formation of granular bainite is the same as ordinary bainite, which was mentioned above. Granular bainite can be frequently observed in the sample fabricated by additive manufacturing. When additive manufacturing is applied, the material undergoes a non-isothermal heat treatment, which includes a continuous cooling process to form granular bainite. More specifically, when the component is deposited during additive manufacturing, it cools down slowly, which makes the sheaves of bainite much coarser, and gives the appearance of blocky bainite. Hence, "granular" is used to describe the blocky feature of this kind of bainite, and to differentiate it from the other types of bainite [23].

Besides, Sun et al. [26] illustrated tempered bainite, see Figure 2.27. They deposited a HSLA multi-layers structure and because of the impact of a long-term thermal cycle during the deposition of the subsequent layers, bainite is heated and tempered into tempered bainite.

Carbon can lead to solid solution strengthening effect to make materials harder. Thus, the strength of martensite decreases dramatically because of the carbon precipitates during tempering. Figure 2.28 shows the microstructures of tempered martensite of Fe-4Mo-0.2C wt% steel, which has been quenched and then experienced different tempering temperatures and tempering times [23]. However, for bainite, carbon is precipitated as coarse carbides, contributing little to strength. Hence, it can be expected that the tempering response of bainite is less sensitive to carbon concentration.

Nevertheless, bainite still becomes softer after tempering because of other reasons. The softening of bainite is due to that the microstructure of bainite plates becomes coarser or recrystallizes into equiaxed grains of ferrite, which replace the bainite plates. Besides, bainite possibly becomes softer because of the coarsening of cementite particles and the occurrence of the recovery of the dislocation [23].

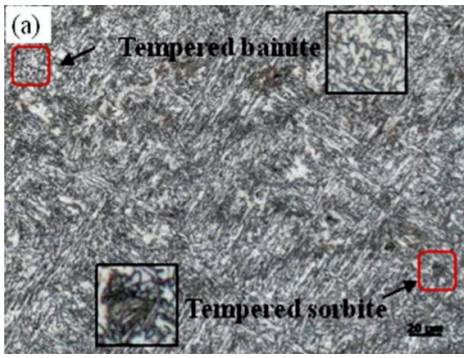

Figure 2.27: The microstructure of bainite in a HSLA multi-layers structure [26]

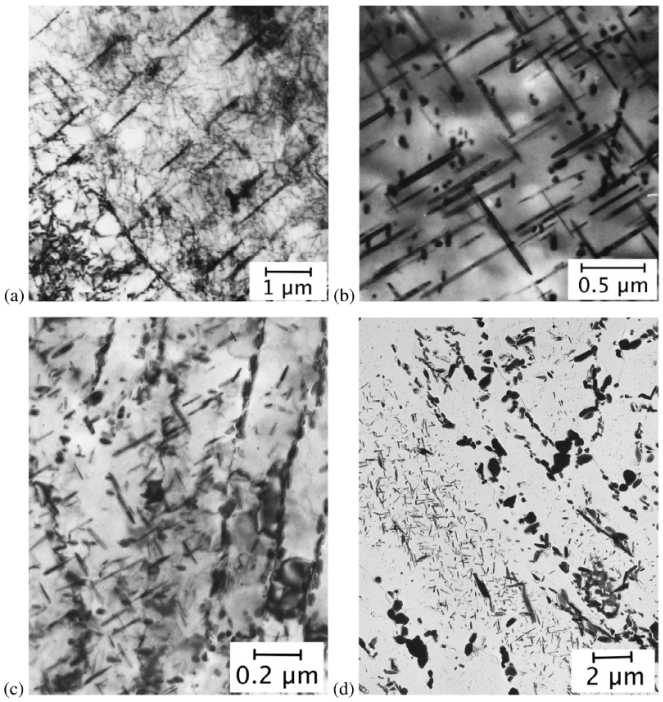

Figure 2.28: Fe-4Mo-0.2C wt% steel with different tempering temperature and time: (a) Tempered at 563 ℃ for 4 hours 30 mins; (b) Tempered at 675 ℃ for 15 hours; (c) Tempered at 700 ℃ for 30 mins; (d) Extraction image of the sample in (c) [23]

Tiago et al. presented a microstructure that was observed in their research: martensite-retained austenite (MA) (see Figure 2.22). MA results from heating into the intercritical phase region of austenite and ferrite, during multipass welding, followed by rapid cooling. In the thermal cycle, austenite nucleates and grows along the bainite lath boundaries and the prior austenite grain boundaries. A large quantity of carbons diffuse into the austenite islands, while there is not sufficient time for substitutional element diffusion. During cooling, the intercritical microstructures transform to products, known as MA constituent. The predominant austenite growth occurs initially along the prior austenite grain boundaries, which has a necklace appearance. Figure 2.29 clearly illustrates the MA distribute along prior austenite grain boundaries and the shape of the distribution looks like a necklace [27] [28].

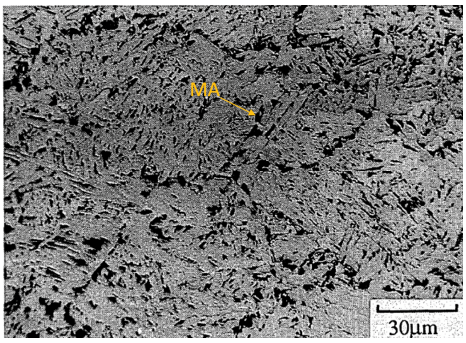

Figure 2.29: Distribution of MA [28]

The brittle nature of the MA constituent could lead to fast cracking propagation in materials. This mechanism occurs when the MA constituents are connected or nearly connected along prior austenite grain boundaries. Figure 2.30 shows the microstructure of a charpy V impact sample tested at room temperature. It clearly shows that the path of the crack is along the shape of the prior austenite grain boundary. Moreover, Sridharan et al. [27] stated that the brittle nature of the MA constituent exists when MA has a stringer morphology. Figure 2.31 shows the blocky MA and MA with a stringer like morphology in between the bainitic ferrite.

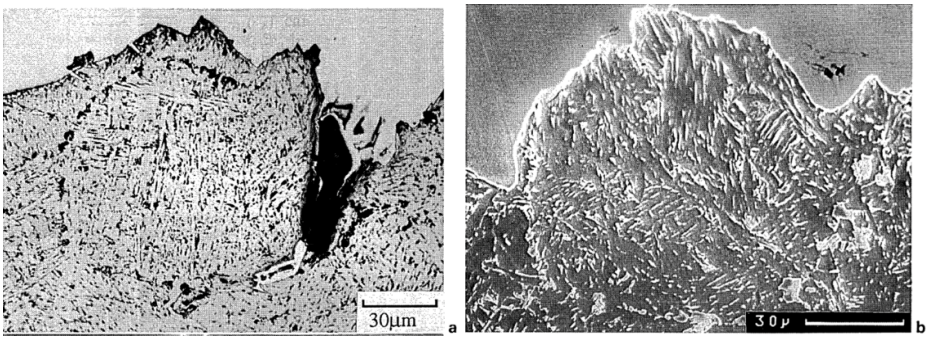

Figure 2.30: Crack path along prior austenite grain boundary [28]

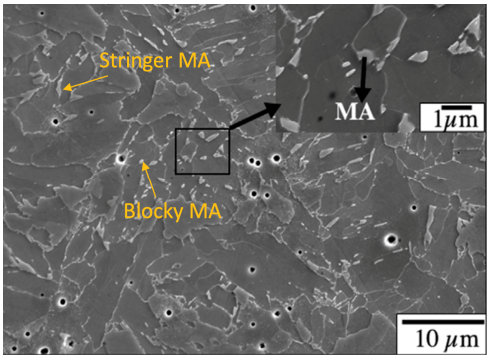

Figure 2.31: Blocky MA and MA in a form of stringer [27]

The reason for the weakened toughness due to connected or nearly connected MA is explained further here. The presence of MA with a stringer between the ferrite laths make MA easily gets debonded from the surrounding matrix. Davis et al. presented that the possible reason for the easily debonding feature of MA particles is a combination of the low interfacial energy for MA particles and unrelieved transformation stresses on the interface resulting from the martensite formation. An isolated MA particle also may debond, but this is not sufficient to cause failure. The region in between the debonded MA particles is constrained and subjected to high local stresses, which can cause a microcrack to form. The connected MA network enables a series of debonded MA particles in close proximity to provide a constrained region, having higher stress concentration to initiate local cleavage [28].

Electron backscattered diffraction (EBSD) is one of the most important techniques to explore the orientation microstructural features. Tiago et al. [3] utilized EBSD measurement to investigate the orientation grains. Figure 2.32 depicts EBSD measurements of sample P1 in zone #3, manufactured with a higher heat input [3]. The colour of the orientation map can be interpreted by the stereographic triangle, which shows the corresponding colour for different orientation. The orientation map in Figure 2.32 shows that no significant preferential orientation was developed [3]. Rafieazad et al. [15] also presented the result of the EBSD test in Figure 2.33, which also shows that the deposited component is also composed of randomly oriented grains. However, in both of research of Tiago et al. [3] and Rafieazad et al. [15], they did not discover the reason why there is no the preferential texture developed in the deposited structures.

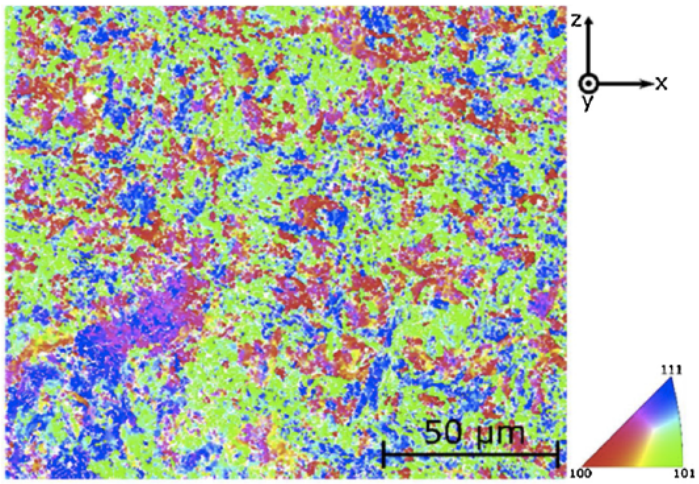

Figure 2.32: Electron backscattered diffraction (EBSD) inverse pole figure measurements of sample P1 [3]

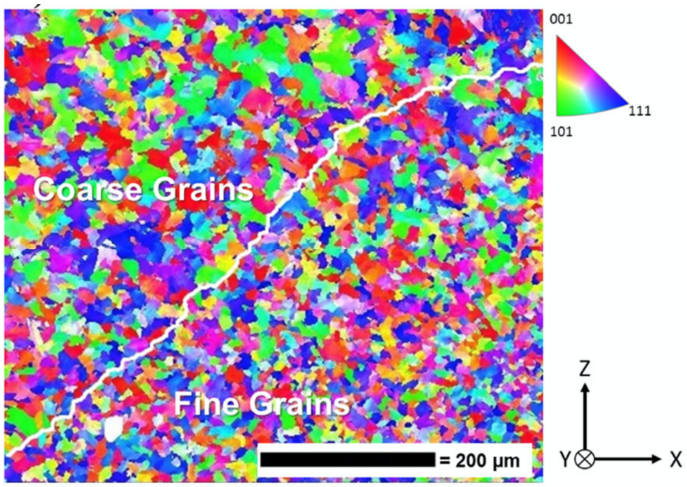

Figure 2.33: EBSD inverse pole figure map of the deposited sample [15]

X-ray diffraction (XRD) is commonly used to explore the microstructural evolution. In the investigation of XRD analysis is established on X-rays and a crystalline sample. A cathode-ray tube produces the X-rays, filtered to generate monochromatic radiation, collimated to concentrate and radiate toward the sample. The

interaction between the incident rays and the analyzed sample generates constructive interference (and a diffracted ray) when Bragg's Law ($n\lambda=2d \sin \theta$) is satisfied. The pattern of the characteristic x-ray diffraction produced in a typical XRD analysis provides a "fingerprint" of the crystals present in the sample. By comparing standard reference patterns and measurements, identification of the crystalline form can be confirmed by the fingerprint [29]. Rafieazad et al. [15], the XRD analysis of the WAAM-ER70S-6 wall was conducted for phase identification on the samples extracted along the building direction (Figure 2.18), and the obtained spectra are presented in Figure 2.34 [15].

According to Figure 2.34, the deposited wall predominantly includes α-Iron (BCC, Ferrite) phase as the main constituent. The locations of the α-Iron peaks are at 2θ of approximately 44.55°, 64.85°, and 82.11° according to the JCPDS patterns of 98-000-9982 [29]. Figure 2.34 shows identical XRD patterns obtained from different locations along the building direction, which is the convincing evidence for the uniformity and homogeneity of the microstructure along the building direction of the deposited wall [15]. More specifically, when the deposited wall was built up, a 10-minutes interval was set between each layer, which decreased the effect of heat accumulation and let all layers have undergone nearly consistent thermal cycles. Therefore, microstructural variations were prevented along the z-direction, which leads to the same XRD patterns obtained along the building direction.

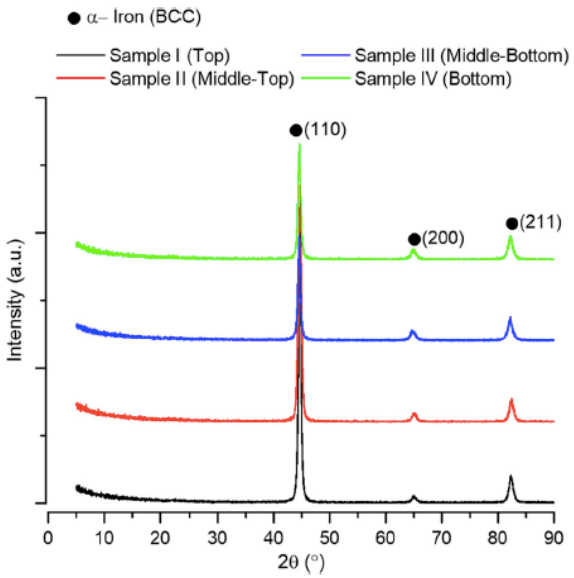

Figure 2.34: XRD pattern of the WAAM-ER70S-6 samples taken from different locations along the building direction. [15]

2.3. Mechanical behaviour

Tiago et al. [3] have studied the mechanical properties of WAAM walls P1 and P2, respectively made with heat inputs of 511 J/mm and 221 J/mm. Figure 2.35 shows the microhardness distributions near four tracking points on the cross-sections of samples P1 and P2. The hardness tends to decreases along the building height because the grain size increases along the building height (the variation of grain size is shown in Figure 2.21).

Moreover, P1 has higher heat input so it has a lower cooling rate. Hence, it can be inferred that the hardness of P2 should be larger than that of P1 at every height level. However, according to Figure 2.35, in the lowest layers, P1 shows the larger hardness than P2. Hence, there is a contradiction between the the hardness of the prediction based on heat input and the hardness shown in Figure 2.35. The possible reason for this contradiction is the experimental error during the localized microhardness measurement or P1 subjected to a larger effect of the substrate.

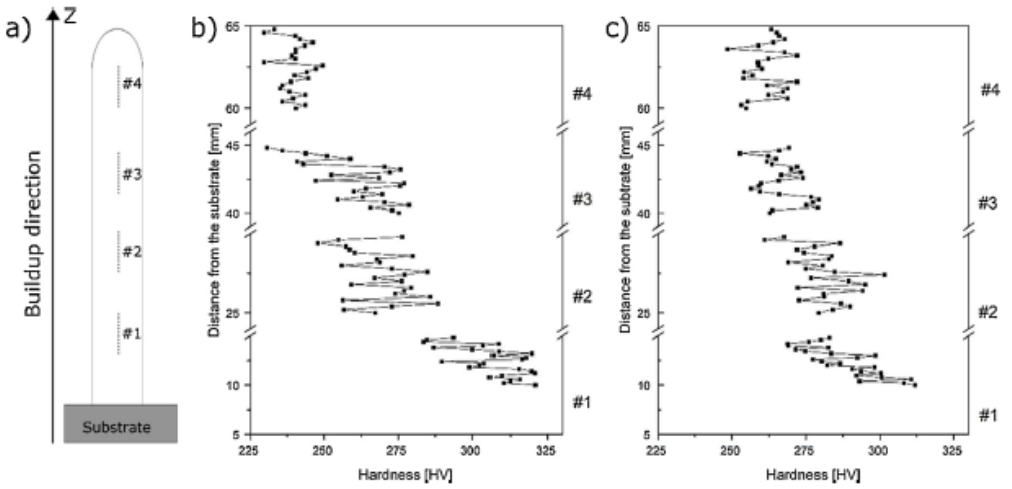

Figure 2.35: a) Schematic representation of indents made on the cross-sections of samples. Microhardness profiles along the z-direction of samples: b) P1; c) P2 [3]

Rafieazad et al. [15] have also investigated the mechanical properties of an AM wall. In Figure 2.36, the microhardness values are evenly distributed in all deposited layers from the bottom to the top of the WAAM-manufactured wall. Because Rafieazad et al. have kept a 10-minutes interval between each layer to weaken the effect of heat accumulation and avoid microstructural variations in different layers, the evenly distributed microhardness values were measured and taken as proof of homogeneity of the microstructure in the deposited wall.

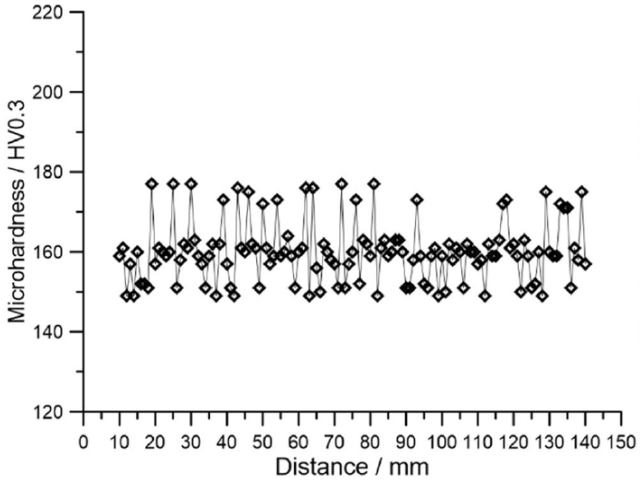

Figure 2.36: Microhardness distribution on different points on the surface along the z-direction of the wall [15]

Tiago et al. [3] have carried out tensile tests for samples. Tensile tests were performed on the samples along the longitudinal (Y) and normal (Z) directions of the deposited wall, the samples for the tensile test are shown in Figure 2.17. Average values for the ultimate tensile strength (UTS) and elongation-to-fracture are shown in Figure 2.37. The small difference of values of UTS or elongation-to-fracture obtained along the Y and Z directions for the samples proves the homogeneity of the mechanical properties. The reason for the homogeneity is due to the fact that no preferential texture was developed. Furthermore, the Charpy V impact test was utilized in the research of Tiago et al. [3]. Through the Charpy impact test, the impact toughness values of the samples extracted along the longitudinal (Y) and normal (Z) direction were measured, and they are 15 J and 18 J, respectively. An empirical hyperbolic-tangent equation [30] is utilized to convert the acquired data to that of a normalized 10 mm thickness specimen, and the converted values are 57 J and 71 J. The impact toughness of the as-received feedstock material was about 70 J. This difference between converted values and the impact toughness of the as-received feedstock material is within the range of uncertainty of the measurements and the empirical method used. It proves that between the vertical and horizontal samples, the homogeneity of mechanical properties exists [3].

In addition, according to Figure 2.37, the elongation-to-fracture of all samples indicated a good ductility. The reason for the good ductility is the presence of ferrite in the microstructure of the material. Furthermore, Figure 2.37 also shows that the tensile strength is larger than 700MPa, which is due to the formation of bainite [3].

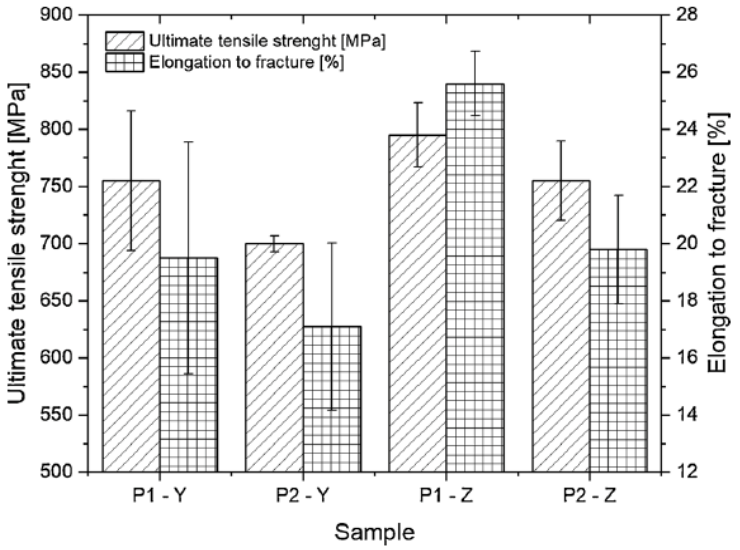

Figure 2.37: Ultimate tensile strength (UTS) and elongation to fracture of the tested samples [3]

Tensile tests were also utilized in the research of Rafieazad et al. [15]. Tensile tests were performed on the samples along the longitudinal (Y) and normal (Z) directions of the deposited wall, and the horizontal samples were obtained from both the top and bottom regions of the wall, and the vertical samples were obtained from the middle region of the wall, shown schematically in Figure 2.18. The result of the

measurements is shown in Figure 2.38 in the form of the standard stress versus strain diagram. Figure 2.38 also depicts the average values of UTS and YS of the horizontal and vertical samples, and it shows a similar yield strength and ultimate tensile strength values in both directions, showing isotropic tensile properties. The consistency in the tensile strength of the vertical and horizontal samples confirms the uniformity and homogeneity of the microstructure. Nevertheless, in Figure 2.38, the elongation of the vertical samples is lower than that of the horizontal samples, which indicates an anisotropy in ductility. The large reduction in the ductility value from the horizontal sample to the vertical one can be explained by the following possible reasons: (a) the existence of manufacturing discontinuities and defects. For example, there is a lack of fusion or porosity accumulated in the interlayer regions; (b) coarsening of the grain occurs along the HAZ. (c) the formation of brittle martensite–austenite (MA) constituent, which could result in the propagation of micro-cracks in early stages of the tensile test, and finally crack at notably lower strain values [15].

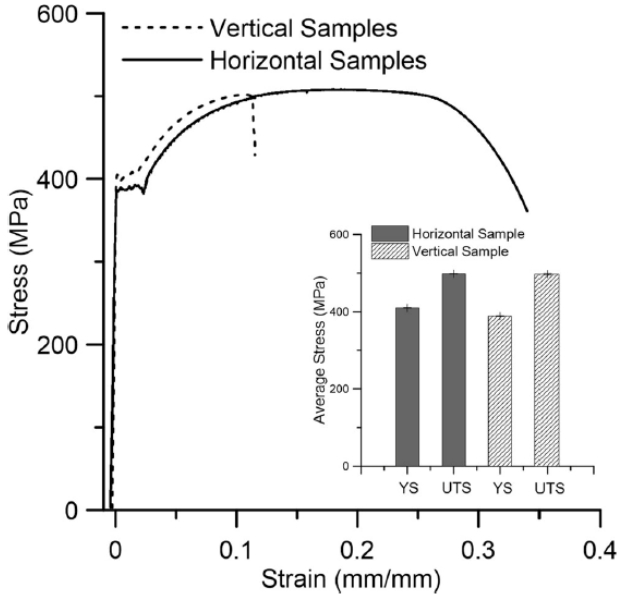

Figure 2.38: The stress-strain curves and their corresponding tensile properties for the vertical and horizontal samples [15]

2.4. Summary

The studies on deposited structures with complex geometries, such as direct crossing structures, T-crossing and sharp angle structures, have mainly proposed the problems about geometrical limitation and the deposition strategies for solving these problems. However, these studies did not investigate how these strategies and process parameters could influence microstructures and mechanical properties of the deposited structures. For various applications, the desired mechanical properties of deposited structures are obtained by modifying different process conditions to get desired microstructures. Hence, for applying these deposited structures to further applications, it is essential to obtain a good understanding of the relationship between process conditions, microstructures, and mechanical properties of the deposited structures.

Microstructures and mechanical properties of low carbon steel for WAAM have been researched intensively. However, these studies mainly focused on the deposited wall structures instead of other more complex structures. In a lot of cases, complex structures are utilized to achieve different functions and purposes, such as stiffened panels with various geometries to improve the buckling index, which was mentioned and shown in Figure 2.1 and Figure 2.2. Hence, it is worth further exploring microstructures and mechanical properties of complex structures of low carbon steel fabricated by WAAM in our research because understanding of these topics is still inadequate.

More specifically, crossing structures are practical structures, which can be used in numerous applications such as bridges and metal ceilings. Besides, functionally graded components can have various properties among different parts in a component to apply in various applications. For example, functionally graded components are widely utilized in automotive and aircraft industries. However, previous research on low carbon steel fabricated via WAAM did not pay much attention to microstructures and mechanical properties of these complex structures. Therefore, in this thesis, microstructures and mechanical properties of the crossing structure as well as the functionally graded component will be investigated further.

3 Experimental methods

3.1. Welding system

In this research, Gas Metal Arc based Additive Manufacturing was performed to deposit the samples with different process parameters and strategies. In our experiments, two welding systems were utilized: a) CNC welding system b) Robotic welding system. Two welding systems have different degrees of freedom. The details of these two systems will be illustrated as follows.

3.1.1. CNC welding system

The CNC welding system (Figure 3.1) was used to perform some experiments in this research, coupled to a gas metal arc power source. The CNC welding system includes a wire feeder (Fronius VR7000), a power source (Fronius TransPuls Synergic 5000 Remote), a CNC platform, and a welding torch, connected to the CNC platform, which can move along the X, Y and Z directions. DMC Smart Terminal System was used to select the travel speed and bead length of the welding process. The Fronius RCU 5000i remote control was used to control the wire feed rate and the output of the power source. Protegon, which is mixture of 85% Argon, and 15% CO_2 ,was used as the shielding gas with a flow rate of 15 l/min. With this gas mixture, a stable process can be realized with a good surface finishing quality and a low amount of spatter [31].

Figure 3.1: CNC welding system

3.1.2. Robotic welding system

The robotic welding system (Figure 3.2) combined with gas metal arc welding was utilized to deposit the samples. The robotic welding system includes a wire feeder (Fronius VR7000), a power source (Fronius TransPuls Synergic 3200 CMT R), a welding robot (FANUC Robot M-710ic 12L), and a robot control panel to define the strategy and travel speed of the deposition. The Fronius RCU 5000i remote control was used to control the wire feed rate and the output of power source. The shielding gas Protegon was used, which is a mixture of 85% Argon, and 15% CO_2 with a flow rate of 15 l/min.

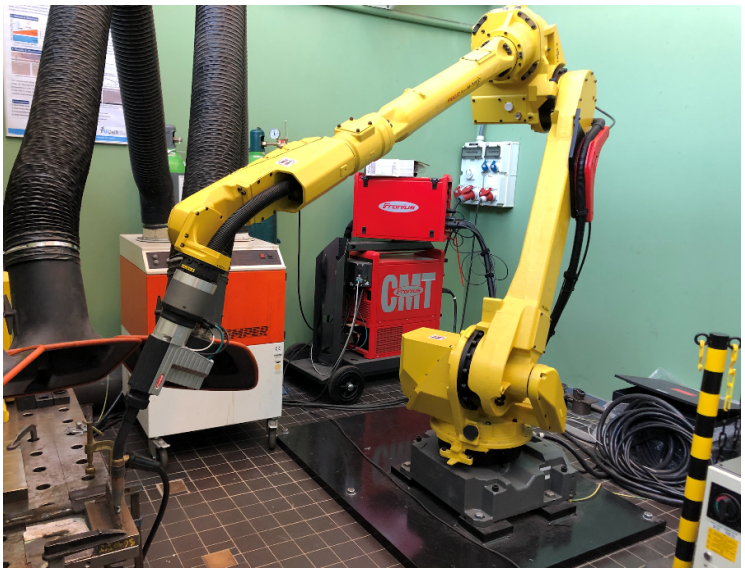

Figure 3.2: Robotic welding system

3.2. Single bead

In this research, complex structures fabricated via WAAM is the major topic of interest. However, single bead experiments provide you the fundamental understanding essential for the deposition of complex structures. Various complex structures are fabricated by sequentially depositing single beads. Therefore, researching single bead geometries and microstructure could help to realize the complex structures. Moreover, heat input plays an important role in determining the geometries, microstructure and properties of beads, and heat input is controlled by different process parameters. Hence, this section is aimed at understanding the influence of process parameters on heat input, and the influence of heat input on geometry, microstructure and properties of the single bead.

3.2.1. Experimental setup

In the experiments, the CNC welding system was used to deposit single beads. The filler wire used in the experiments is Union NiMoCr with a diameter of 1.2 mm. The composition of this wire is listed in Table 3.1. The base material used in these experiments is S235 mild steel. Dimensions of the base material were 50 × 150 × 10 mm^3. The contact tip to workpiece distance (CTWD) was 15 mm. Beads of 100 mm length were deposited. Table 3.2 lists the welding parameters for each experiment. Travel speed and wire feed rate were

varied to change the heat input. Hence, by changing the process parameters, the effect of various heat inputs on geometries, microstructure and hardness can be investigated. A vernier calliper was used to measure the width and height of the beads.

Table 3.1: The composition of Union NiMoCr

Element	C	Si	Mn	Cr	Mo	Ni	Fe
Weight Percentage (wt%)	0.08	0.6	1.7	0.2	0.5	1.5	Bal.

Table 3.2: Welding parameters for each sample

Sample no.	Wire Feed Rate (m/min)	Travel Speed(mm/s)
1	6.0	5
2	6.0	8
3	6.0	11
4	6.0	14
5	6.0	17
6	6.0	20
7	7.5	5
8	7.5	8
9	7.5	11
10	7.5	14
11	7.5	17
12	7.5	20
13	4.5	5
14	4.5	8
15	4.5	11
16	4.5	14
17	4.5	17
18	4.5	20
19	3.0	5
20	3.0	8
21	3.0	11
22	3.0	14
23	3.0	17
24	3.0	20

3.3. Optimum process parameters for the multi-pass multi-layer structure

Since complex structures usually have the multi-pass multi-layer structures, this section discusses the experimental process parameter optimization for the deposition of multi-pass multi-layer structures. Wire feed rate, travel speed, and step over increment (the distance between two adjacent beads) are crucial parameters to control the quality of the multi-pass multi-layer structures. Surface roughness, geometry of the structure, and the presence of defects are considered as the significant factors to evaluate the quality of the structure.

3.3.1. Experimental setup

For obtaining optimum process parameters for the multi-pass multi-layer structures, two-layers structures were deposited with different process parameters, and the two-layer structures were evaluated based on surface roughness, geometrical features and defects.

In this experiment, there are 14 samples of the two-layers structure fabricated according to various parameters in Table 3.3. The step over increment can be calculated according to the research of Suryakumar et al. [32], who confirmed mathematically that if the step over increment p (the distance between two adjacent beads) equals to two-thirds of the width w of the bead (shown in Figure 3.3), the roughness of the top surface of a multi-pass structure can be reduced. Hence, in this experiment, step over increments were set to two-thirds of the width of each bead, and the width values of the beads deposited with different wire feed rates and travel speeds were acquired from the single bead experiments (Table 4.1 in Chapter 4.1.1).

Table 3.3 shows the step over increment values of samples. Besides, Table 3.3 also displays the ratio of the wire feed rate to the travel speed of each sample, and this ratio represents the heat input level of the welding. Besides, this ratio from 0 to 25 can be divided into three regions: Low heat input zone(the ratio below 5), Medium heat input zone(the ratio from 5 to 15), High heat input (the ratio above 15) zone.

Table 3.3: The parameters of the 14 samples

Sample no.	Ratio (WFR/TS)	Wire Feed Rate (m/min)	Travel Speed (mm/s)	Step Over Increment (mm)
1	2.5	3	20	1.7
2	2.9	3	17	2.2
3	3.6	3	14	2.3
4	3.8	4.5	20	2.6
5	4.6	3	11	3
6	5	6	20	3.1
7	5.9	6	17	3.7
8	7.4	7.5	17	4.9
9	9.4	4.5	8	5
10	10	3	5	4.3
11	12.5	6	8	5.8
12	15.6	7.5	8	6.8
13	20	6	5	7.5
14	25	7.5	5	8.5

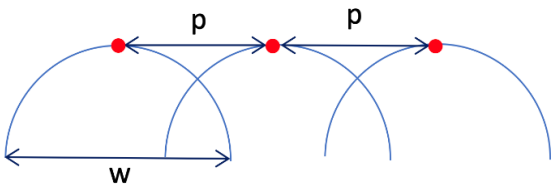

Figure 3.3: the step over increment p and width w in the multi-pass surface

Each layer of the 14 samples of two-layer structures, deposited by the CNC welding system, contained 5 beads. The depositing strategy is shown in Figure 3.4. The length of each bead was 60 mm. The wire used to deposit these samples was a Union NiMoCr and the substrate was S235 mild steel, the same as for the single bead experiments, described in Chapter 3.2. The contact tip to workpiece distance (CTWD) of 15 mm was maintained.

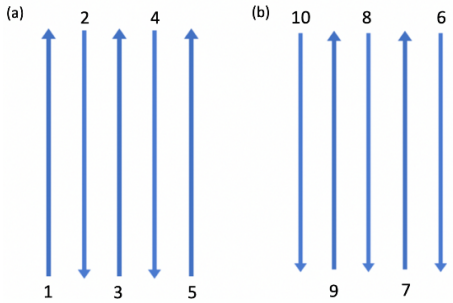

Figure 3.4: Depositing strategy for the two-layers structure. (a) first layer (b) second layer

3.4. Functionally graded component

Functional grading is achieved in a component by gradual or rapid spatial variation of microstructure or composition leading to corresponding changes in the properties of the component [33]. The goal of this research is to explore the microstructures and properties of a functionally graded rectangular block which was graded along the build direction. Functional grading in the component was accomplished by varying process parameters like travel speed and interlayer temperature.

3.4.1. Experimental setup

The functionally graded component was deposited by the Fanuc 7 axis robotic welding system. In this experiment, the wire used for depositing the functionally graded component is LNM MoNiVa, and the composition of this wire is listed in Table 3.4. The diameter of LNM MoNiVa wire was 1.2 mm. The substrate used in this experiment was S235 mild steel, and the dimensions of the substrate were 50 × 150 × 10 mm^3.

Table 3.4: The composition of LNM MoNiVa

Element	C	Si	Mn	P	S	Cr	Ni	Mo	Cu	V	Ti
Weight Percentage (wt%)	0.09	0.54	1.55	0.007	0.012	0.30	1.40	0.24	0.06	0.08	0.002
Element	Zr	N	Al	Fe							
Weight Percentage (wt%)	<0.001	0.004	0.002	Bal.							

The functionally graded component is composed of three zones along the z-direction: a) High heat input zone I, b) Low heat input zone, c) High heat input zone II. (The three zones are illustrated in Figure 3.5) Both of the high heat input zones I, II had 3 layers. Each layer contained 3 beads, and the step over increment (the distance between two adjacent beads) was set to 5.8 mm. The low heat input zone had 6 layers. Each layer contained 6 beads, and the step over increment was set to 3.1 mm. The process parameters of the high heat input zones I, II are: a wire feeding rate of 6 m/min and a travel speed of 8 mm/s. The process parameters of the low heat input zone are: a wire feeding rate of 6 m/min and a travel speed of 20 mm/s. Every bead in this functionally graded component has a length of 100 mm.

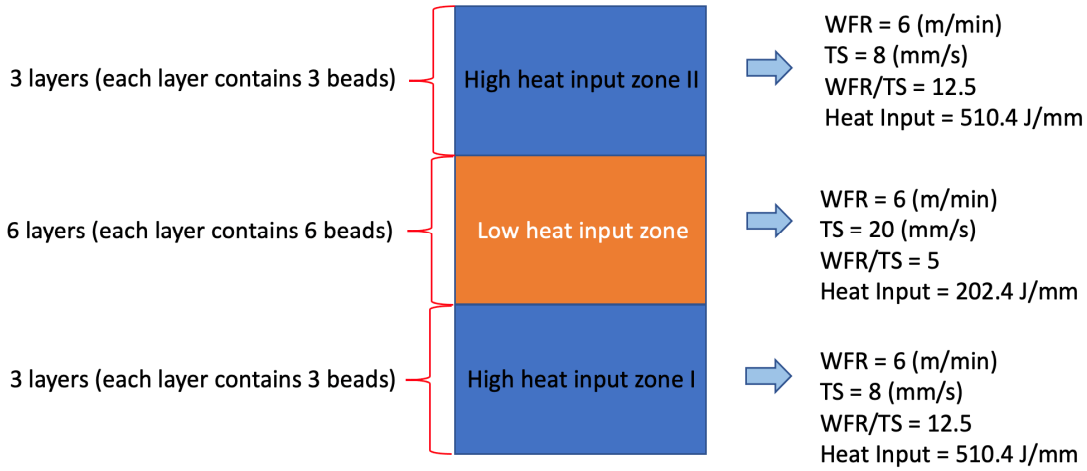

Figure 3.5: The Functionally graded component consists of three zones: a) High heat input zone I. b) Low heat input zone. c) High heat input zone II.

Figure 3.6 shows the deposition strategies of (a) high heat input zones I, II (b) low heat input zone. Before depositing functionally graded component, the substrate was preheated to 100°C. During the process of depositing the high heat input zone I, II, in each layer, the dwell time between each pass was only about 5 seconds (the time for the torch moving from the end point of one pass to the start point of the next pass). In the high heat input zones I, II, the interlayer temperature between each layer was 100°C.

After the deposition of the high heat input zone I, the low heat input zone was started to be deposited when the temperature of the high heat input zone I cooled down to 50 °C. During the process of deposition of the low heat input zone, the interbead temperature between each pass was 50°C, and the interlayer temperature

between each layer was also 50°C. After the deposition of the low heat input zone, the high heat input zone II was deposited when the temperature of the low heat input zone had cooled to 100 °C.

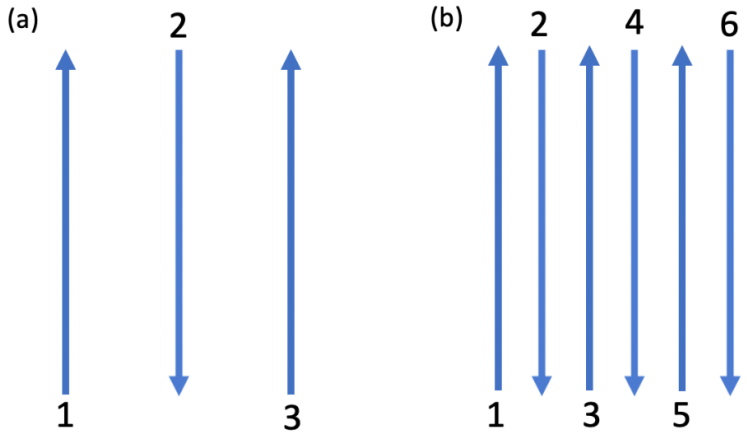

Figure 3.6: The deposition strategies of (a) high heat input zones I, II (b) low heat input zone

3.5. Crossing structures

As mentioned in Chapter 2, most previous researches about low carbon steel for WAAM only focused on thin wall structures instead of other more complex structures. Therefore, in this research project, crossing shaped features were selected and the thermal history, microstructure and mechanical properties were explored.

3.5.1. Sample buildup

In the experiments, two crossing structures were deposited by the Fanuc 7 axis robotic welding system. Two crossing structures were fabricated with the same material, the same wire feed rate, the same travel speed, and the same deposition toolpath. However, there are two differences: (a) one of the crossing structures was fabricated with the interlayer temperature of 100°C between adjacent layers. (b) the second crossing structure was fabricated with the interlayer time of 90 sec between adjacent layers. Moreover, the different arrangements of thermocouples applied to these structures will be illustrated later.

In the experiment of the crossing structures, the material of the wire is a 1.2 mm diameter LNM MoNiVa. The compositions of the wires used in the crossing structure and the previous functionally graded component are different. The composition of this wire used in the crossing structure is shown in Table 3.5. The substrate used in this experiment was a S690 steel, and the dimensions of the substrate were 225 × 225 × 25.5 mm^3.

Table 3.5: The composition of LNM MoNiVa

Element	C	Si	Mn	P	S	Cr	Ni	Mo	Cu	V	Al	Fe
Weight Percentage (wt%)	0.065	0.54	1.63	0.006	0.012	0.30	1.47	0.24	0.06	0.09	0.003	Balance

The process parameters for building up both crossing structures are: a) wire feed rate 4.5 m/min b) travel speed 8 mm/s. The deposition strategy for both crossing structures is shown in figure 3.7. Each layer has two passes, and the length of each pass is 180 mm. Besides, after a layer has been deposited, the torch ascended a height of 1.2mm before depositing the next layer. In each layer, the time between two passes is about 10 seconds, which is the time for the torch to move from the end point of the first pass to the start point of the second pass. Finally, the deposition was repeated until the final structure had 20 layers.

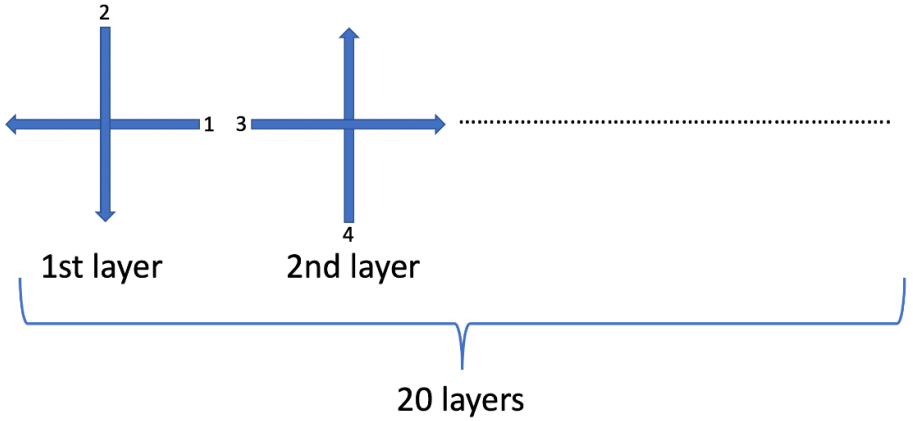

Figure 3.7: the strategy for depositing both crossing structures (top view)

3.5.2. Thermal cycles measurement

To record the thermal history of the depositing process of the crossing structures, Type K thermocouples were used. Thermocouples were attached to the substrates and the crossing structures for measuring and recording the temperature at different tracking points. The arrangement of thermocouples for the crossing structure fabricated with the interlayer temperature of 100°C and the crossing structure fabricated with the interlayer time of 90 sec are described below separately.

3.5.2.1. Setup of thermocouples for crossing structure fabricated with interlayer temperature of 100°C between adjacent layers

There were 7 tracking points in the experiment of the crossing structure fabricated with the interlayer temperature of 100°C. Thermocouples were attached at tracking points A, B, C, D on the substrate before depositing the crossing structure, and thermocouples were attached at tracking points E, F, G on the wall of centre points of the crossing structure along the building direction during the depositing process. Tracking points A-G are shown in the Figure 3.8.

Tracking point E was attached on the 5th layer after the 6th layer finished, and its height is around 11 mm from the substrate. However, the thermocouple of tracking point E got burned off while the 16th layer was deposited, so tracking point E recorded the complete thermal cycles corresponding to the deposition of the layer 7th to the layer 15th. Tracking point F was attached on the 10th layer after the 11th layer finished, and its height is around 15.5 mm from the substrate. Tracking point F recorded the complete thermal cycles of

the deposition of the layer 12th to the layer 20th. Tracking point G was attached on the 15th layer after the 16th layer finished, and its height is around 24.4 mm from the substrate. Tracking point G recorded the complete thermal cycles corresponding to the deposition of the layer 17th to the layer 20th.

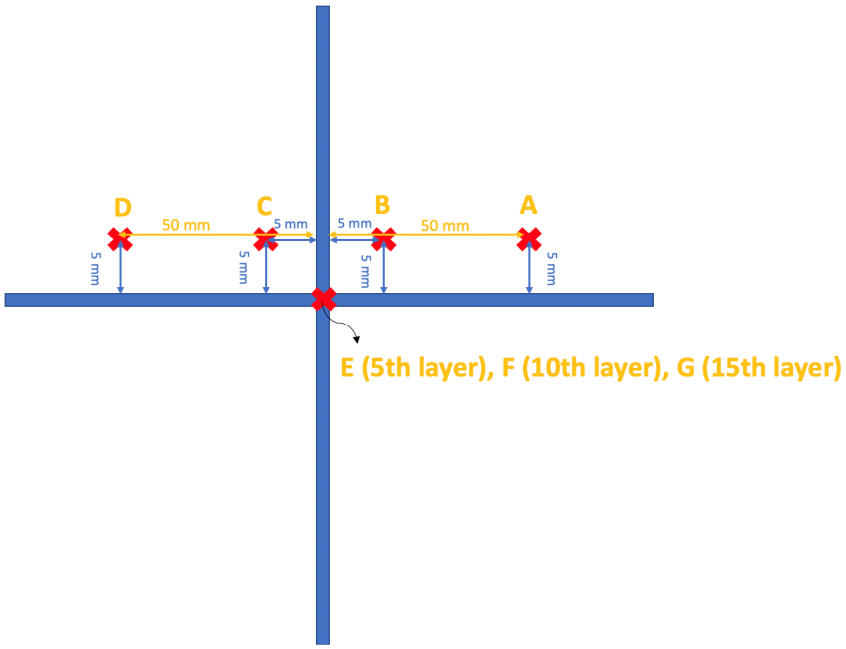

Figure 3.8: Top view of locations of the thermocouples (crossing structure fabricated with the interlayer temperature of 100°C)

3.5.2.2. Setup of thermocouples for crossing structure fabricated with interlayer time of 90 sec between adjacent layers

There were 7 tracking points in the experiment of the crossing structure fabricated with the interlayer time of 90 sec: thermocouples were attached at tracking points A', B', C', D' on the substrate before depositing the crossing structure, and thermocouples were attached at tracking points E', F', G' on the side wall of the crossing structure along the building direction during the depositing process. Tracking points A'-G' are shown in the Figure 3.9.

Tracking point E' attached on the 8th layer after the 9th layer finished. Tracking point E' failed while the 13th layer was deposited so tracking point E' recorded the complete thermal cycles of the deposition of the layer 10th to the layer 12th. Tracking point F' was attached on the 13th layer after the 15th layer finished, and its height is around 20 mm from the substrate. Tracking point F' recorded the complete thermal cycles corresponding to the deposition of the layer 16th to the layer 20th. Tracking point G' was attached on the 15th layer after the 17th layer finished, and its height is around 23.0 mm from the substrate. Tracking point G' recorded the complete thermal cycles corresponding to the deposition of the 18th layer to the 20th layer.

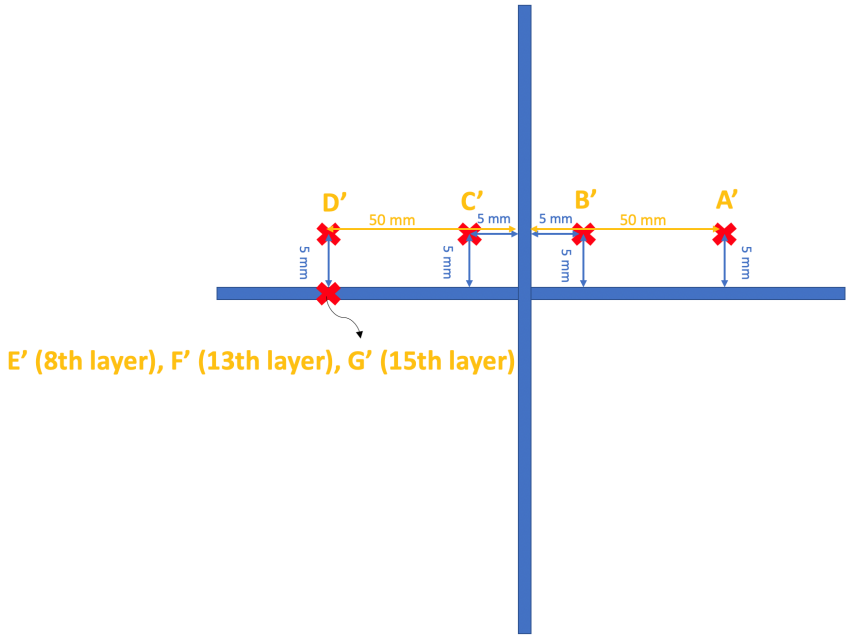

Figure 3.9: Top view of locations of the thermocouples (crossing structure fabricated with the interlayer time of 90 sec)

3.5.3. Thermal simulation of crossing structure

Even though the crossing structure fabricated with the interlayer time of 90 sec has been deposited and the thermal history has been measured, the result could be incomplete due to the limitations of the experiment. For example, it was too difficult to record the whole thermal history at a tracking point because the thermocouple could fail during the welding process. Besides, it was not easily to attach the thermocouple to the desired location precisely. Moreover, the error of thermocouple occurs frequently due to the interference from the arc and the inhomogeneous composition in the wire. For further understanding the thermal history and the microstructure of the deposition of the crossing structure, the use of thermal simulations of the crossing structure is an effective method to investigate it.

All methodology and the result of the thermal simulation in this thesis have been designed and provided by Rutger Schreurs, a graduate student in Mechanical Engineering department in TU Delft. Figures 3.10 and Figure 3.11, Equations (1) to (3), Table 3.6, and paragraphs in Chapter 3.5.3.1. to Chapter 3.5.3.3. were compiled according to the methodology provided by Rutger Schreurs. The detailed information of this thermal simulation can be found in the master thesis of Rutger Schreurs.

3.5.3.1. Material composition and properties

For this simulation, the selected material is LNM MoNiVa wire, which is the same as the wire used in the crossing structure experiment mentioned above. However, the thermal properties of the S690QL1 HSLA steel were utilized because the information about the thermal properties of LNM MoNiVa was still insufficient. S690QL1 HSLA steel and LNM MoNiVa has a similar yield strength. However, the compositions of these two steels are dissimilar. The composition of S690QL1 HSLA steel is shown in Table

3.6. Figure 3.10 shows the temperature dependent material properties of S690QL1, which were obtained by He Gao [34].

Table 3.6: The composition of S690QL1 [34]

Element	C	Mn	P	S	Cr	Ni
Weight Percentage (wt%)	0.16	0.86	0.04	0.0007	0.32	0.075
Element	Mo	Cu	Nb	Ti	P	Fe
Weight Percentage (wt%)	0.18	0.015	0.03	0.006	0.04	balance

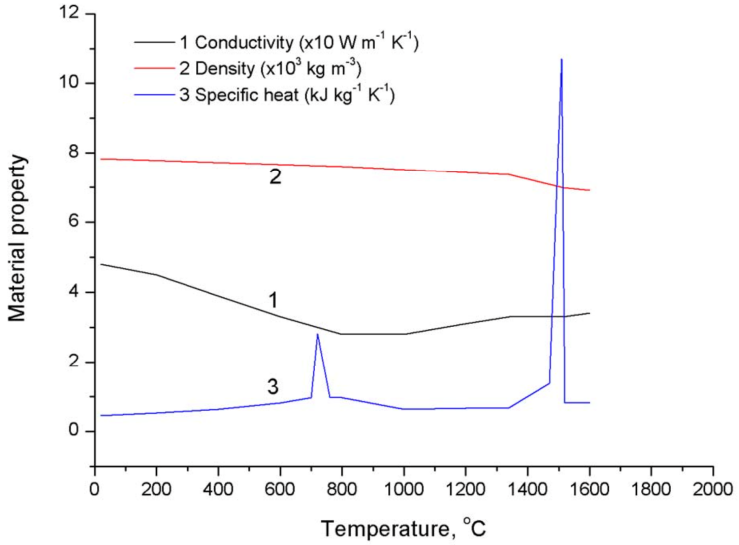

Figure 3.10: Material properties of S690QL1 utilized in the thermal process model [34]

3.5.3.2. Heat transfer equations

The conservation of energy equation was used as the governing equation describing the physics of the thermal model [35]:

$$\frac{\partial(\rho c T)}{\partial t} = \nabla \cdot (\lambda \nabla T) + Q_{HS} \quad (1)$$

where ρ = temperature dependent density, c = temperature dependent specific heat capacity, T = temperature, t = time, λ = temperature dependent thermal conductivity and Q_{HS} = addition of the heat from the heat source [35][36].

Generally, heat losses in the thermal modelling of the additive manufacturing were applied as boundary conditions to Eq. (1). Heat losses occur due to convection, radiation, and conduction to the base plate. The equations of the heat loss (Q_C) due to convection and the heat loss (Q_R) due to radiation are shown below [36]. For conduction to the base plate, an conduction coefficient of 300 W/(m^{2}K) was utilized [36][37].

$$Q_C = h(T_0 - T) \quad (2a)$$

$$Q_R = \beta E({T_0}^4 - T^4) \quad (2b)$$

where h = heat convection coefficient, T_0 = ambient temperature (i.e. 20 °C), T = temperature, β = Stefan-Boltzmann constant (i.e. 5.67×10^{-8} $Wm^{-2}K^{-4}$)[35]), E = the emissivity of the material.

One of the most common model used for describing the arc welding process is the Goldak double-ellipsoidal model. The power density distribution inside the front region (Q_f) and the rear region (Q_r) [37-42]:

$$Q_f(x,y,z,t) = \frac{6\sqrt{3}\eta Q_{HS} f_f}{L_f W D \pi \sqrt{\pi}} exp\left(-\frac{3(x-V_{HS}t)^2}{{L_f}^2} - \frac{3y^2}{W^2} - \frac{3z^2}{D^2}\right) \quad (3a)$$

$$Q_r(x,y,z,t) = \frac{6\sqrt{3}\eta Q_{HS} f_r}{L_r W D \pi \sqrt{\pi}} exp\left(-\frac{3(x-V_{HS}t)^2}{{L_r}^2} - \frac{3y^2}{W^2} - \frac{3z^2}{D^2}\right) \quad (3a)$$

where L_f = length of the frontal region of the weld pool (i.e. 3.75 mm), and L_r = length of the rear region of the weld pool (i.e. 11.25 mm), W = weld pool's width (i.e. 3.75 mm), D = weld pool's depth (i.e. 2.5 mm), η = thermal efficiency of the heat source (i.e. 0.9 [37]), Q_{HS} = heat source power (i.e. 3715 W), V_{HS} = travel speed of the heat source (i.e. 8 mm/s), f_f and f_r = power distribution factors for the frontal and rear of the hear source (f_f = 0.6 and f_r= 1.4 [37]). Goldak heat source does not account for conduction within the weld pool. Hence, for considering this effect, the thermal conductivity of liquid metal is increased to 120 W/(m K) [37][40][43].

3.5.3.3. Sample deposition

The deposition strategy for the crossing structure in this simulation was the same as the strategy to deposit the crossing structure mentioned in Figure 3.7. The final crossing structure had 20 layers on a substrate with dimensions 225 × 225 × 25.5 mm^3. The interlayer time between adjacent layers was 90 sec.

Modelling of material deposition is achieved by using the quiet element method (shown in Figure 3.11). In the quiet element method, the value multiplied by material properties of the non-deposited regions is downscaled to a very low value (i.e. 10^{-6}). For obtaining material properties in the quiet region, the material properties were multiplied with this low value (i.e. 10^{-6}). During the deposition of materials, the material properties were scaled back to their normal value.

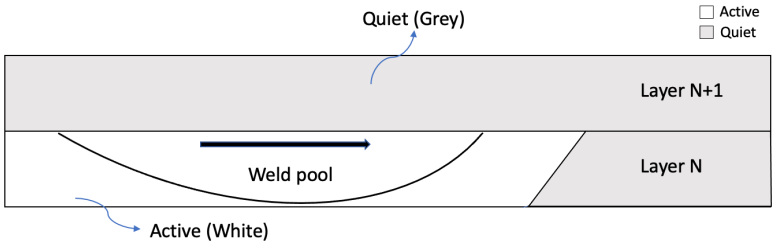

Figure 3.11: Quiet element method

3.6. Characterization techniques

3.6.1. Microscopic evaluation

Three kinds of microscopes were utilized for the characterization of the microstructures: optical microscope (Leica DM LM), digital microscope (VHX-5000), and scanning electron microscope (JSM-IT100).

The optical microscope magnifies an image through a combination of lenses. The optical microscope has a range of objective lenses, allowing a magnification up to 1000x. The digital microscope uses optics and a digital camera to show a live image on a monitor. The observation by the digital microscope is fast and convenient because the different functions, such as auto-focus, stitched image, sharpen mode, and distance measurement, can be activated through the software and the controller [44].

A scanning electron microscope (SEM) was used to observe the microstructures at higher magnifications. During the operation of a SEM, an electron beam is applied to the sample, and the electrons interact with the sample. The effects of the interaction between the electrons and the sample can be captured and analyzed to acquire the desired information. The scanning electron microscope features three types of detectors: a Secondary Electron Detector (SED), an Electron Back-Scattered Detector (EBSD), and an Energy Dispersive Spectrum Detector (EDS) [45].

For characterizing the microstructures by these microscopes, the samples were prepared according to the following procedures. Firstly, the sections to be observed were acquired from the deposited structures by a cutting machine. The samples were then ground with P80 to P2000 grit paper. Subsequently, the samples were polished from with a diamond colloidal solution with particle size 3μm to 1μm. After the polishing process, the samples were etched with Nital (2% Nitric acid in ethanol) to reveal the microstructure of the metal through selective chemical attack.

3.6.2. Hardness measurement

The Vickers hardness of samples was measured with the hardness measurement device (Struers GmbH DuraScan 70). Hardness is a characteristic feature of a material, and it can be defined as the resistance to indentation. The Vickers hardness test method is based on an optical measurement system. The microhardness test procedure involves using a range of loads to make an indentation on the material. In this research, the loads of 1 Kg and 200 g were used to make indentations. A square base pyramid shaped diamond is used for making the indent. The average of the two diagonals of the indent and the applied load (shown in Figure 3.12) are used for calculation of the Vickers hardness in the software. For measuring the diagonals of the indent accurately, the microscope is utilized and the sample needs to be polished before the hardness measurement to make the indent clearly shown on the image [46][47].

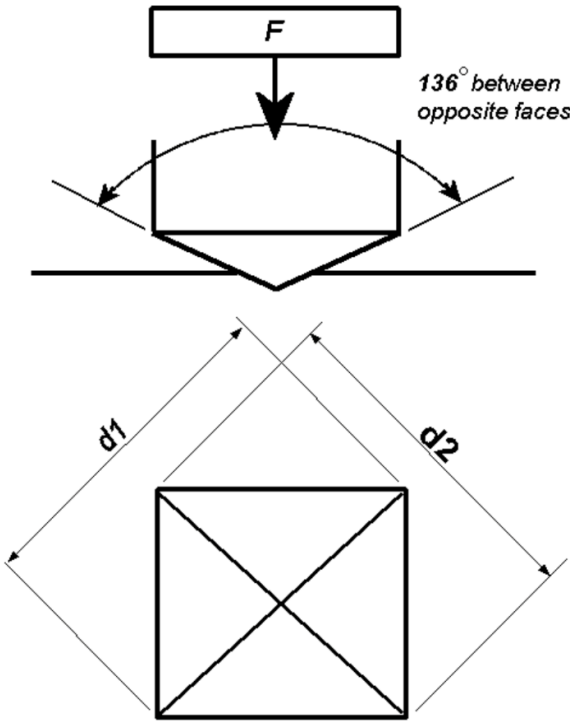

Figure 3.12: The Vickers hardness test

4 Result and discussion

The approach of this study is divided into a part considering single beads to obtain relationships between processing conditions, bead geometry, microstructure evolution, and mechanical properties (in particular the hardness). From the obtained results, appropriate welding conditions were selected to fabricate the more complex structures, i.e. functionally graded parts and crossing structures.

4.1. Single bead

Figure 4.1(a), Figure 4.1(b), and Figure 4.1(c) show macroscopic images of the single beads. The sample numbers are indicated in these figures. The welding conditions for each of the samples are listed in Table 4.1. The measured voltage and current combined with the travel speed result in a certain heat input. The measured heat inputs, geometrical aspects, microstructures, and hardness are presented, and the relationship between them are discussed in this chapter.

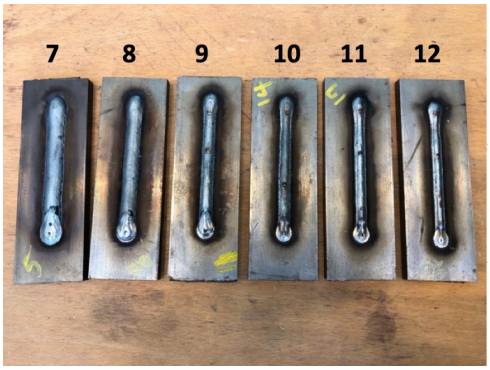

(a) sample 7-12

(b) sample 13-18

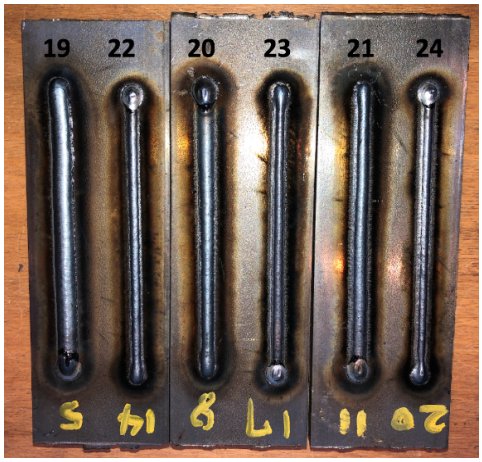

(c) sample 19-24

Figure 4.1: Bead appearance of a) samples 7-12, b) samples 13-18, c) samples 19-24

4.1.1. Relationship between Heat input and process parameters

The heat input was measured and calculated by Eq. (4)

$$\mathrm{HI} = \eta \frac{\frac{1}{n}\sum V_i \cdot I_i}{V_s} = \eta \frac{W}{V_s} \quad (4)$$

where V_i is the instantaneous voltage (V) at each recorded point in the stable part of AMV3500 waveform (an illustrative picture shown in Figure 4.2), I_i is the instantaneous current (A) at each recorded point in the stable part of AMV3500 waveform, n is the amount of recorded points in the stable part of AMV3500 waveform, W is the average welding power (J/s) in the stable part of AMV3500 waveform, V_s is the welding travel speed (mm/s), η is the thermal efficiency factor for the welding process, and η = 0.8 is taken here [48]. Figure 4.3 shows the partial enlargement figure of a stable part of AMV3500 waveform in the illustrative picture in Figure 4.2.

The detailed mechanisms of welding process can be explained in Figure 4.3:

1. From point a to point b: point a is the starting of the pulse time. As the current increases from the background level to the peak value, the intensity of the arc light gets stronger, and the wire tip starts melting.
2. At point b: the peak current is achieved, and the droplet is formed.
3. From point b to point c: the arc light intensity is strongest, and the droplet grows.
4. At point c: point c is the end of the pulse time. At point c, the current starts to change from the peak value to the lower current, the droplet is detached from the wire tip and jumps into the weld pool.
5. From point c to point d: the section between point c to point d is cooling off period. Pulsed GMAW drops the current as extra power is not needed. Hence, the cooling off of the process occurs from point c to point d.
6. At point d: background current is achieved, and this is the current required to maintain the arc. The background current keeps the arc, but it is too low for metal transfer to happen [49][50].

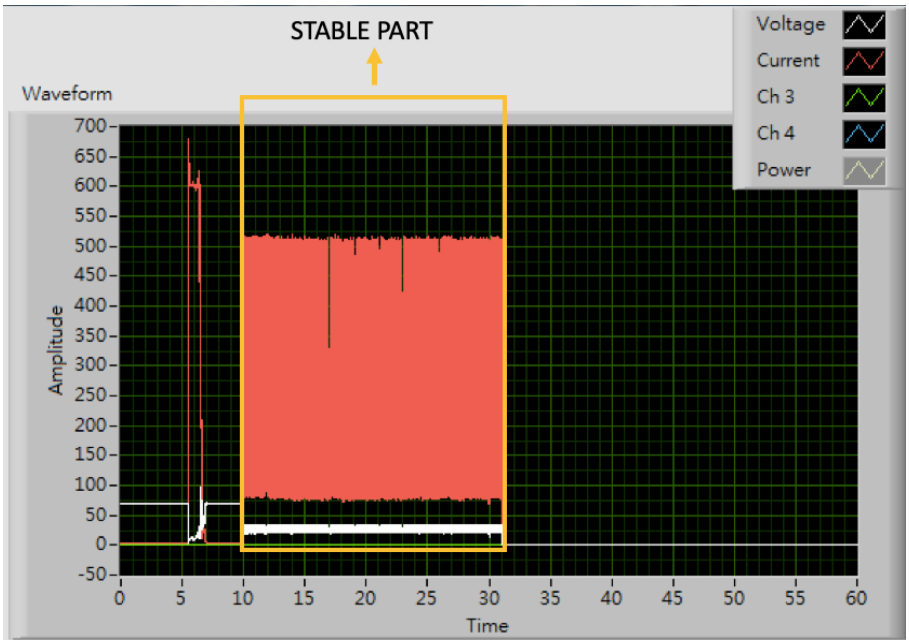

Figure 4.2: the illustrative picture of AMV3500 waveform

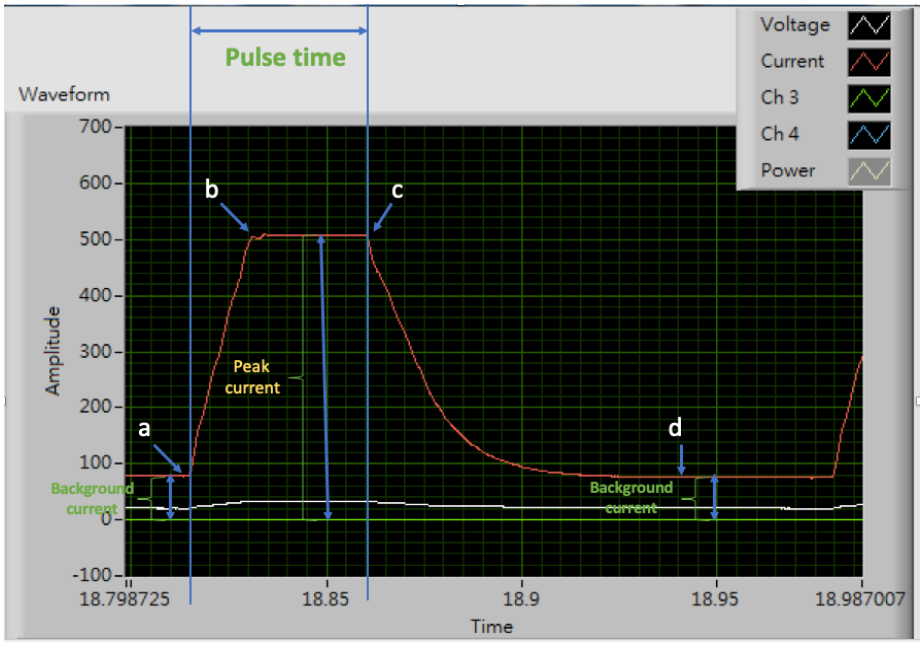

Figure 4.3: the partial enlargement figure of stable part of AMV3500 waveform in the illustrative picture

The heat input of each sample is shown in Table 4.1. Figure 4.4 shows the effect of the travel speed on the heat input for a fixed wire feed rate of 6 m/min. According to Figure 4.4, when the travel speed increases, the heat input decreases. This is because the heat input is the average welding power divided by travel speed (see Eq. (4)).

Table 4.1: The welding conditions and the measurement results of the geometry of sample 1 to 24

no.	Wire Feed Rate (m/min)	Travel Speed (mm/s)	Ratio (WFR/V_t)	Average Voltage (V)	Average Current (A)	Heat Input (J/mm)	Width (mm)	Height (mm)
1	6.0	5	20	23.5	178.7	812.8	11.17	2.98
2	6.0	8	12.5	23.4	179.3	510.4	8.67	2.43
3	6.0	11	9.1	23.8	180.4	376	7.95	2.08
4	6.0	14	7.1	23.3	178.4	290.4	6.65	1.87
5	6.0	17	5.9	23.3	177.7	237.6	5.48	1.72
6	6.0	20	5	23.3	177.3	202.4	4.62	1.5
7	7.5	5	25	25.4	222.7	1045.6	12.67	3.23
8	7.5	8	15.6	25.3	220.1	646.4	10.17	2.57
9	7.5	11	11.4	25.3	219.3	470.4	8.73	2.3
10	7.5	14	8.9	25.4	221	372	7.5	1.93
11	7.5	17	7.4	25.5	215.8	302.4	7.27	1.8
12	7.5	20	6.3	25.3	214	253.6	6.45	1.72
13	4.5	5	15	21.8	129.3	576.8	8.78	2.75
14	4.5	8	9.4	22.4	130.1	378.4	7.48	2.05
15	4.5	11	6.8	21.8	131.2	264	6.13	1.85
16	4.5	14	5.4	21.8	135.9	214.4	5.58	1.5
17	4.5	17	4.4	21.7	131.5	171.2	4.73	1.35
18	4.5	20	3.8	21.4	129.9	144	3.93	1.28
19	3.0	5	10	20.8	88	396.8	6.4	2.15
20	3.0	8	6.3	21	90.8	259.2	4.88	1.75
21	3.0	11	4.6	20.9	84.2	172.8	4.47	1.7
22	3.0	14	3.6	21	79.9	130.4	3.38	1.47
23	3.0	17	2.9	21.6	81.8	111.2	3.22	1.28
24	3.0	20	2.5	21	87.1	99.2	2.48	1.15

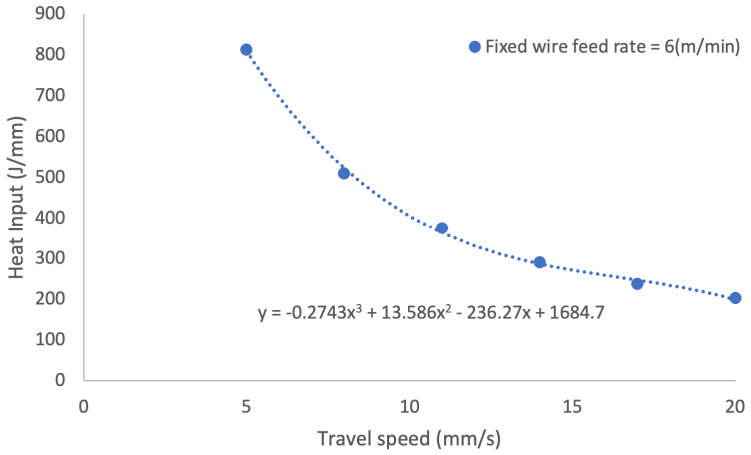

Figure 4.4: The effect of the travel speed on the heat input (WFR=6 m/min)

Figure 4.5 shows the effect of the wire feed rate on heat input for a fixed travel speed of 5 mm/s. Figure 4.5 shows that the heat input becomes larger with an increase in the wire feed rate. The reason for this tendency is that an increase in the wire feed rate increases the welding current. The welding power divided by the travel speed equals to the heat input (see Eq. (4)), and welding power is the product of welding current and arc voltage. Hence, higher wire feed rates lead to higher heat inputs [51].

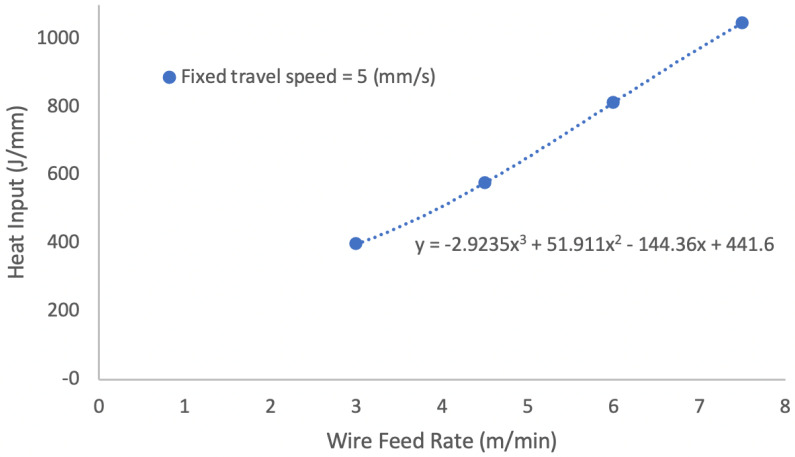

Figure 4.5: The effect of the wire feed rate on the heat input (V_t=5 mm/s)

Moreover, the ratio of the wire feed rate to the travel speed is also illustrated in Table 4.1. Figure 4.6 shows the variation of heat input with increasing WFR/V_t ratio. As the ratio of the wire feed rate to the travel speed becomes larger, the heat input also increases. This result corresponds to the trends described above, which indicated that the travel speed is in inverse ratio to the heat input, and the wire feed rate is in direct ratio to the heat input. Hence, the higher ratio of the wire feed rate to the travel speed can represent the higher level of the heat input of the welding process, leading to more metal deposited per unit length. The WFR/V_t ratio from 0 to 25 can be divided into three regions: Low heat input zone (ratio below 5), Medium heat input zone (ratio from 5 to 15), High heat input zone (ratio above 15).

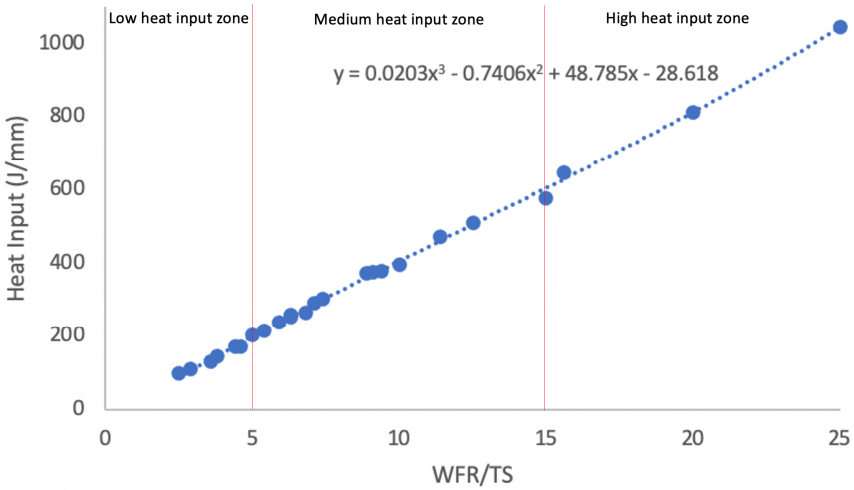

Figure 4.6: The effect of the ratio(WFR/V_t) on the heat input

4.1.2. Effect of heat input on width and height of bead

Figure 4.7 and Figure 4.8 separately illustrate the effect of the heat input on the width and the height of the bead. Figure 4.7 shows the tendency that when the heat input increases, the bead width also becomes larger; Figure 4.8 depicts that the height tends to become larger with higher heat input. In other words, when the heat input increases, the bead width as well as bead height show the tendency to increase. The reason for this tendency is that as the heat input becomes larger, more metal is deposited per unit length, which increases both width and height of the bead.

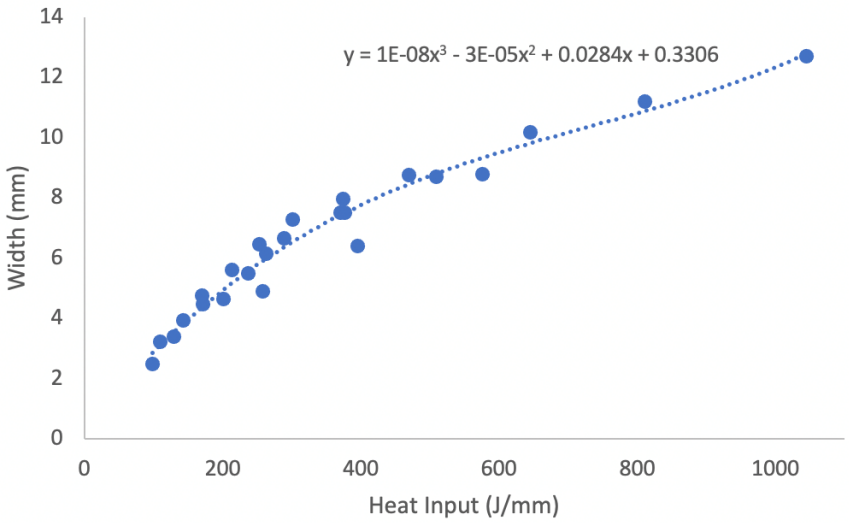

Figure 4.7: The effect of the heat input on the bead width

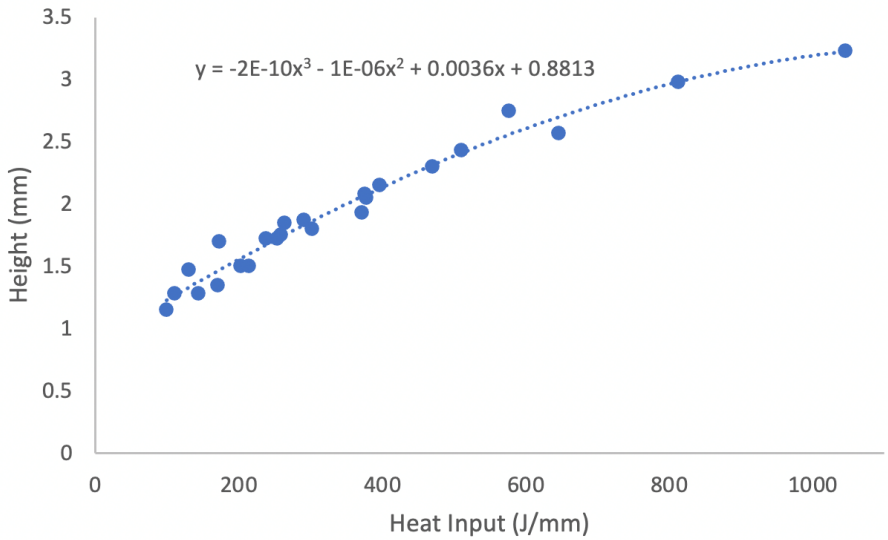

Figure 4.8: The effect of the heat input on the bead height

4.1.3. Effect of heat input on microstructure and hardness

The heat input, and the hardness of sample 1 to sample 6 have been measured and are presented in Table 4.2. Figure 4.9 illustrates the effect of the heat input on the hardness, showing that as the heat input increases, the hardness decreases. The main reason for decreasing hardness with increasing heat input is that the increasing amount of the heat input or the higher level of the heat input leads to a lower cooling rate [3], resulting in a lower fraction of martensite and a higher fraction of ferrite in the bead. Because martensite has a higher hardness compared to ferrite, a lower fraction of martensite and a higher fraction of ferrite decrease the hardness of the sample. The relationship between heat input, microstructure, and hardness will be discussed further with the aid of microstructural images of sample 1 to sample 6 (shown in Figure 4.10).

Table 4.2: The measurement results of sample 1 to sample 6

Sample no.	Wire Feed Rate (m/min)	Travel Speed (mm/s)	Heat Input (J/mm)	Hardness (HV)	Standard Deviation (HV)
1	6.0	5	812.8	269	10
2	6.0	8	510.4	289	5
3	6.0	11	376	338	8
4	6.0	14	290.4	379	4
5	6.0	17	237.6	416	5
6	6.0	20	202.4	446	5

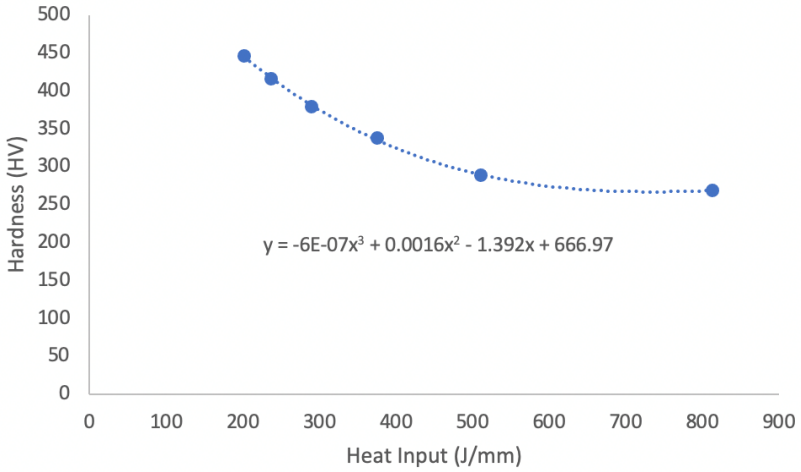

Figure 4.9: The effect of the heat input on the hardness

Figure 4.10(a)-(f) show the microstructures of the beads of sample 1 to sample 6. In Figure 4.10(a)-(c), ferrite dominates in the microstructures. Ferrite is a soft phase, and it can be classified into four types depending on the morphologies. As the name suggests, grain boundary ferrite nucleates at prior austenite grain boundaries and can be observed in Figure 4.10(a). It is also known as allotriomorphic ferrite. It can be seen that grain boundary ferrite forms as coarse crystals [52]. Another type of ferrite is shown in Figure 4.10(c): Polygonal ferrite. Both austenite grain boundaries and intragranular regions are the potential

locations for the nucleation of polygonal ferrite. The morphology of polygonal ferrite is in the form of coarse isolated ferrite islands embedded in the matrix [35][53]. In addition to the above categories of relatively coarse ferrite, Figure 4.10(c) also shows side plate ferrite, also known as Widmanstätten ferrite. The shape of the side plate ferrite looks like needles due to cross sectioning, but actually consists of parallel plates growing from the prior austenite grain boundary into the austenite grain [35]. Furthermore, acicular ferrite can be observed in Figure 4.10(a) with a thin and lenticular morphology. The name "acicular" of this ferrite was given by its need-shape grains. Acicular ferrite often nucleates on non-metallic inclusions and is radially growing from these nucleation points [23][35].

Another phase is bainite indicated in Figure 4.10(d)-(e). Bainite consists of ferrite plates and cementite particles. Grain boundaries of the former austenite are the potential nucleation sites of the bainite [52]. Bainite can be classified into upper bainite (formed at about 550°C - 400°C), and lower bainite (formed at about 400°C - 250°C). It also can be classified into different categories by its morphology and formation mechanisms (as mentioned in Table 2.2 in Chapter 2). A clear distinction between upper and lower bainite requires high magnifications to distinguish the location of the carbides.

In Figure 4.10(e)-(f), the martensitic phase dominates the microstructures. When the steel cools to room temperature at a sufficiently high cooling rate to avoid other phase transformation such as ferrite and bainite, martensite is formed. The velocity of the transformation interface is faster than that of the velocity of carbon diffusion. Hence, the carbon gets trapped at high cooling rate, which leads to the formation of martensite, a needle-like microstructure with high hardness [23].

According to Figure 4.10(a)-(f), the amount of ferrite decreases from sample 1 to sample 6. This decrease is due to the decreasing heat input from sample 1 to sample 6, with an associated increasing cooling rate. The increasing cooling rate from sample 1 to sample 6 promotes martensite formation. Bainite formation mainly occurs because the beads underwent the medium cooling rate, i.e. samples 4 and 5. Moreover, the increasing order of the level of the hardness among these microstructural constituents is from ferrite via bainite to martensite. This is in line with the hardness results presented in Table 4.2.

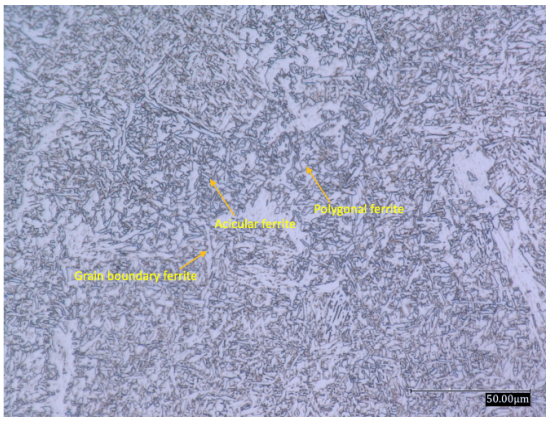

(a) sample 1

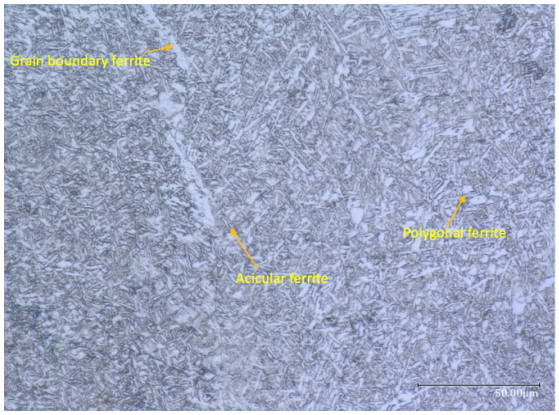

(b) sample 2

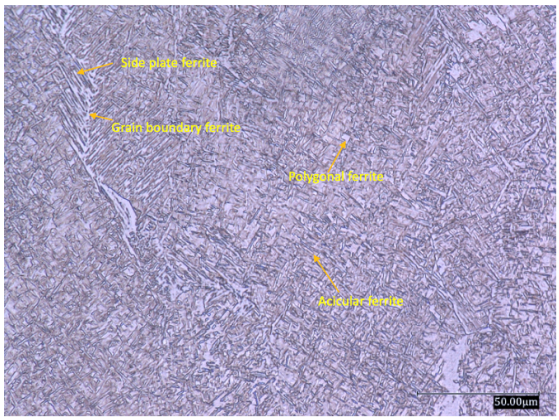

(c) sample 3

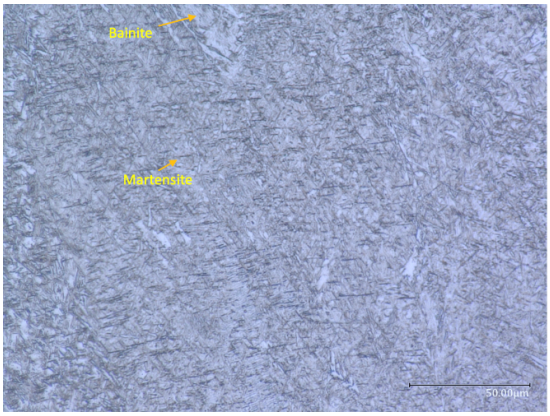

(d) sample 4

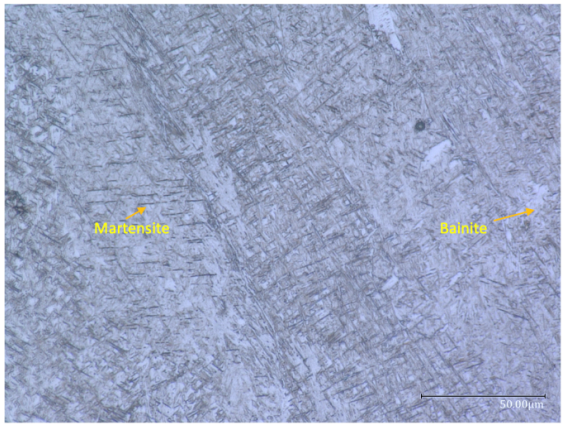

(e) sample 5

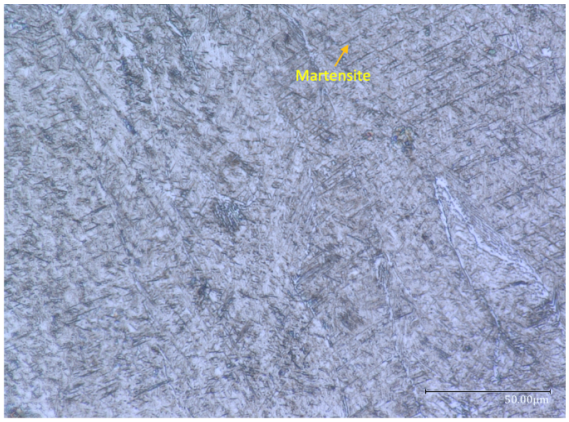

(f) sample 6

Figure 4.10: the images of microstructures of sample 1 to sample 6

4.2. Optimum process parameters for the multi-pass multi-layer structure

4.2.1. Evaluation of multi-pass multi-layer structure

The optimum wire feed rate and the optimum travel speed for multi-layer geometries are determined based on the geometry and defects of the deposited two-layers structures. Besides, surface roughness is another important index to be used for evaluating the samples.

4.2.1.1. Defect

The top view photos of the 14 samples fabricated according to the parameters in Table 3.3 are listed in Table 4.3. The defects formed during the welding process need to be avoided for achieving the high-quality structures.

According to Table 4.3, samples 1 to 5 show defects, which are in the form of depressions on the top surfaces of structures. The defects are marked by yellow dashed circles. This indicates that, when the ratio of the wire feed rate to the travel speed is equal to or less than 4.6, the defects (depressions) are formed on the structure. The reason of the formation of the porous structure is that the travel speed was too high, and the amount of feeding material was not enough to deposit the bead uniformly with this high travel speed. Also, as the ratio of the wire feed rate to the travel speed is equal or less than 4.6, the structures with the same wire feed rate become much more porous with the drastically rising of travel speed. For example, sample 1 and sample 3 both have the same wire feed rate (3 m/min), but because sample 1 has much higher travel speed (20 mm/s) than the travel speed (14 mm/s) of sample 3, this structure shows far more depressions.

Therefore, for preventing occurrence of porous defects and obtaining high-quality structures, parameters with the ratio greater than 4.6 are chosen.

Table 4.3: The top views of the 14 samples

No.	1	2	3
Top view		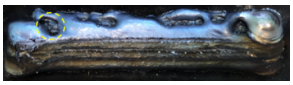	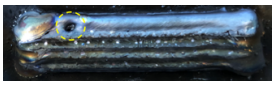
No.	4	5	6
Top view	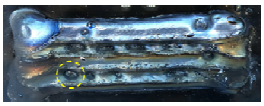	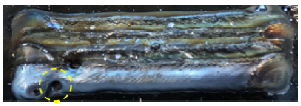	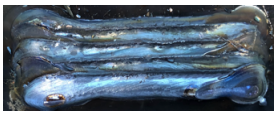
No.	7	8	9
Top view		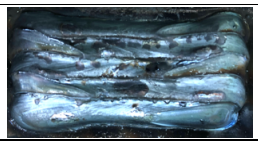	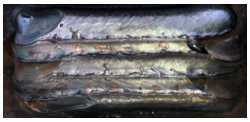
No.	10	11	12
Top view	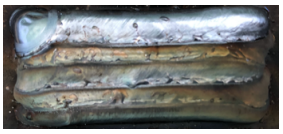		
No.	13	14	
Top view	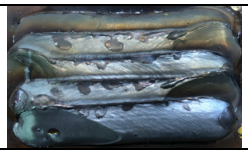		

4.2.1.2. Surface roughness

The mean peak-to-valley roughness was used to evaluate the surface quality, and it was calculated by Eq. (5),

$$\text{Roughness} = \frac{Z1 + Z2 + Z3 + Z4}{4} \quad (5)$$

where Z1, Z2, Z3, Z4 are the distances between the lowest valley point to the highest peak point, illustrated in Figure 4.11 [54]. The range of roughness can represent different surface qualities: a) a roughness < 0.4, indicates a good surface quality; b) a roughness between 0.4 and 0.6, shows an acceptable surface quality; c) a roughness ≥ 0.6, can be associated with a poor surface quality.

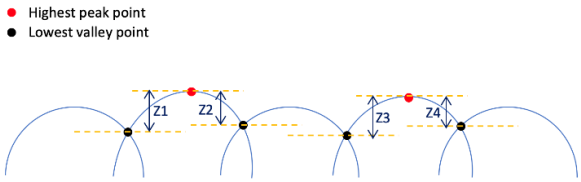

Figure 4.11: Z1, Z2, Z3, Z4, distances between the lowest valley point to highest peak point

The cross sectional images of the 14 samples are listed in Table 4.4. The roughness values calculated by Eq. (5) are shown in Table 4.5.

Table 4.4: The sectional views of the 14 samples

No.	1	2	3
Sectional view	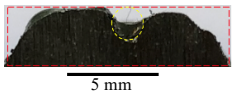	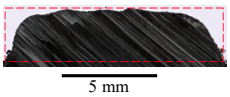	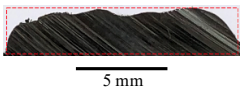
No.	4	5	6
Sectional view	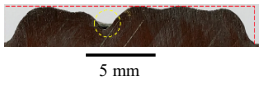	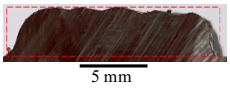	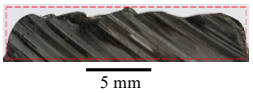
No.	7	8	9
Sectional view	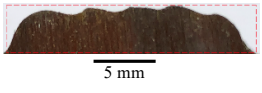	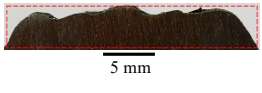	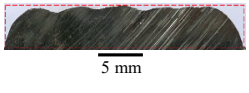
No.	10	11	12
Sectional view	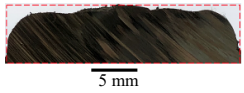	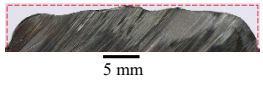	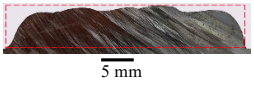
No.	13	14	
Sectional view	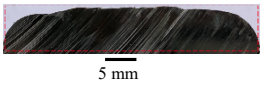	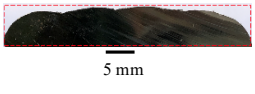	

Table 4.5: Roughness of 14 samples

Sample no.	**Roughness (mm)**	**Surface quality**
1	0.6	Poor
2	0.14	Poor*
3	0.43	Poor*
4	0.64	Poor
5	0.3	Poor*
6	0.51	Acceptable
7	0.52	Acceptable
8	0.55	Acceptable
9	0.39	Good
10	0.47	Acceptable
11	0.58	Acceptable
12	0.67	Poor
13	0.4	Acceptable
14	0.59	Acceptable

*: Even though roughness values of sample 2, 3, 5 are below 0.5, their surface qualities are still poor because the defects(depressions) exist on the other cross-sections, leading to a poor surface quality.

According to Table 4.4 and Table 4.5, sample 9 has the best surface quality, sample 6-8, 10, 11, 13, 14 have an acceptable surface quality, and sample 1 to 5, and 12 show a poor surface quality. In these samples,

sample 1 and 4 show the depressions(marked by the yellow dashed circles) on the top surface, and the surface quality was classified as poor due to these depressions (see section 4.2.1.1). It is worth noting that, even though roughness values of sample 2, 3, 5 are below 0.6, their surface qualities are still poor because the depressions exist on the other cross-sections. More specifically, sample 2, 3, and 5 all have the depressions which lead to the bad surface quality of these samples.

Theoretically, top surfaces of all two-layers structures should have a minimum waviness if the step over increment equals to two-thirds of the width of the bead, according to the research of Suryakumar et al [32]. An entirely flat surface can however not be achieved due to the nature of the welding process. In addition, a variation in roughness along the bead is based on the stability of the bead shape, i.e. the weld width. Also the measurements by a vernier calliper introduces an experimental error of approximately 0.1 mm in the determination of the bead width which slightly affects the step over increment. More specifically, the reason for the imperfect surface roughness is the error during measurement of the bead width (shown in Table 4.1), resulting in the error in the calculation of the optimum step over increment. The reasons for the error in the measurement of the width are a) the bead width is not uniform over the entire bead length, and at some locations of the bead could have larger or smaller widths. b) the widths of Table 4.1 were measured by the vernier calliper, and the distance between two edges of the bead is the width value. However, if this measured distance was not exactly on the cross-section which we wanted to measure, then there is a possibility of an error. Hence, it's difficult to get the exact correct width value of the beads for the calculation of the optimum step over increment to get an entirely flat top surface.

To sum up, samples 6-11, 13, 14 have better surface quality because the optimum step over increment has been set to two-thirds of the width, and the measured widths are relatively accurate. Among samples 6-11, 13, 14, sample 9 has the best surface quality. Moreover, Sample 12 has the worse surface quality even though the optimum step over increment has been set up to two-thirds of the width. This worse surface quality is caused by the bigger error of the measured width value, leading to a more inaccurate step over increment. Besides, sample 1 to 5 have the bad surface roughness due to the depressions formed on the top surfaces.

4.2.1.3. Geometry of structure

The side view images of samples 1 to 14 are listed in Table 4.6. Samples 1 to 5 are from the low heat input zone, while samples 6 to 8 are from the edge part of the medium heat input zone. According to Table 4.6, samples 1 to 8 have severe rising ends, which means the heights of two ends of the structure are much higher than that of the middle steady-state part of the structure, and the rising ends result in very non-uniform structures [55]. The reason for the rising ends is explained below. Samples 1 to 8 were deposited with lower heat input, which leads to a higher cooling rate. Besides, the arc existed for more time at the start and stop point due to the operating conditions corresponding to start and stop of the torch, so there is more molten

material at the start and stop point, and the molten material solidified very fast due to high cooling rates associated with low heat input [56]. Hence, samples 1 to 8 have higher height at the start and stop region compared to the middle region of the two-layer structures.

Moreover, samples 12 to 14 are from the high heat input zone, and sample 11 is from the edge part of the medium heat input zone. Table 4.6 shows that sample 11 to 14 have a higher tapered end. The tapered end has the feature that there is a significant slope on one end of the structure, which leads to an uneven structure [55]. The reason for the formation of the tapered end is that samples 11 to 14 were deposited with higher heat input, which resulted in a lower cooling rate and a large weld pool [57][58]. When the welding process came to the region close to the stop point, the arc was more stable and the wire received more heat to deposit on the substrate. The large weld pool was formed on the substrate and cooled down slowly due to the high heat input, which made the melted metal flow for a longer time and become a huge slope on the end of the structure. Besides, there is another reason for the height difference between the two ends of the structure. When the welding process started from the one end, the cooling rate was higher at the start point due to the cold substrate [3]. Hence, the structure is higher at the start point than the other end because the melted metal solidified faster with the cold substrate at the start point.

Sample 9 and 10 are both from the middle region of the medium heat input zone. According to Table 4.6, sample 9 and 10 have more uniform structure only with very slight rising ends and tapered end compared to the other samples. Moreover, among sample 9 and 10, the height of sample 9 is more uniform along the whole bead. Hence, the structure of sample 9 shows a more steady behaviour than sample 10.

To sum up, samples 1 to 8 have the acute rising ends, and samples 11 to 14 display the drastic tapered end. So when the multiple-layer structure is deposited with the process parameters of samples 1 to 8 and samples 11 to 14, uneven geometries will be formed and result in a tilted structure. With the process parameters of sample 9 and sample 10, the structures can be more uniform and steady due to the improvement in rising ends and tapered end. Furthermore, according to Table 4.6, using the process parameter of sample 9 is more ideal than that of sample 10 because sample 9 shows the most uniform structure.

Table 4.6: The side views of the 14 samples

No.	Side view
1	
2	
3	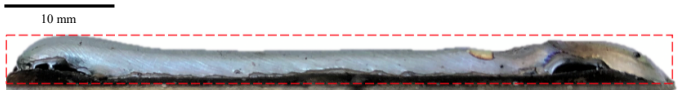
4	
5	
6	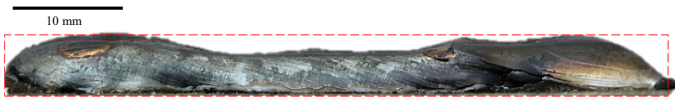
7	
8	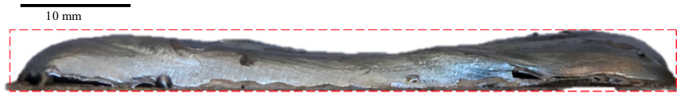
9	
10	
11	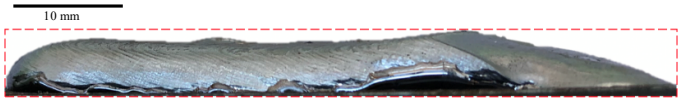
12	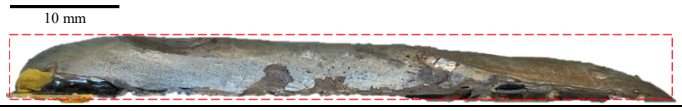
13	
14	

4.2.1.4. Summary

For achieving the high-quality multi-pass multi-layer structure, depression defects, surface roughness, and geometry are considered as the critical factors to evaluate the quality of the structure. As the ratio of the wire feed rate and the travel speed is equal to or less than 4.6, the depression defects are formed because the amount of feeding material is not enough to deposit the structure uniformly with the high travel speed. Besides, the process parameters of samples 6-11, 13, 14 resulted in better surface roughness, because the step over increments were set to two-thirds of the width, which is considered ideal. Sample 9 has the best surface roughness among these samples. In addition, the process parameter of sample 9 also result in a structure having uniform geometry because the appropriate heat input minimises the rising starts and tapered end effects.

To sum up, the welding condition of sample 9 with a wire feed rate 4.5 (m/min) and a travel speed 8 (mm/s) are the optimized parameters to be applied to deposit the multi-pass multi-layer structure with highest quality.

4.3. Functionally graded component

4.3.1. Macrostructure

The functionally graded rectangular block is shown in Figure 4.12. Figure 4.13 shows the stitched image of the transverse cross-section of the functionally graded component. This figure shows the different zones of the functionally graded component: a) High heat input zone I. b) Low heat input zone. c) High heat input zone II.

In Figure 4.13, the columnar grains can be observed. The formation of the columnar grains is explained as follows. In the weld metal, epitaxial growth dominates the grain structure of the area close to the fusion line. The epitaxial growth leads to nucleation of the columnar grains at the fusion line, and the grain growth towards the centreline of the weld pool, resulting in the coarse columnar grain structure. The direction of the growth is along the maximum temperature gradient, which is the direction from the heat-affected zone to the weld pool centre [35][59]. Besides, equiaxed grains along the fusion line also can be observed. Velocity of solidification (V) and temperature gradient (G) at the solidification front are solidification parameters and they can influence the solidification microstructure. When the value of G/V is small, the formation of equiaxed grains is facilitated [60].

Besides, in Figure 4.13, white lines can be observed in the low heat input zone. Figure 4.14 shows the measured distance between the white line and the fusion line. The average distance between these white lines and the corresponding fusion line is 539.1 µm, with the standard deviation of 14.3 µm. Hence, the white lines always keep nearly the same distance from the fusion lines. The mechanical and microstructural features of these white lines will be explored later.

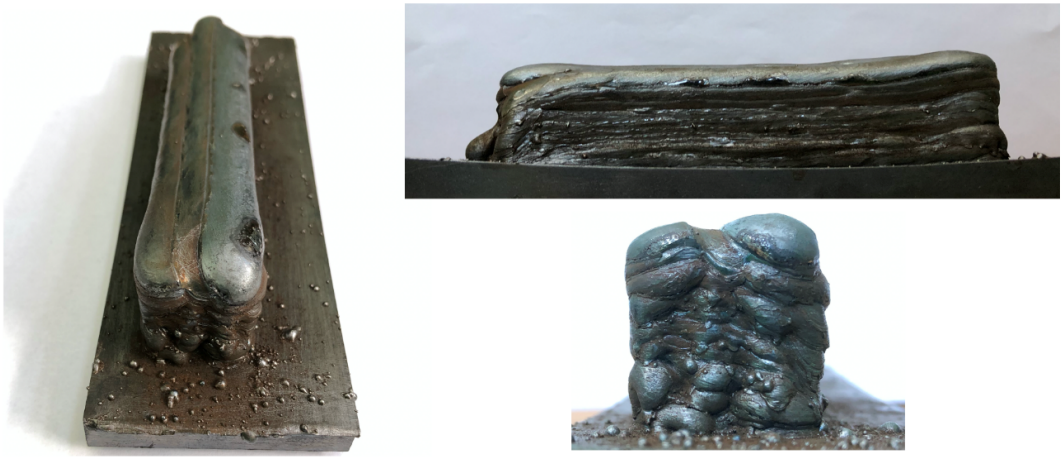

Figure 4.12: Functionally graded component

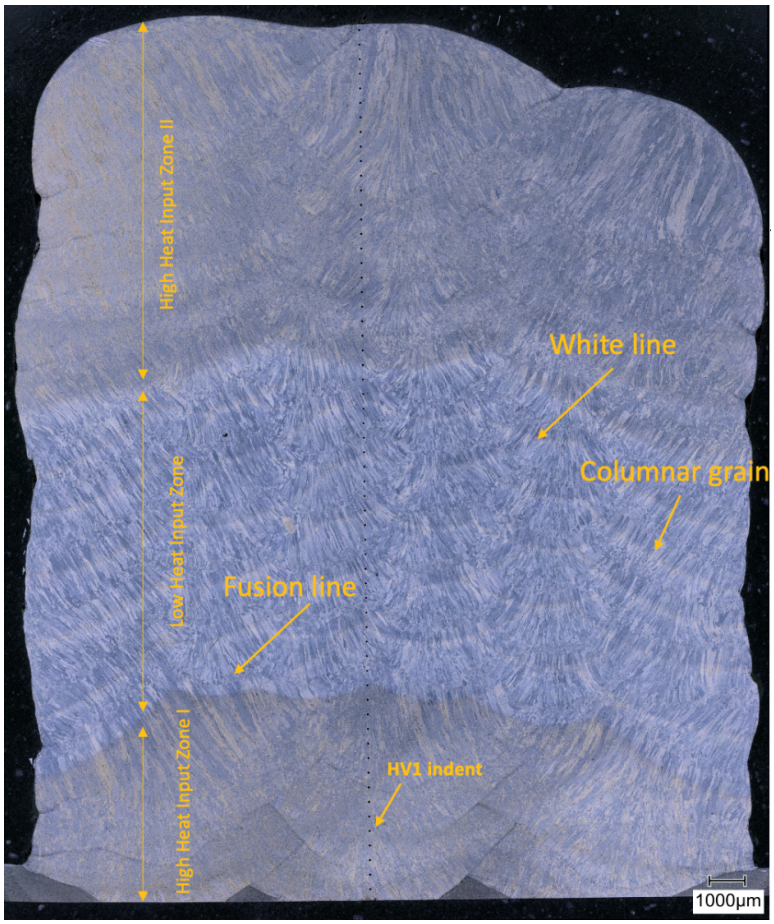

Figure 4.13: The stitched image of the transverse cross-section of the functionally graded component

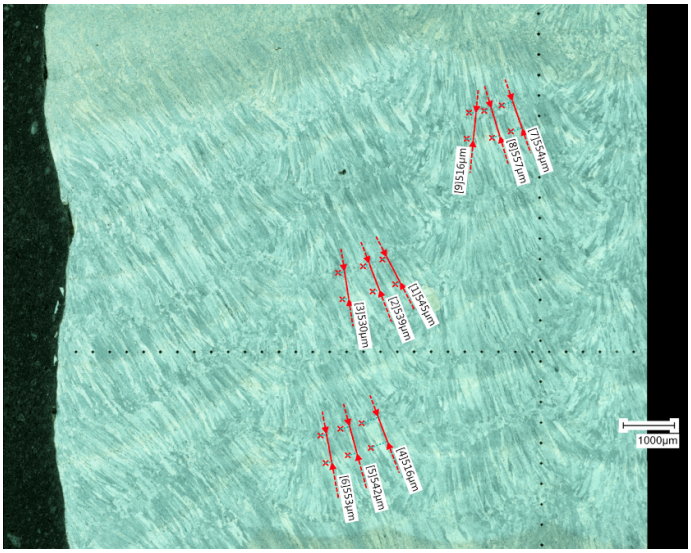

Figure 4.14: The distances between the white line and the fusion line

4.3.2. Microstructure

Figure 4.15 shows the microstructures in different regions of the functionally graded component. Figure 4.15(a) and Figure 4.15(c) display the microstructures of the high heat input zones I,II, which were both fabricated with the same process parameters, i.e. wire feeding rate of 6 m/min and travel speed of 8 mm/s. According to Figure 4.15(a) and Figure 4.15(c), microstructures of the high heat input zones I and II are dominated by the presence of ferrite and bainite. Figure 4.15(b) illustrates the microstructure of the low heat input zone, which was fabricated with a wire feeding rate of 6 m/min, but with a higher travel speed of 20 mm/s. In Figure 4.15(b), the microstructure of low heat input zone includes side plate ferrite, grain boundary ferrite, and martensite. The fraction of martensite phase is high in the low heat input zone. Moreover, according to Figure 4.15, it can be observed that the grain size of the low heat input zone is much smaller than the grain size of the high heat input zone I,II.

The reason for the formation of these varied microstructures in different zones of the functionally graded component is explained below. The different welding conditions of the high heat input zones I, II and the low heat input zone are the critical causes for the various microstructures in these zones. The higher heat input results in lower cooling rate, which results in softer microstructures, such as ferrite and bainite, and grains growth [61]. A lower heat input of the low heat input zone increases the cooling rate, which produces harder microstructure, such as martensite, accompanied by fine grains [23][61].

Martensite is harder than bainite and ferrite. Hence, according to Figure 4.15, it can be expected that the low heat input zone should have higher hardness and the high heat input zone should have the lower hardness. The relation between the heat input, hardness, and the microstructure in High heat input zone I,II, and Low heat input zone will be further investigated in section 4.3.3.

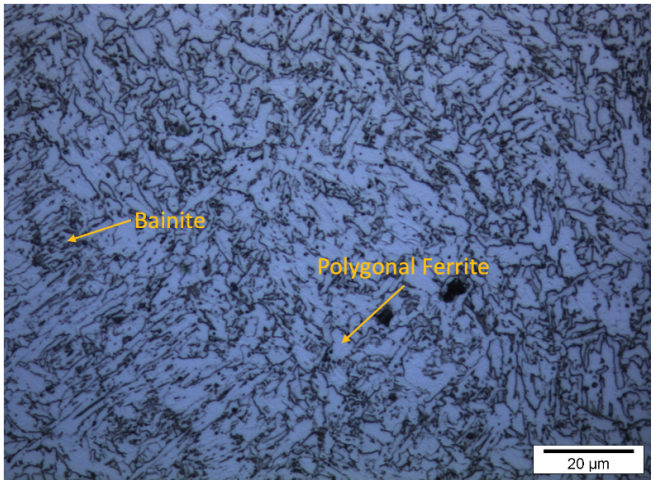

(a) High Heat Input Zone I (Bottom)

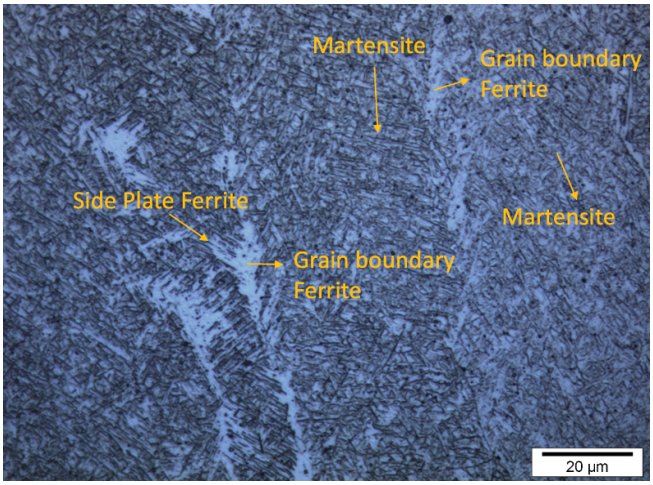

(b) Low Heat Input Zone

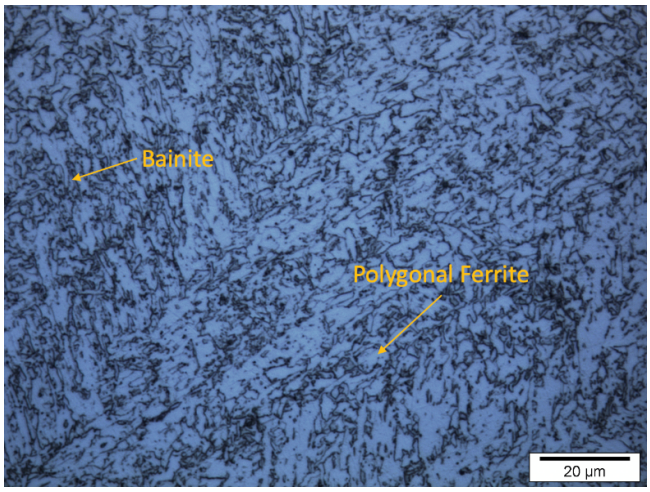

(c) High Heat Input Zone II (Top)

Figure 4.15: The optical microscopy images of the functionally graded component: (a) High Heat Input Zone I (Bottom); (b) Low Heat Input Zone; (c) High Heat Input Zone II (Top)

Figure 4.16(a) illustrates the SEM image of the white line region in the low heat input zone. In Figure 4.16(a), acicular ferrite and polygonal ferrite can be observed in the microstructure of this region. Besides, bainite also can be observed in Figure 4.16(a). Figure 4.16(b) shows the microstructure of the other regions in the bead of the low heat input zone, and it can be seen that martensite dominates in most of the region, which is the same as the microstructure observed in Figure 4.15(b). The microstructure in the white line region is dramatically different from other regions in the low heat input zone, and this inhomogeneous microstructure will affect the mechanical properties in the low heat input zone. Hence, the hardness of the white line region will be investigated further.

As martensite is harder than ferrite, it can be inferred that the hardness of the white line region will be smaller than the hardness of the other region in the low heat input zone.

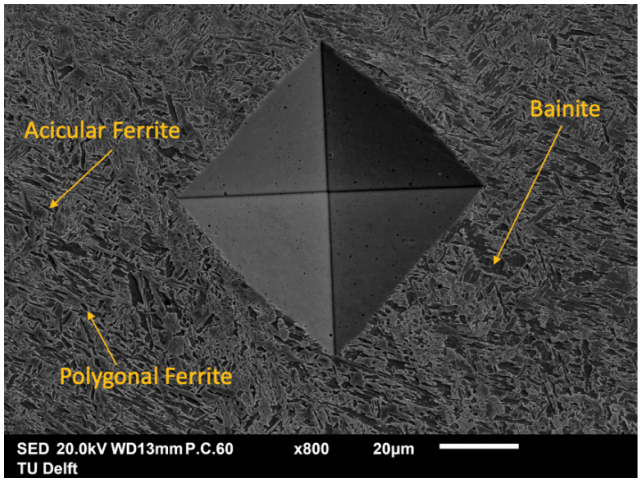

(a) White line region

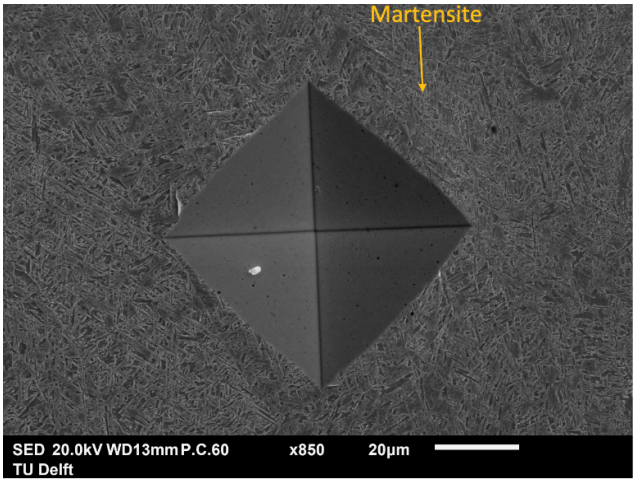

(b) Bead in the low heat input zone

Figure 4.16: SEM images of the low heat input zone: (a) white line region (b) bead region

4.3.3. Hardness measurement

Figure 4.17 demonstrates the hardness measurement of the functionally graded component, which shows the hardness value from the bottom layer to the top layer in the centre of the built sample as shown in Figure 4.13. The load used for the indentation was 1 kg to obtain a better-averaged hardness. According to Figure 4.17, both high heat input zones have similar hardness value, which is around 250 HV. The low heat input zone has a higher hardness value, which varies between about 280 to about 350 HV. The hardness value of the low heat input zone is larger than that of high heat input zone, which is in agreement with the prediction according to the characterization of microstructures in section 4.3.2. The reason for the higher hardness in low heat input region is the faster welding speed, the lower interlayer temperature of 50°C, and the lower interbead temperature of 50°C lead to the higher cooling rates, resulting in the higher fraction of martensite. On the contrary, a higher heat input and the interlayer temperature of 100°C used in the high heat input zone give rise to a lower cooling rate, leading to the higher fraction of ferrite and a lower fraction of martensite.

Moreover, it is worth noting that the hardness value oscillates in the low heat input zone, ranging from 280 to 350 HV. According to Figure 4.17 and the corresponding indent distribution in Figure 4.13, when the indents are closer to and on the white lines, the hardness values are lower.

Another set of hardness measurement was performed with a load of 200 g to evaluate the hardness across a white line. Figure 4.18 shows the small HV0.2 indents, across the white line with its initial and end points made within the bead region. According to Figure 4.19, the hardness drops from 350 HV to 280 HV as the measured point is on the white line. Hence, compared to the other areas in the low heat input zone, the white line region is softer. The reduction in hardness at the white line region agrees with the findings from microscopic observations (Figure 4.16(a)), which indicates a large amount of ferrite.

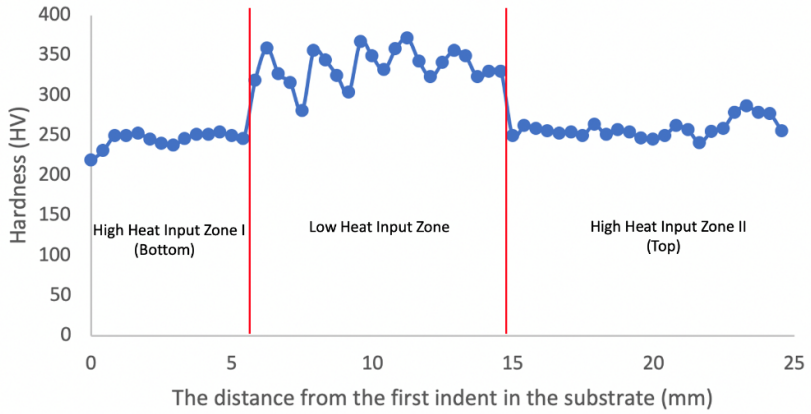

Figure 4.17: Hardness measurement for the functionally graded component

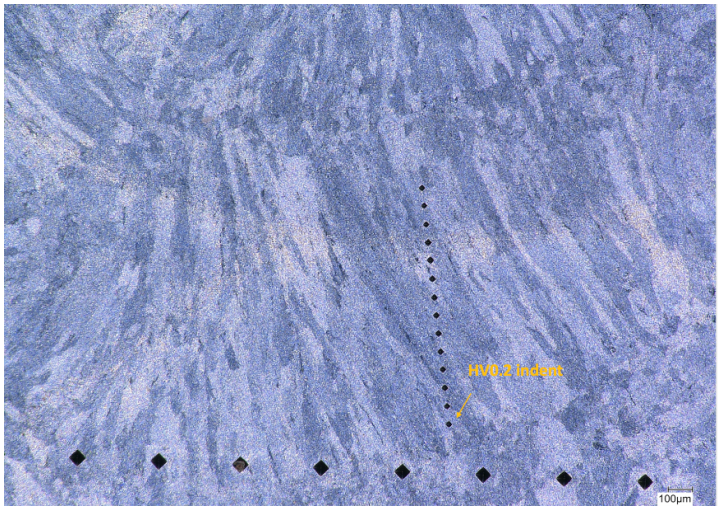

Figure 4.18: the small indents (HV 0.2) across the white line

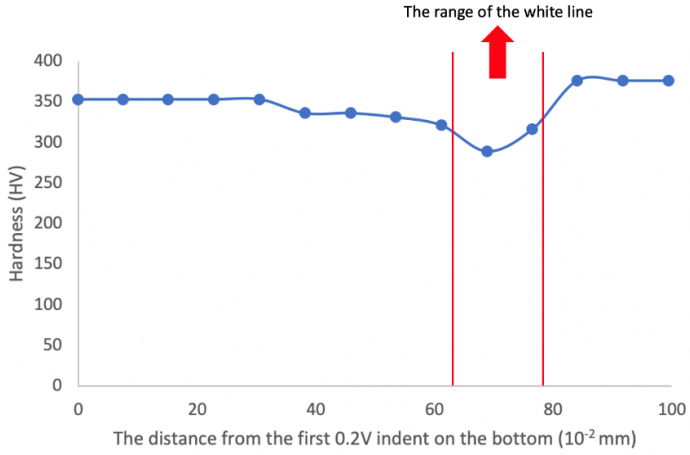

Figure 4.19: Hardness measurement for white line (HV 0.2)

4.3.4. White line region in low heat input zone

According to the findings about white line, white lines exist in some specific regions and they have a large amount of ferrite as well as the lower hardness. It is worth to explore the reason of the existence of these special white lines which lead to inhomogeneous microstructural features and mechanical properties in the low heat input zone. The possible mechanism of the formation of these white lines is explained as follows. In Figure 4.14, the distance of the white line and the fusion line always keeps almost the same. Thus, it can be assumed that the white line underwent the same thermal history in the heat-affected zone when the subsequent weld pass was applied on the deposited structure. When the subsequent welding was performed, the temperature could increase to the intercritical range ($\alpha+\gamma$ region between A_{C1} and A_{C3}) at the location of the white line. The nucleation of ferrite possibly occurred during the process of temperature heating to intercritical range, and the ferrite grains could grow when the temperature achieved the intercritical range ($\alpha+\gamma$ region). Besides, during the intercritical range ($\alpha+\gamma$ region), austenite could also form. However, when the temperature cooled down, the cooling rate could be not fast enough to realise the transformation of austenite to martensite, because the cooling rate drops significantly with the distance away from the fusion line [23]. Hence, the formed austenite could finally transform to ferrite after cooling down.

Therefore, a large amount of ferrite forms at the location of white line possibly because it underwent the thermal history of heating up to the intercritical range. Besides, the new-formed ferrite replaces martensite, thereby reducing the hardness, as shown in Figure 4.17 and Figure 4.19.

In addition, after the new-formed ferrite formed, the subsequent welding pass could increase the temperature to approximately 500°C to 700°C resulting in the recrystallization and grain growth of ferrite, which decreases the hardness further [62]. The reduction of the stored strain energy in materials is the driving force for recrystallization. Recrystallization proceeds by heating, thereby replacing strained grains by new grains with a low defect (dislocation) concentration [62][63]. Besides, because the interaction between dislocations can obstruct the movement of dislocations to make the material harder, i.e. strain hardening. Hence, the decrease in dislocation density, caused by the defect-free new grains formed during recrystallization, will lead to a lower hardness [64]. Moreover, grain growth also could occur, and the driving force of the grain growth is the reduction of grain boundary energy, which can be achieved by decreasing the grain boundary area. For decreasing grain boundary area, grains merge into the grain with a bigger grain size by the movement of grain boundaries [63][65]. The increase of the grain size during grain growth results in the decrease of hardness according to the Hall-Petch relation [66].

To sum up, the hardness of the high heat input zone I,II is lower than that of the low heat input zone because the high heat input zone I,II mainly contain ferrite and bainite, whereas the low heat input zone mainly contains of martensite. The difference in microstructure between the zones is mainly due to the heat input. A high heat input leads to the lower cooling rate, while in the low heat input zone higher cooling rates are achieved. In addition, a more inhomogeneous microstructure is observed in the low heat input zone due

to the relatively lower hardness in the white line region. The possible reason for the lower hardness in the white line region is the large amount of ferrite formed and replaced the martensite, where the temperature achieved the intercritical range, and recrystallization and grain growth of ferrite occurred when it was heated up to about 500°C to 700°C during the subsequent weld pass.

4.4. Crossing structures

4.4.1. Macrostructure

Figure 4.20 shows the images of the crossing structure fabricated with the interlayer temperature of 100°C. The measured heights are illustrated in Figure 4.20(b): the height at the centre is 33.5 mm, and the heights of the side walls are 32.5mm, 30.9 mm, 32.6 mm, 30.1 mm. According to these results, a peak develops at the centre of the crossing structure. Peak development usually can be observed in the crossing structure due to the overlapping beads of the WAAM wall [10], as mentioned in Chapter 2. Figure 4.21 shows the images of the crossing structure fabricated with the interlayer time of 90 sec. The measured heights are shown in Figure 4.21(b): the height at the centre is 34.3 mm, whereas the heights of the side walls are 32.7mm, 31.5 mm, 32.7 mm, 31.5 mm. Because the same deposition pattern and process parameters were applied for these two crossing structures, the height of the crossing structures is similar. Also in this structure, a peak exists at the centre.

(a) Side view image of the crossing structure

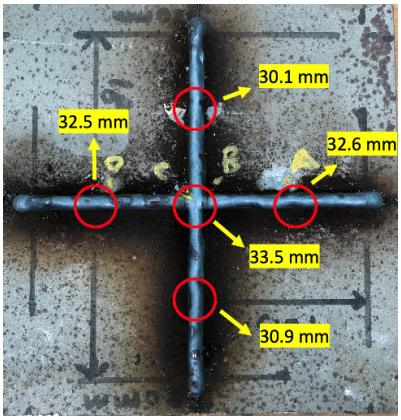

(b) Top view image of the crossing structure

Figure 4.20: The crossing structure fabricated with interlayer temperature of 100°C

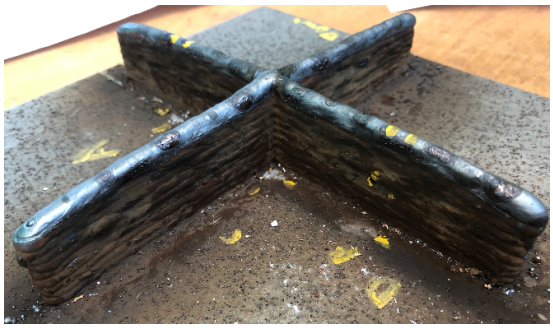

(a) Side view image of the crossing structure

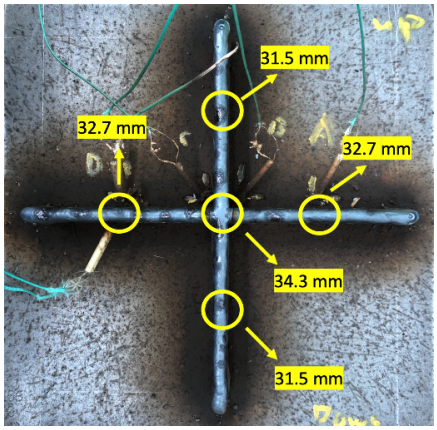

(b) Top view image of the crossing structure

Figure 4.21: The crossing structure fabricated with interlayer time of 90 sec

The crossing structures were divided into different zones and cross sectioned samples were cut from all these zones. Figure 4.22 shows the locations of different zones: side zone I, centre zone and side zone II (adjacent to the centre zone). The cross sectioned samples were cut from the centre zone and the side zone I of the crossing structure with the interlayer temperature of 100°C. Figure 4.23(a) and Figure 4.23(b) respectively display the stitched images of the cross sectioned samples. Thermocouples were attached at the centre zone during the deposition of the crossing structure with the interlayer temperature of 100°C (shown in Figure 3.8) .

The cross sectioned samples were also cut for the crossing structure with the interlayer time of 90 sec. Figure 4.24(a), Figure 4.24(b), and Figure 4.24(c) respectively illustrate these stitched images of these cross sections. Thermocouples were attached to side zone I during the deposition of the crossing structure with the interlayer time of 90 sec (shown in Figure 3.9). The location of thermocouples of the crossing structure with the interlayer time of 90 sec is different from that of the crossing structure with the interlayer temperature of 100°C, because it was found that it's difficult to attach thermocouples to the exact centre zone accurately during the process of the deposition of the crossing structure. Hence, by attaching the thermocouples to the side wall, the thermal cycles of the desired location can be acquired accurately, and the accurate thermal cycles can be used to validate the simulation. Besides, by changing the location of thermocouples, both the thermal cycles at centre zone and side zone can be understood.

Fusion lines, i.e. the boundary between the fusion zone and the heat-affected zone, can be seen in Figure 4.23 and Figure 4.24 clearly. Besides, columnar grains are observed in the fusion zone of the beads in these figures. The columnar grains nucleate at the fusion line and grow along the direction with the maximum temperature gradient [35].

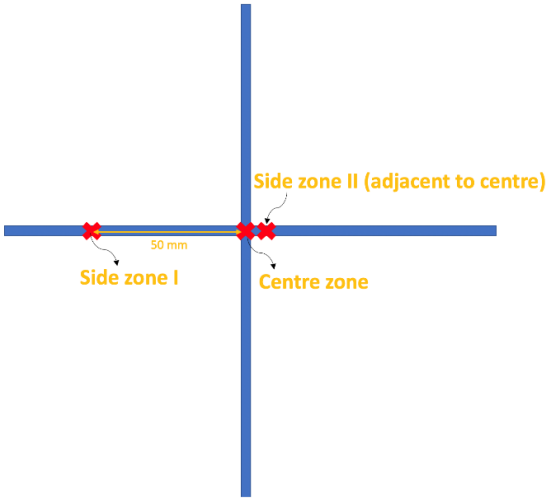

Figure 4.22: Different zones in the crossing structure (Top view)

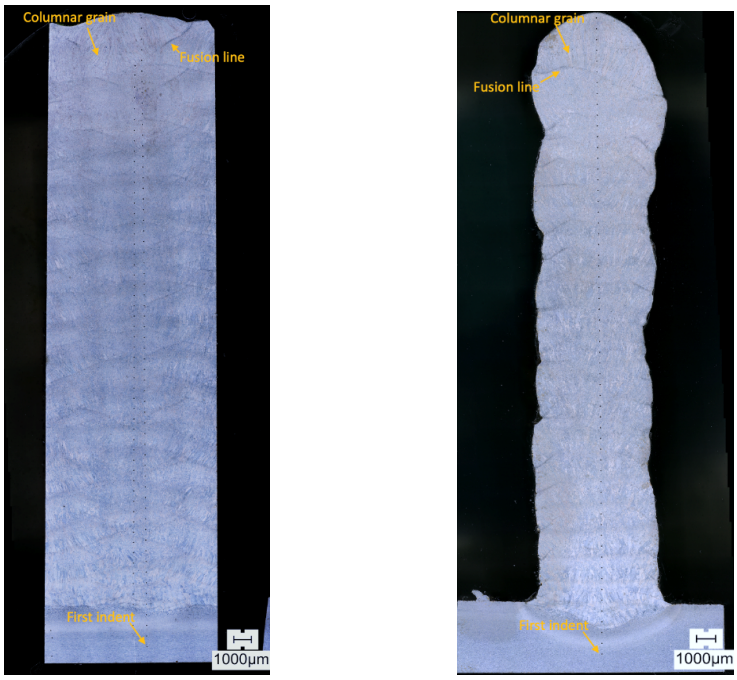

(a) Centre zone (b) Side zone I

Figure 4.23: The cross sectioned samples from the crossing structure fabricated with the interlayer temperature of 100°C

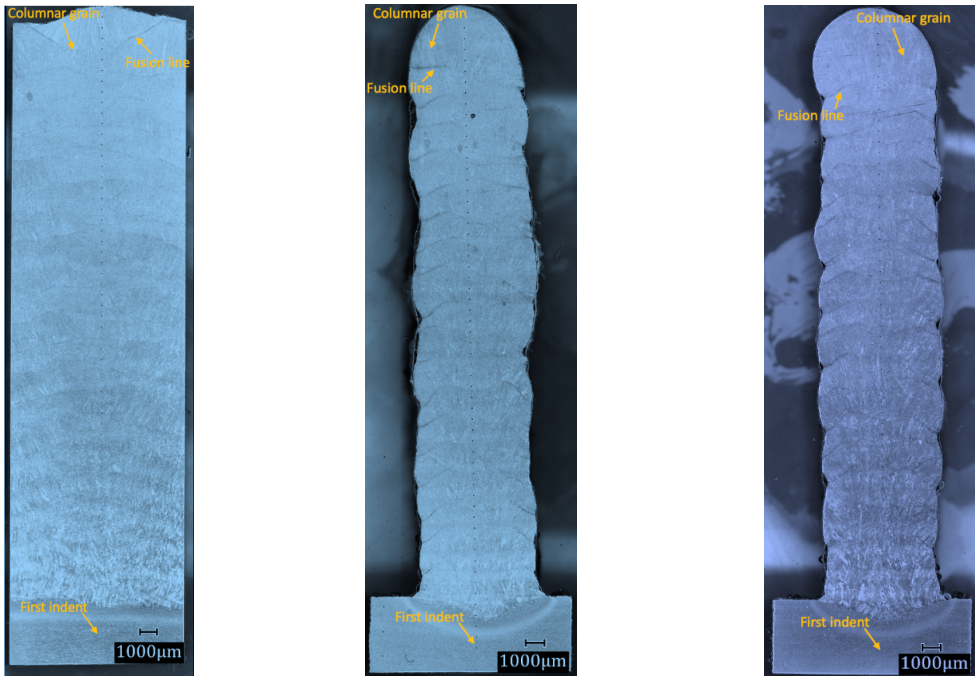

(a) Centre zone (b) Side zone I (c) Side zone II (adjacent to centre)

Figure 4.24: The cross sectioned samples from the crossing structure fabricated with the interlayer time of 90 sec

4.4.2. Thermal history

4.4.2.1. Thermal history of crossing structure with interlayer temperature of 100°C

Figure 4.25 indicates the location of tracking points A to G. Figure 4.26 shows the thermal histories of tracking point A, B, C, D on the substrate. Tracking point B, C shows there are two temperature peaks produced during the deposition of each layer, but tracking point A, D illustrate only one temperature peak is involved in depositing each layer. The reason for this difference at tracking point B and C is that these points are located close to the centre of the crossing structure. They experience a temperature cycle during the deposition of the two passes in each layer. Tracking point A and D, located at the side wall, detected the heat of only one pass during the deposition of each layer.

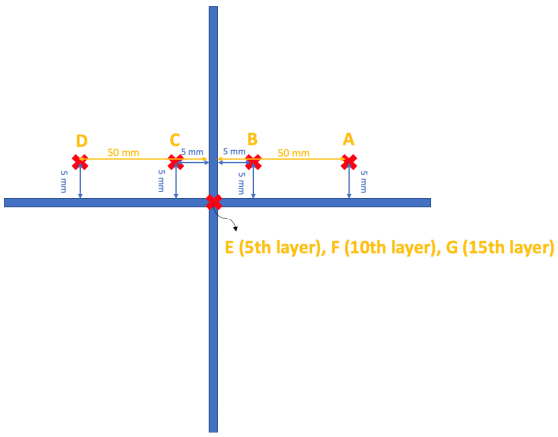

Figure 4.25: Locations of the tracking points (Top view)

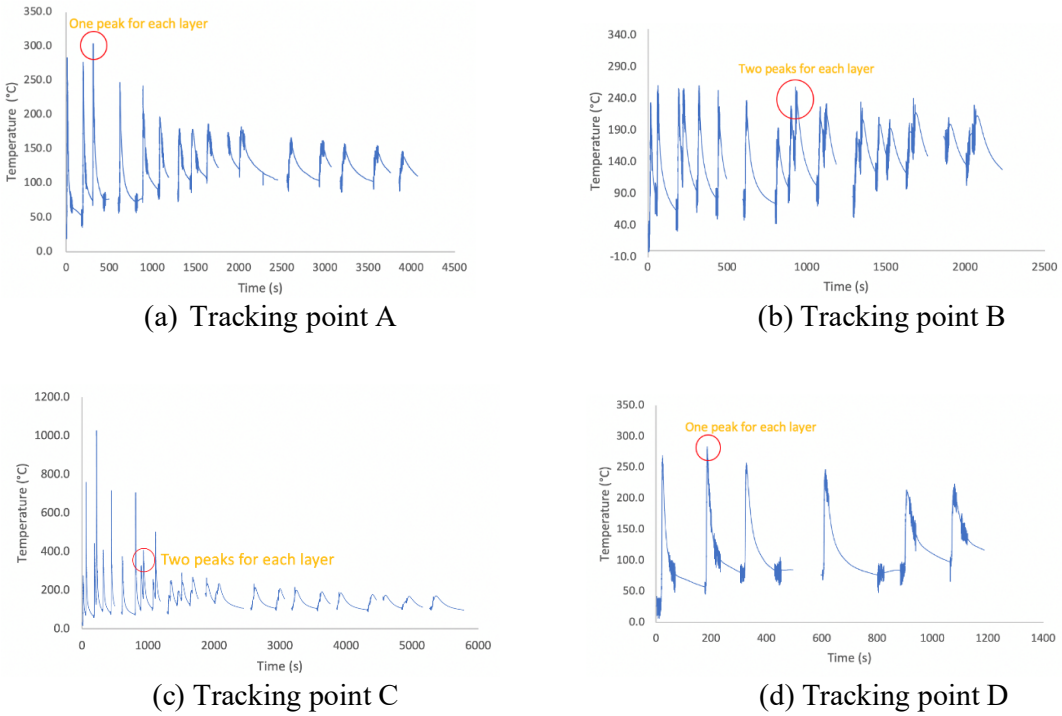

(a) Tracking point A

(b) Tracking point B

(c) Tracking point C

(d) Tracking point D

Figure 4.26: Thermal cycles of tracking point A, B, C, D on the substrate

In Figure 4.26, the thermal cycles of tracking points A to D attached to the substrate show that the peak temperature tends to decrease with time. The tendency of the peak temperature is because the temperature decreases with the distance away from the heat source. Hence, when the crossing structure was being built up, the heat source moved away from the substrate, leading to the decreasing peak temperature on the substrate during the process of the deposition [23][35]. However, in Figure 4.26, some temperature peaks do not always drop with time, and tracking point C even shows some temperature peaks above 600 °C, which are very different from the thermal cycles recorded in other tracking points. In addition to the above error, the noise in the signals can also be observed for all tracking points. The possible reasons for these errors in the temperature measurements are: (a) The error in the measured value and the noise could be caused by the interference of the thermal radiation from the arc during the welding process. (b) inhomogeneity of electrodes of thermocouples, caused by high temperature, could lead to 5 to 10 °C errors in the measurement [67][68][69]. (c) the connection between thermocouple and the substrate could be weak, leading to the error in the measurement.

Tracking point C records all the thermal cycles during the whole process of manufacturing 20 layers structure, see Figure 4.26(c). The total time for depositing the crossing structure with a constant interlayer temperature is over 5000 seconds.

Figure 4.27 shows the thermal cycles of the tracking point E, F, G at the centre of the crossing structure. In these figures, all thermal cycles show the tendency that the peak temperature decrease with the time because the heat source position was further away from the tracking point during the building up of the crossing structure. The cooling rates between 800°C to 500°C were calculated as it affects the microstructure of the steel [16], as mentioned in Chapter 2. It can be observed that the cooling rates decrease with time.

According to Figure 4.27, the highest cooling rate occurs in Tracking point E (in the lower layer). This is because the cold substrate strengthened the capacity for faster heat dissipation in the lower layers. The cooling rates are lower in the higher layers shown in Figure 4.27(b) and Figure 4.27(c). This is because the thermal accumulation becomes more severe during the entire deposition process [3].

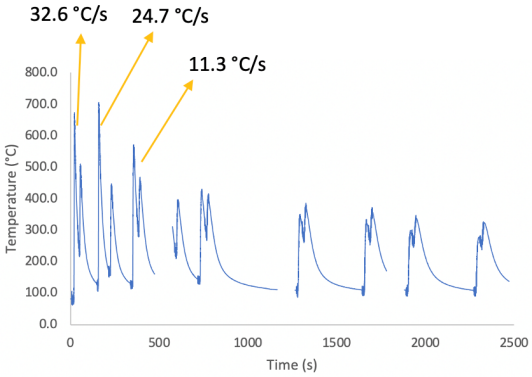

(a) Tracking point E (on 5th layer)

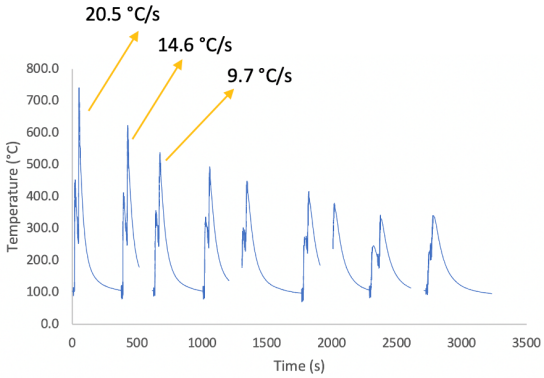

(b) Tracking point F (on 10th layer)

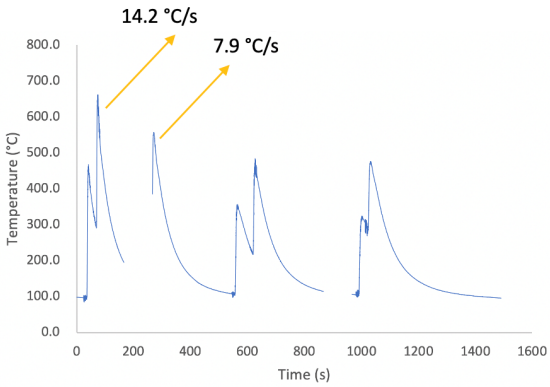

(c) Tracking point G (on 15th layer)

Figure 4.27: Thermal cycles of tracking point E, F, G at the centre

4.4.2.2. Thermal history of crossing structure with interlayer time of 90 sec

Figure 4.28 indicates the location of the tracking points A' to G'. Figure 4.29 shows the thermal histories of tracking points A', B', C', D' attached to the substrate. In Figure 4.29, the peak temperatures of each tracking point increase slightly and then stabilises, which is different from the tendency of the decreasing peak temperature shown in Figure 4.26. This is because the shortening of the time between each layer leads to the more severe thermal accumulation in the substrate. More specifically, the heat in the substrate has less time to diffuse when an interlayer time of 90 sec is maintained. More heat accumulates in the substrate compared to the crossing structure fabricated with interlayer temperature 100°C. Tracking point C' records all the thermal cycles during the whole process of manufacturing the 20 layers crossing structure, see Figure 4.29(c). From this measurement, it can be extracted that the total build time is about 3000 seconds, which is much less than the total time for depositing the crossing structure fabricated with the interlayer temperature of 100°C (shown in Figure 4.26(c)).

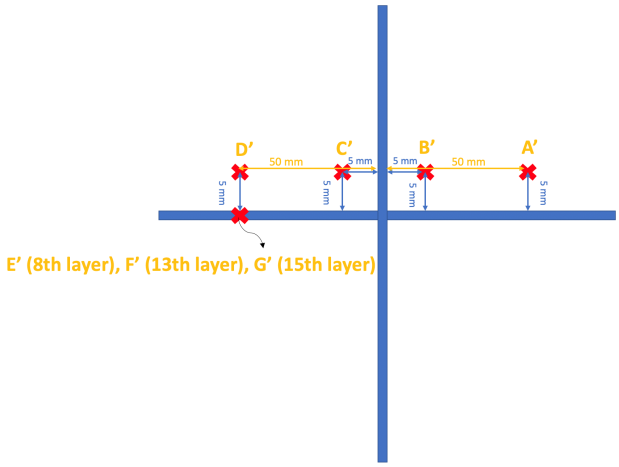

Figure 4.28: Locations of the tracking points (Top view)

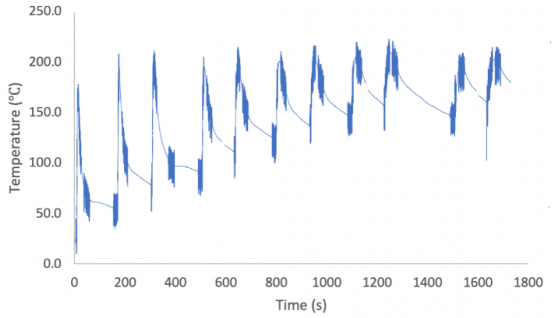

(a) Tracking point A'

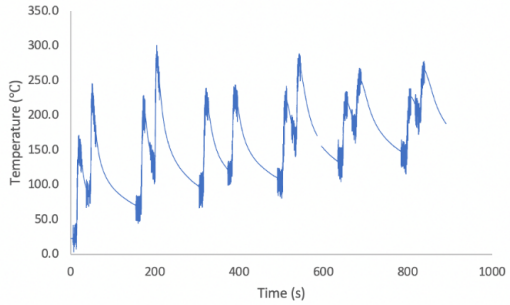

(b) Tracking point B'

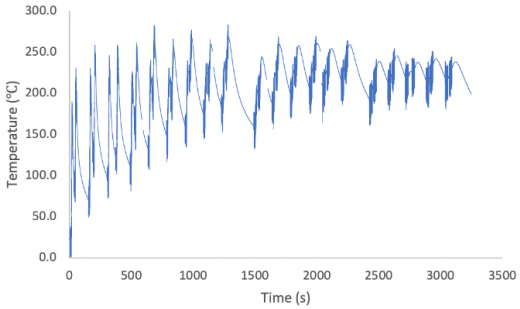

(c) Tracking pint C'

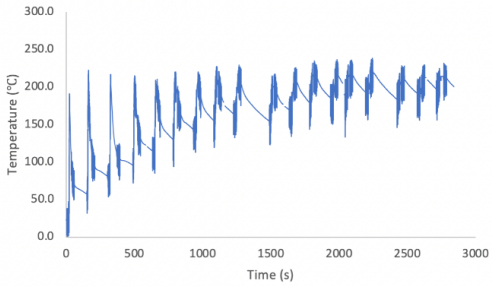

(d) Tracking pint D'

Figure 4.29: Thermal cycles of tracking point A', B', C', D' on the substrate

All methodology and the result of the thermal simulation in this thesis have been designed and provided by Rutger Schreurs. Figure 4.30 shows the thermal cycles obtained from the simulations and experimentally by thermocouples at tracking point E', F', G' at the side wall. The thermal history of the simulation fits well with the thermal history of the thermocouple measurements. Therefore, the simulation can accurately predict the thermal history of the side wall of the crossing structure, which was fabricated with the interlayer time of 90 sec. However, some small differences between the simulation and the thermocouple still can be observed. According to Figure 4.30, the values of cooling rates and the peak temperatures in each thermal cycle are slightly different between the simulation and the thermocouple. For example, for the third thermal cycle in

Figure 4.30(a), the peak temperature (1372 °C) and the cooling rate (23.9 °C/s) of the simulation are slightly higher than the peak temperature (1355 °C) and the cooling rate (19.8 °C/s) obtained by the thermocouple. The differences can be explained. First, the setup of simulation did not include latent heat for phase transformation. Latent heat is the releasing or absorbing of the heat during the phase transformation with a constant temperature [70][71]. Hence, avoiding latent heat could result in incorrect temperature predictions in the high temperature regime. Moreover, the thermal properties of S690QL1 HSLA were used for this simulation. However, LNM MoNiVa wire was used in the experiment. Hence, there is a difference between the thermal properties of S690QL1 HSLA and LNM MoNiVa, leading to the different thermal histories. Besides, as mentioned previously, inhomogeneity of electrodes of thermocouples can result in the error of 5 to 10 °C, which also could be one of the possible reasons for the difference between the thermocouple and the simulation [67][68][69].

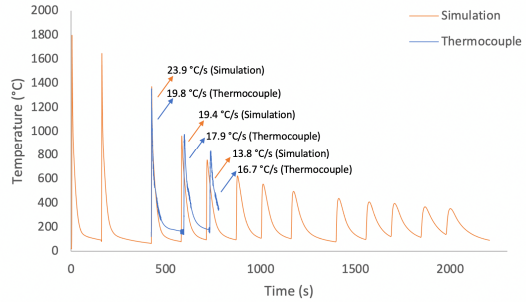

(a) Tracking point E' (on 8th layer)

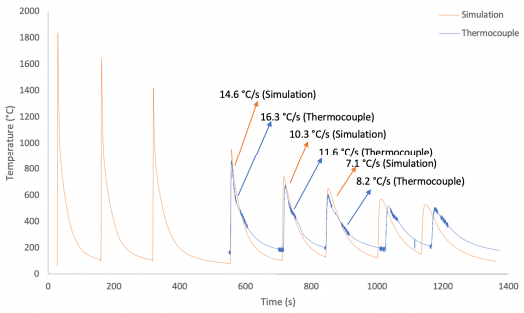

(b) Tracking point F' (on 13th layer)

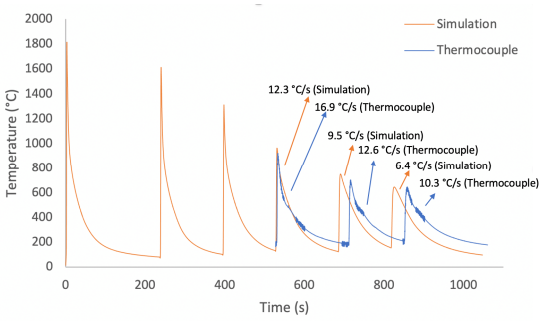

(c) Tracking point G'(on 15th layer)

Figure 4.30: Simulation and measured thermal cycles at tracking point E', F', G' at the side wall

Figure 4.31 shows the simulated thermal cycles undergone at the side wall (the location is 50 mm from the centre, like the location of tracking point E', F', G' but at a different height) and the centre in different layers of the crossing structure with the interlayer time of 90 sec. Layer 1, layer 10, and layer 20 are used to represent the bottom, middle, and top region of the crossing structure.

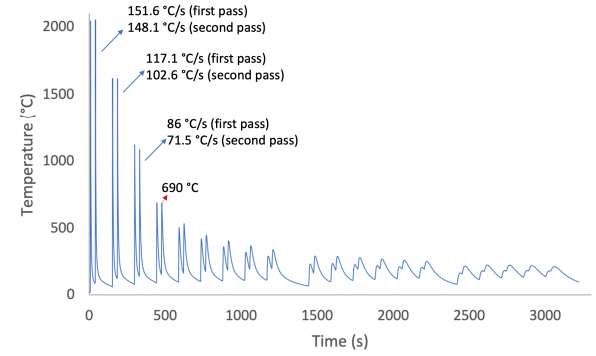

(a) 1st Layer at the centre

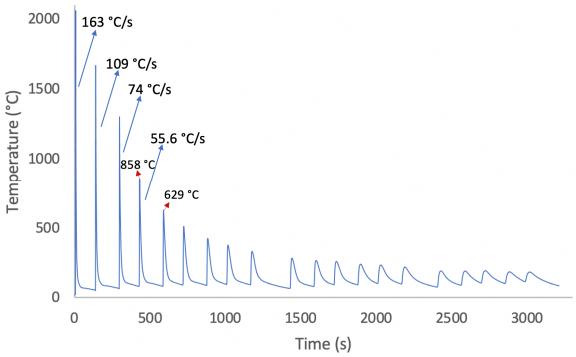

(d) 1st Layer at the side wall

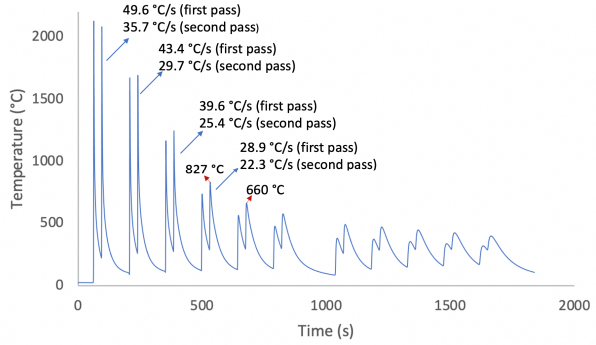

(b) 10th Layer at the centre

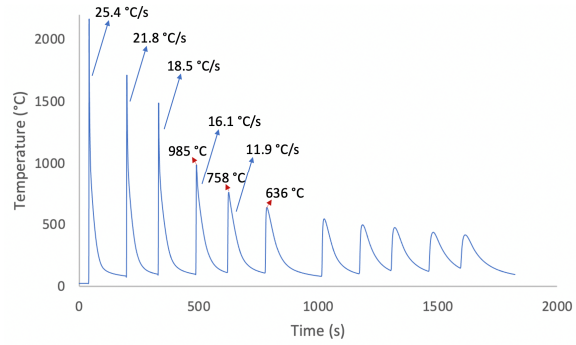

(e) 10th Layer at the side wall

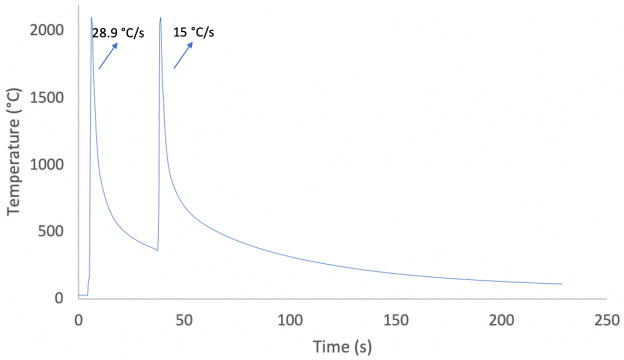

(c) 20th Layer at the centre

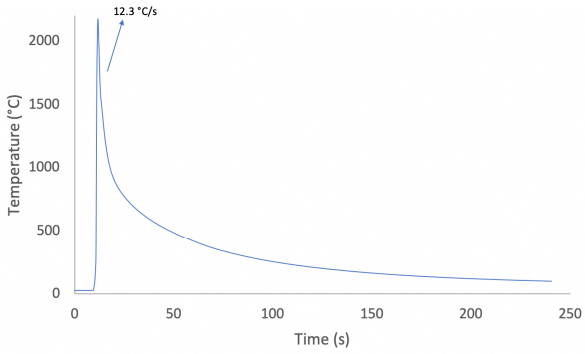

(f) 20th Layer at the side wall

Figure 4.31: The thermal cycles of the simulation at the side wall and the centre of different layers

According to Figure 4.31, the peak temperature always tends to decrease with time. The decreasing peak temperature is because during the process of depositing the crossing structure, the heat source became farther away from the previously deposited layer. It can be observed that the cooling rate also always decreases with time [23][35].

According to both Figure 4.31(a)-(c) and Figure 4.31(d)-(f), the cooling rate dramatically decrease from the 1st layer to 20th layer. For example, in Figure 4.31(d) and Figure 4.31(f), the first thermal cycle of 1st Layer at the side wall has the cooling rate of 163 °C/s, and the cooling rate of the first thermal cycle of 20th layer drops to 12.3 °C/s. The significant difference in cooling rate is because the cold substrate increased the heat dissipation of bottom layers and hence the cooling rate in bottom layers can become above 150 °C/s. Besides,

the impact of thermal accumulation became more severe when the higher layers were built. Hence, middle layers have medium cooling rate due to the increasing heat accumulation, and top layers have the lowest cooling rate due to the highest heat accumulation in the crossings [3].

The discussions about the cooling rates of the middle layers, the bottom layers, and the top layers are shown in the following three paragraphs, and the microstructure can be predicted with the aid of the continuous cooling transformation (CCT) diagram of low-carbon low-alloy steel in Figure 4.32, which has a similar composition of the feedstock material used in this research. Moreover, for the feedstock material used for corssing structures, A_{C1} is 731 °C and A_{C3} is 863 °C. Besides, it is worth noting that for depositing each layer, there are two passes included in one thermal cycle for centre zone.

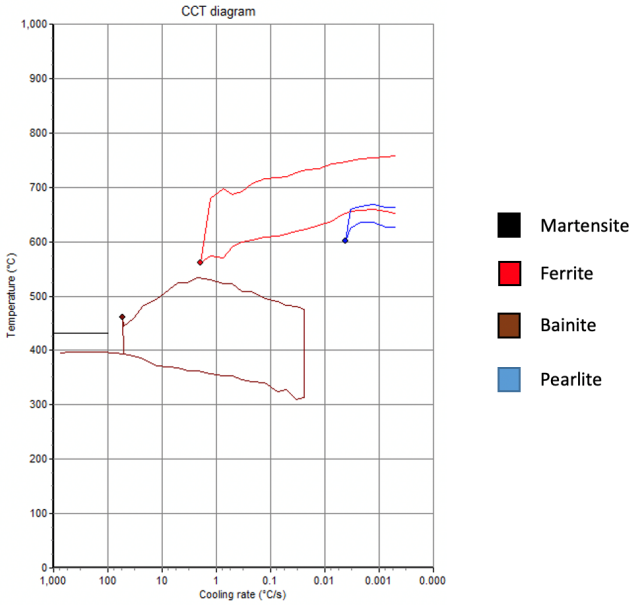

Figure 4.32: Continuous cooling transformation (CCT) diagram of the low-carbon low-alloy steel

(a) In the middle layers, the cooling rate of the first pass of the thermal cycle at the centre (Figure 4.31(b)) is always much higher than the cooling rate of the same thermal cycle at the side wall (Figure 4.31(e)). The higher cooling rate of the first pass at the centre is because the heat can diffuse from the centre to four connected walls. Hence, compared to the side wall, the heat produced at the centre had more area to transfer and the higher cooling rate of the first pass in each thermal cycle was achieved. However, the deposited material at the centre underwent second pass in each thermal cycle of depositing each layer. Due to the thermal accumulation caused by the first pass in each thermal cycle, the cooling rate of the second pass in the same thermal cycle decreased a lot, and second pass has the almost same peak temperature as that of the first pass [3][72]. This situation can be observed at the centre of every layer. Therefore, by comparing Figure 4.31(b) and Figure 4.31(e), it can be observed that the difference of cooling rate between centre and side wall becomes small in each thermal cycle during depositing each layer, because the cooling rate of the second pass at the centre drops a lot. Besides, according to the CCT diagram in Figure 4.32 and the cooling rates in

Figure 4.31(b) and Figure 4.31(e), it can be inferred that bainite could form in the microstructure in the middle layers of the crossing structure.

(b) According to Figure 4.31(a) and Figure 4.31(d), in the bottom layers, the cooling rate of the same thermal cycle at the centre and at the side wall are close. The reason is that for the bottom layers, the cooling rate at side wall and centre were both dominated by the effect of the cold substrate, which contributed to a very high heat dissipation and made the cooling rates at the side wall and the centre in the bottom layers quite close and high [3][35]. Moreover, based on the CCT diagram in Figure 4.32 and the cooling rates in Figure 4.31(a) and Figure 4.31(d), it can be known that both martensite and bainite could be included in the microstructure of the bottom layers of the crossing structure.

(c) According to Figure 4.31(c) and Figure 4.31(f), in the top layers, cooling rates of the same thermal cycle at the centre and the side wall are close and very low due to the highest accumulation in the top region as well as the extra thermal accumulation at the centre caused by first pass in each thermal cycle [3]. Besides, according to the CCT diagram in Figure 4.32 and the cooling rates in Figure 4.31(c) and Figure 4.31(f), it can be realized that bainite could form in the microstructure of the top layers of the crossing structure.

To sum up, for both the centre and the side wall, the cooling rate tends to decrease from the 1st layer to 20th layer due to the impact of the cold substrate and the thermal accumulation during the deposition process. For the bottom region (bottom layers), the cooling rates of the centre and the side wall are both very high and close because of the high impact of the cold substrate. For the middle region (middle layers), compared to the side wall, the cooling rate is always slightly higher at the centre because the heat at the centre has more area to diffuse. For the top region (top layers), the cooling rates of the centre and the side wall are both very low and close due to the greatest extent of thermal accumulation.

4.4.3. Microstructure

The microstructures of the different regions along the building direction of the crossing structures with the interlayer time of 90 sec and the interlayer temperature of 100 °C are shown in Figure 4.33 and Figure 4.34. In each of the bottom, the middle, and the top regions, the crossing structure can be divided into the centre zone, the side zone I, and the side zone II (adjacent to the centre zone), and the locations of these zones have been indicated in Figure 4.22. It is worth noting that even though the side zone II (adjacent to the centre zone) was additionally cut into the samples for characterizing its microstructure, the microstructure in the side zone II is actually very similar to the microstructure in centre zone, because the side zone II and the centre zone are extremely close, which makes them undergo the similar thermal histories. Hence, in this chapter, the difference between the centre zone and the side zone I are mainly discussed below, because the centre zone actually can represent the side zone II (adjacent to the centre zone) due to the similar thermal histories and microstructures.

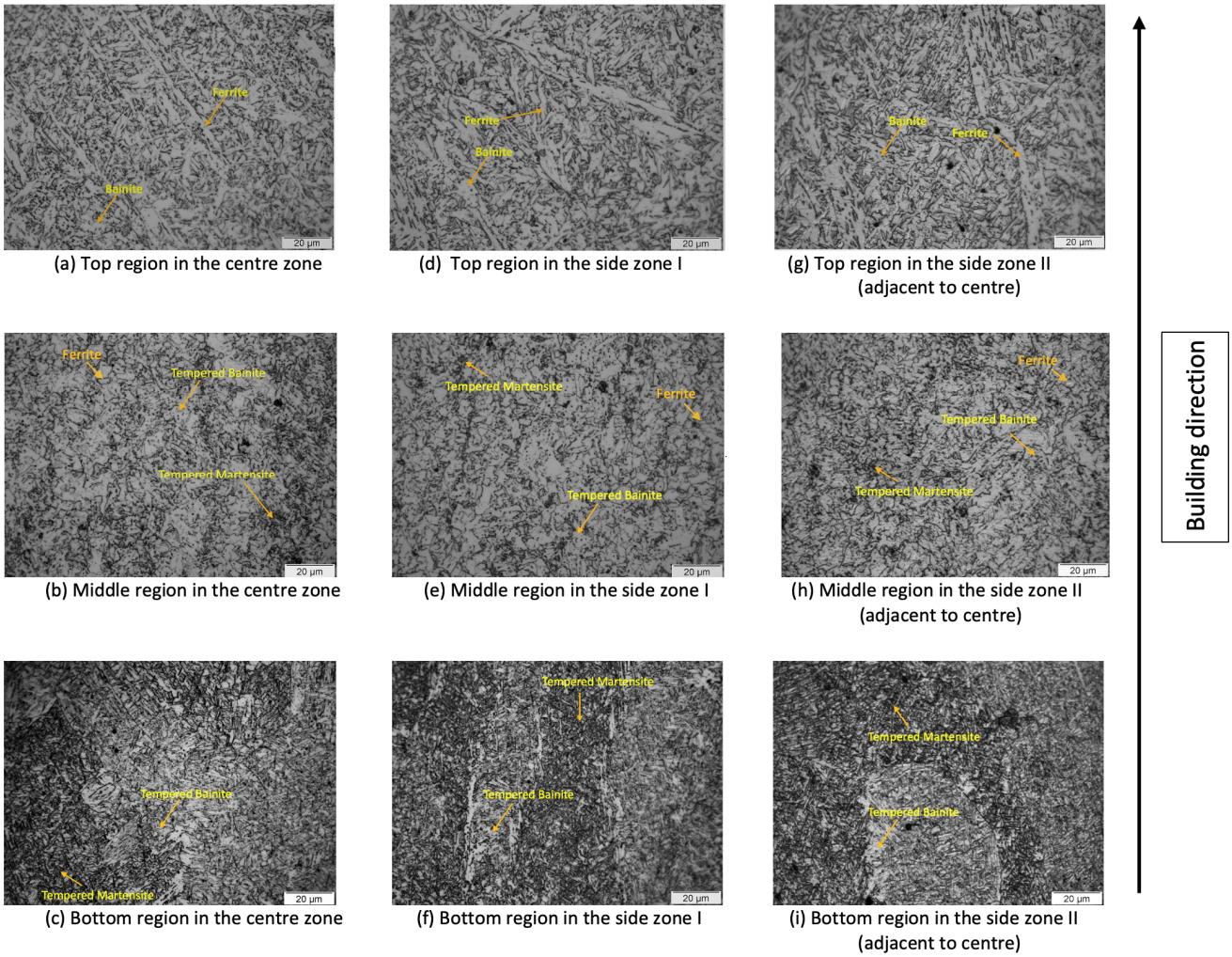

Figure 4.33: The microstructure of the different regions along the building direction of the crossing structure with the interlayer time of 90 sec

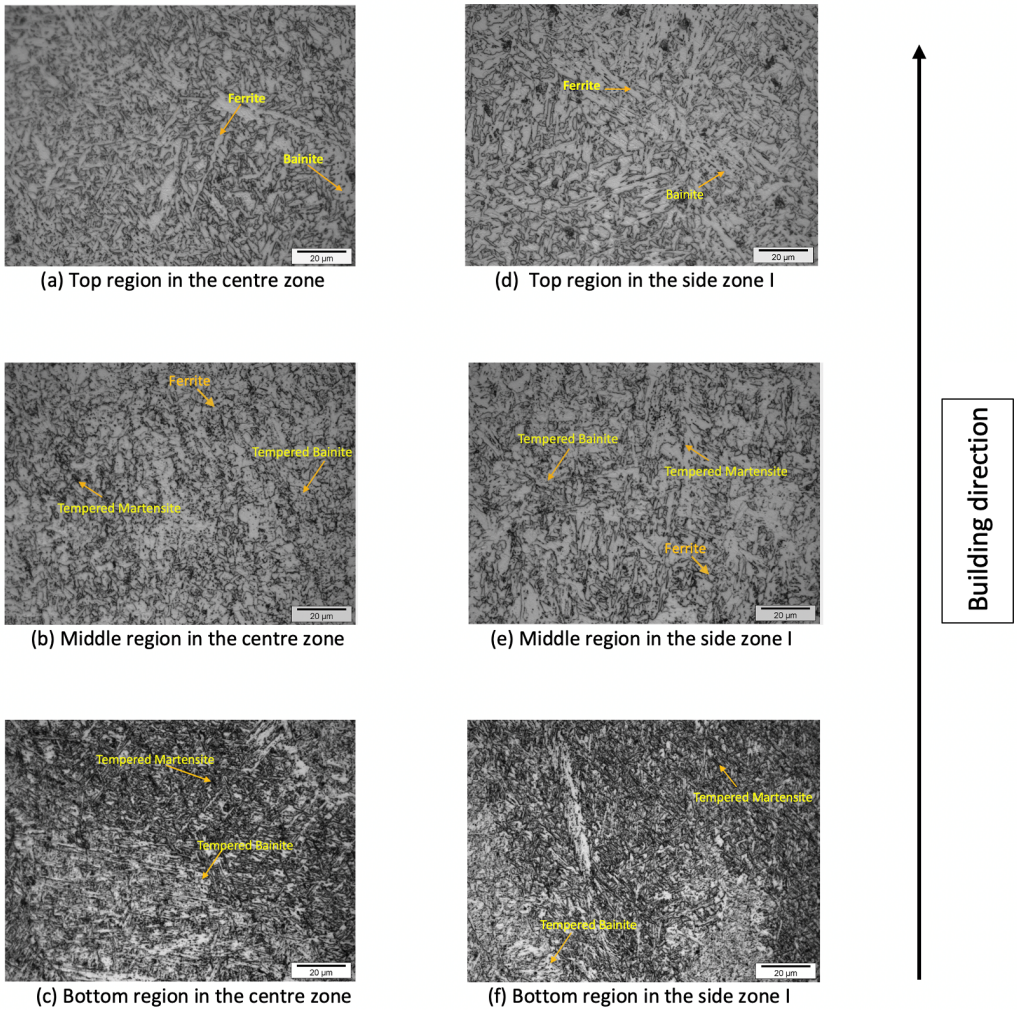

Figure 4.34: The microstructure of the different regions along the building direction of the crossing structure with the interlayer temperature 100 °C

According to Figure 4.33 and Figure 4.34, the grain size becomes coarser along the building direction, which accords with the result of thermal history of Figure 4.31, showing that the cooling rate decreases dramatically from bottom layer to top layer.

The discussions about the microstructures of the middle layers, the bottom layers, and the top layers in Figure 4.33 and Figure 4.34 are shown in the following three paragraphs.

(a) Figure 4.33(c), Figure 4.33(f), Figure 4.33(i), Figure 4.34(c) and Figure 4.34(f) show that in the bottom layer, tempered martensite and tempered bainite dominate the microstructure because of the high cooling rate in the bottom region (shown in Figure 4.31(a) and Figure 4.31(d)), caused by the cold substrate. The cold substrate is the critical factor that contributes to the very high cooling rate of the bottom layers, which leads to the similar microstructures occurring in different zones in the bottom region [72].

(b) Figure 4.33(b), Figure 4.33(e), Figure 4.33(h), Figure 4.34(b) and Figure 4.34(e) show a large amount of ferrite and tempered bainite as well as a small amount of tempered martensite formed in the middle layers

of the crossing structure, and this result agrees with Figure 4.31(b) and Figure 4.31(e), which display that the medium cooling rate occurs in the middle layers [3][72]. Moreover, the cooling rate in the centre zone is slightly higher than that in the side zone I (as mentioned previously) so the centre zone of the middle layers includes more martensite than the side zone I.

(c) Figure 4.33(a), Figure 4.33(d), Figure 4.33(g), Figure 4.34(a) and Figure 4.34(d) all illustrate the similar microstructures in the top layers, mainly including ferrite and bainite, and this result is in accord with the low cooling rates in the top layers shown in Figure 4.31(c) and Figure 4.31(f). Because the effect of the thermal accumulation increases along the building direction, the cooling rate becomes lowest in the top layers, which leads to more formation of ferrite [3][72].

According to Figure 4.33 and Figure 4.34, the crossing structures fabricated with the interlayer temperature of 100 °C and with the interlayer time of 90 sec have the similar microstructures. The possible reasons are discussed here: (a) When the crossing structure was intended to be fabricated with the interlayer temperature 100 °C, the interlayer temperature could be not controlled well at 100 °C. Because when this structure was being deposited, the temperature on the substrate, which was recorded by tracking point A, B, C, D, was taken as the interlayer temperature. However, the temperature in the substrate decreased faster than the temperature in the deposited crossing structure because of the high capacity for faster heat dissipation in the substrate and lower thermal accumulation in the substrate. Besides, because tracking point A, B, C, D are placed at a distance from the crossing structure, their temperature is much lower than the temperature of the crossing structure. Hence, in fact, the real interlayer temperature in the crossing structure could be much larger than 100 °C, which made the difference in the extent of the thermal accumulation between two structures become small, and made the difference of the cooling rates between two structures become too small to have different microstructures. (b) The interlayer time of 90 sec indeed has a higher extent of the thermal accumulation due to less time for thermal dissipation. However, with this extent of the thermal accumulation, the difference of the cooling rates between two structures could be still not high enough to lead to the obvious difference in microstructures. In other words, for achieving obvious difference in their microstructures, the interlayer time should be decreased further to increase the difference in the extent of the thermal accumulation between two structures.

Besides, it can be found that the result of microstructural characterization in Figure 4.33 and the prediction of the microstructure by the CCT diagram (shown in Figure 4.32) in previous section 4.4.2.2. are not totally same. The reason is explained below. Figure 4.32 is a conventional CCT diagram, which was produced by heating up the sample to a specific austenization temperature, keeping it at this temperature for a long time, and cooling the sample with various cooling rate. However, for the additive manufacturing, the austenization temperature changes in different thermal cycles. Besides, for the additive manufacturing, the material is only heated up and kept at the high temperature for austenization for a very short time (this time is also known as dwell time) [73].

Both the austenization temperature and the dwell time in austenization can affect the grain size of austenite. For example, either with the lower austenization temperature or the shorter dwell time, the size of austenite becomes smaller. The change in the grain size of austenite leads to the difference in the subsequent phase transformation during following cooling. For instance, austenite to ferrite transformation could be facilitated when the grain size of austenite becomes smaller. It is because the area of the grain boundary becomes more with smaller grain size, resulting in more sites for nucleation of ferrite [74]. Moreover, with short dwell time in austenization, the material possibly can not be fully austenized, leading to the inhomogeneous microstructure in the material [73]. Hence, based on these reasons, the difference between microstructure in Figure 4.33 and the microstructure predicted by CCT diagram exists.

Figure 4.35(a) and Figure 4.35(b) show the SEM images of the middle region (middle layers) of the crossing structure fabricated with the interlayer time of 90 sec. Figure 4.36(a) and Figure 4.36(b) show the SEM images of the middle region (middle layers) of the crossing structure fabricated with the interlayer temperature of 100 °C. These four images were taken at the different heights and zones of the middle region (middle layers) of the crossing structures, so the microstructure in four images underwent different thermal histories. Bainitic ferrite, martensite-retained austenite (MA), and martensite can be observed in Figure 4.35 and Figure 4.36. The distribution of MA is mainly along the grain boundary of bainitic ferrite, which is in accord with the description mentioned in Chapter 2, which describes that the formation of MA occurs at the grain boundary of bainitic ferrite and between bainite laths [22]. The different shapes of MA are observed in the forms of the blocky grains and stringers. Compared to blocky MA, stringer MA between bainitic ferrite is more easily debonded from the matrix. The connected MA network can initiate the local cleavage, which gives rise to a brittle behaviour [28]. However, according to Figure 4.35 and Figure 4.36, MA particles keep a distance between each other. Hence, even though some stringer MAs exist, they can not make the structure become very brittle because these stringer MAs are isolated [28].

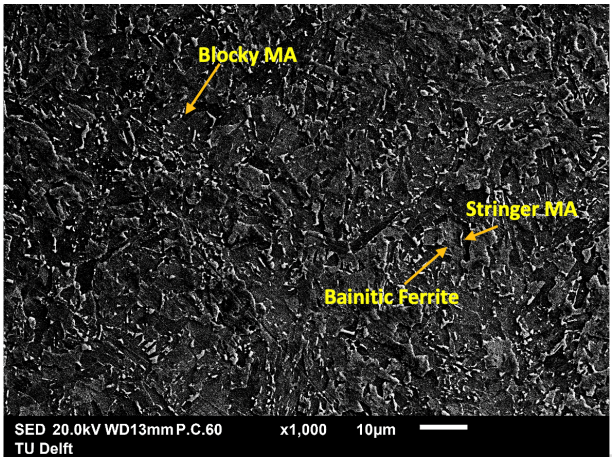

(a) the middle region in the centre zone

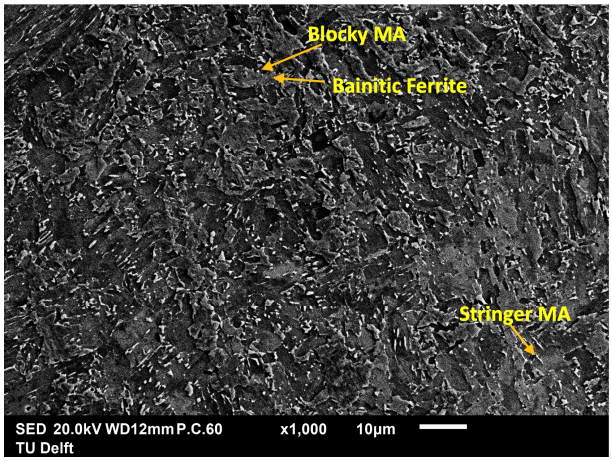

(b) the middle region in the side zone I

Figure 4.35: the SEM images of the crossing structure fabricated with interlayer time of 90 sec

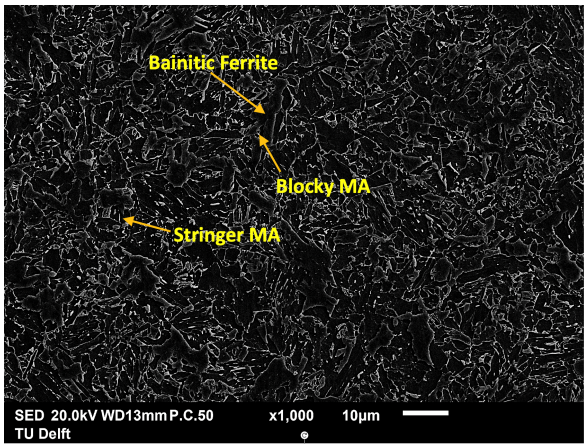

(a) the middle region in the centre zone

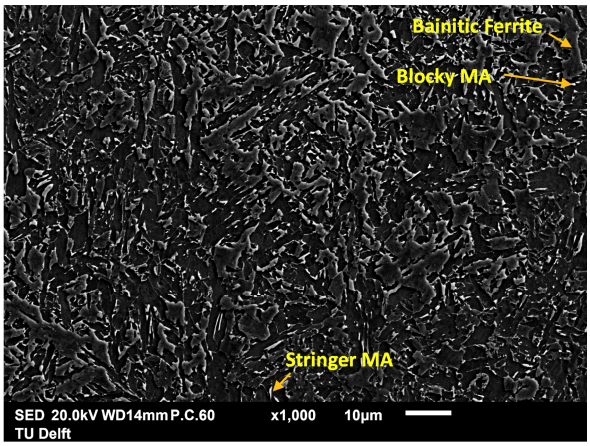

(b) the middle region in the side zone I

Figure 4.36: the SEM images of the crossing structure fabricated with interlayer temperature of 100 °C

Moreover, the formation of MA is caused by heating to the intercritical phase region and the subsequent cooling. During the process of cooling, partial austenite transforms to martensite to result in MA [26][27]. Cooling rate plays a key role for the size of MA. The austenite to martensite transformation needs higher cooling rate to be completed. If the cooling rate is not sufficient, partial austenite will decompose into ferrite or bainite. Hence, the size of MA will be smaller with a lower cooling rate because the formation of martensite decreases a lot [28][75].

According to Figure 4.35(a) and Figure 4.35(b), the sizes of MA in these two locations (these two images were taken at the different heights and zones) are similar, which means the cooling rates were similar in these two locations. Even though in the middle region, heat has more space to diffuse from the centre, the cooling rate of the centre zone at higher height still can be similar to the cooling rate of the side zone I at the lower height, which is caused by the more thermal accumulation at the higher height of the centre zone [28][75]. The size of MA in Figure 4.36(b) is larger than the size of MA in Figure 4.36(a). Thus, it can be inferred that the cooling rate at the location in Figure 4.36(b) is higher because of the bigger size of MA shown in Figure 4.36(b). Even though in the middle region, heat can transfer faster at the centre because of more space connected to the centre, the cooling rate of the centre zone still could be smaller than the cooling rate of the side zone I when the location at the centre is much higher than the location at the side zone I, leading to the much higher extent of thermal accumulation at the high location of the centre zone [28][75].

4.4.4. Hardness measurement

The results of hardness measurements for the centre zone, the side zone I, the side zone II (the locations of these zones are shown in previous Figure 4.22) of two crossing structures are illustrated in Figure 4.37. The hardness measurements were made from the bottom region to the top region of the crossing structures with a load of 1 Kg. Figure 4.37 shows that the hardness measurement from different zones in two structures are

similar. These results of hardness measurements are in accordance with the results of the microstructural characterization in chapter 4.4.3, which illustrates that different zones in two structures all show the similar microstructure.

According to Figure 4.37, the hardness in the bottom region is around 325 HV to 275 HV, and the hardness in both the middle region and the top region is around 250 HV. Hence, the order of the level of the hardness along the building direction is: Bottom region > Middle region ≈ Top region. The hardness of each region will be discussed with the microstructure and the thermal history below.

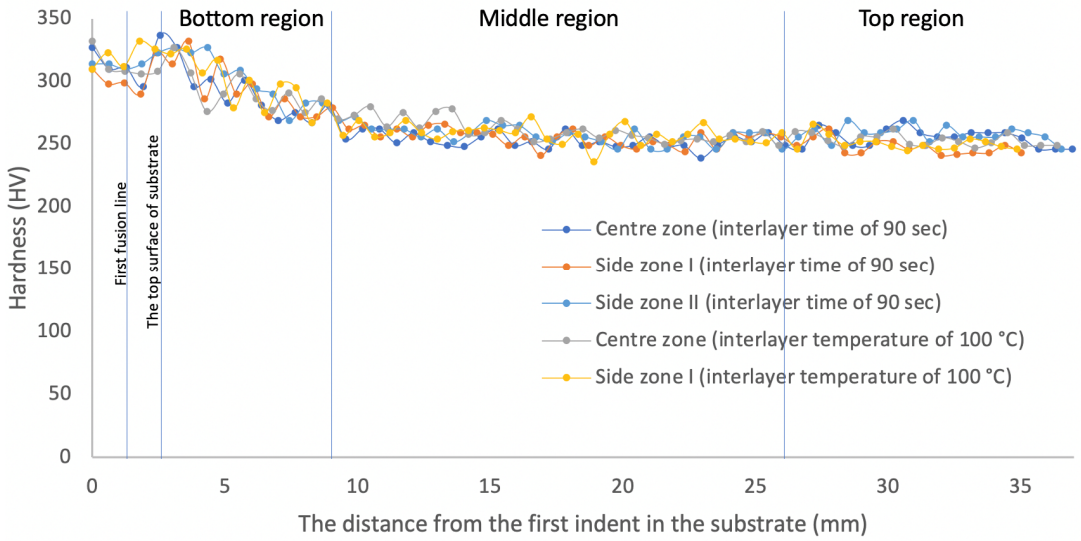

Figure 4.37: The hardness measurement of centre zone, side zone I, side zone II in two crossing structures

(a) Because the cold substrate strengthened the capacity for faster heat dissipation in the bottom regions, the material in bottom region underwent the highest cooling rate, which was even higher than 100 °C/s (shown in Figure 4.31(a)). With this high cooling rate, bainite and martensite dominate the microstructure, and after the following deposition process, the bainite and martensite got tempered [72]. As a result of higher fraction of martensite, the bottom region has the highest hardness in the structure [23]. The comparison of the hardness between the bottom region and other regions will be discussed in the following paragraphs.

(b) In the middle region (middle layers), a large amount of ferrite and bainite as well as a small amount of martensite were formed because of the reduced cooling rate, caused by the thermal accumulation [3]. In the middle region (middle layers), bainite and martensite also got tempered because of the subsequent deposition of the top region [72]. Compared to the bottom region, the amount of martensite in the middle region is lower, and ferrite as well as bainite occupy a large percentage of the area in the middle region. Hence, the hardness of the middle region is lower than that of the bottom region. Besides, Figure 4.33(b), Figure 4.33(e), Figure 4.34(b) and Figure 4.34(e) show that in the middle region (middle layers), more tempered martensite exists in the centre zone than the side zone I. However, according to Figure 4.37, in the middle layers, the

hardness results of the centre zone and the side zone I are still almost the same. The reason is that the centre zone underwent two passes of welding so there was more time for the material in the centre zone to get tempered. Hence, even if the phase fraction of martensite in the centre zone is more than that in the side zone I, the martensite in the centre has been tempered for a longer time to decrease the hardness level to be the same hardness level in the side zone I [72].

(c) When the top region of the crossing structure was being deposited, the extent of the thermal accumulation in the structure was already very high, which reduced the cooling rate further in the top region. Because of this lowest cooling rate in the top region, ferrite and bainite mainly occupy the microstructure. Besides, the amount of martensite observed in the middle layers is larger than that in the top layers but the hardness of the top layers and the middle layers are still similar. It is because the middle region includes the large amount of ferrite, and bainite as well as martensite in the middle layers have been tempered severely when the top region was being deposited. After tempering, the hardness in the middle region decreased further to become almost the same hardness level as the top region, which mainly has ferrite and bainite without tempering or with very short tempering time. Besides, the hardness in the top region is much lower than the hardness in the bottom region because the bottom region contains much more martensite due to its higher cooling rate [26][72].

To sum up, along the building direction, the bottom region is dominated by both tempered bainite and tempered martensite, the middle region has a large amount of ferrite and tempered bainite as well as a small amount of tempered martensite, and the top region mainly has ferrite and bainite without tempering or with very short tempering time. Hence, these different microstructures exist with various ratios in each region, which make the hardness level along the building direction become: Bottom region > Middle region ≈ Top region [3][72].

5 Conclusion and recommendation

5.1. Conclusion

According to the literature review, previous studies did not investigate the microstructure and mechanical properties of the low carbon steel in complex WAAM deposited structures. Hence, this thesis mainly researched the relationship between the process condition, the microstructural evolution and the hardness of the low carbon steel in complex structures fabricated by the WAAM process. The single bead is the first research topic in this report because it is the fundamental building block of complex structures. It was found that when the heat input decreased with a higher travel speed or a lower wire feed rate, the cooling rate became higher, leading to more martensite and less ferrite in the bead. The bead possessed higher hardness due to the increased amount of martensite. Besides, as the heat input became smaller, both the width and the height of the bead became small because less material was deposited per unit length with a smaller heat input.

The optimum process parameters for the best quality of multi-pass multi-layer structures were explored. The relationship between the process parameters, surface roughness, geometry of the structure and defect was also investigated. When the ratio of the wire feed rate to the travel speed was too small ($\leq$4.6), a depression was formed since the amount of feeding material was not enough to deposit the structure uniformly with the high travel speed. Besides, the step over increments were set to two-thirds of the width to improve the surface roughness. However, the surface quality could still be poor due to the error in the measurement of the bead width. When the appropriate heat input in the medium heat input zone was applied to deposit the structure, the structure can get more uniform geometry because the rising ends and tapered end have been improved. According to the result of the investigation, a wire feed rate 4.5 m/min and a travel speed 8 mm/s are the optimized process parameters to deposit the multi-pass multi-layer structure with the highest quality.

A functionally graded component was researched, and it was composed of three zones along the z-direction: a) High heat input zone I. b) Low heat input zone. c) High heat input zone II. The high heat input zones I, II were fabricated with higher heat input, resulting in a lower cooling rate, and the low heat input zone underwent a higher cooling rate because it was fabricated with lower heat input. The lower hardness in the high heat input zones I, II was due to more ferrite and bainite, caused by the lower cooling rate. The higher hardness in the low heat input zone was caused by more martensite in the microstructure as a consequence of the higher cooling rate. However, the microstructure in the low heat input zone was not homogeneous because of the occurrence of the softer white line region, which contained a large amount of ferrite. The formation of the ferrite in the white line was possibly caused by the nucleation of ferrite grains which could occur during the process of temperature heating up to the intercritical range, and the growth of ferrite grains

which could occur when the temperature achieved intercritical range. Besides, recrystallization and grain growth of ferrite also could occur when the temperature achieved to about 500°C to 700°C.

The thermal history, the microstructure, and the mechanical properties of the crossing structures were explored. The crossing structures respectively fabricated with the interlayer temperature of 100 °C and the interlayer time of 90 sec showed a similar microstructures and hardness. In the bottom region, both tempered bainite and tempered martensite dominated the microstructure due to the cold substrate. In the middle layers, a large amount of ferrite and tempered bainite as well as a small amount of tempered martensite were formed because of the medium cooling rate, caused by the medium thermal accumulation. Besides, in the middle layers, compared to the side wall, the higher cooling rate at the centre can be observed, and it is because the heat can diffuse from the centre to four connected walls, which gave the heat produced at the centre more area to transfer. According to SEM images of the middle layers, isolated MA islands in the forms of the blocky grains and stringers can be observed. In the top region, ferrite and bainite without tempering or with very short tempering time mainly existed in the microstructure due to the lowest cooling rate, caused by the greatest extent of the thermal accumulation. Due to the varying microstructure from the bottom region to the top region, the hardness level along the building direction became: Bottom region > Middle region ≈ Top region.

5.2. Recommendation

In this research, some questions still remain unresolved, and some suggestions for further investigation are recommended below. The mechanical properties of the crossing structures and the functionally graded component were only explored by the hardness test. If other mechanical tests can be applied to these structures, the relationship between heat input, microstructure, and mechanical properties can be understood more completely. For example, tensile test can be used to acquire tensile strength, yield strength, and ductility. Charpy impact test also can be used to measure the toughness. Besides, for exploring the microstructure further, other techniques can be utilized. For example, EBSD measurement can be used to investigate the orientation of the grains in these structures.

The crossing structure was intended to be fabricated with the interlayer temperature of 100 °C in the experiment. However, the interlayer temperature could be not controlled well at 100 °C. If the interlayer temperature can be controlled accurately by measuring the temperature of the top surface of the structure, the recorded thermal history should be more accurate and reliable. Besides, the crossing structures fabricated with the interlayer temperature of 100 °C and with the interlayer time of 90 sec had the similar microstructures. It should be interesting to see if the obvious difference could occur in the microstructure if the interlayer time is further decreased, and the effect of thermal accumulation can be understood further.

There are still other structures fabricated by WAAM worth exploring further. For instance, circle and T-shape. These structures have not been investigated with respect to their microstructure and mechanical

properties. As mentioned before, for applying these structures in various applications, it is important to understand the relationship between process conditions, microstructure, and mechanical properties of these structures.

Bibliography

[1] T. DebRoy, H.L. Wei, J.S. Zuback, T. Mukherjee , J.W. Elmer, J.O. Milewski, A.M. Beese, A. Wilson-Heid, A. De, W. Zhang, Additive manufacturing of metallic components – Process, structure and properties, Progress in Materials Science 92, 112–224, 2018.

[2] The 7 Categories of Additive Manufacturing. URL https://www.manufacturingglobal.com/smart-manufacturing/7-categories-additive-manufacturing

[3] Tiago A. Rodrigues, V. Duarte, Julian A. Avila, Telmo G. Santos, R.M. Miranda, J.P. Oliveira, Wire and arc additive manufacturing of HSLA steel: Effect of thermal cycles on microstructure and mechanical properties, Additive Manufacturing 27, 440–450, 2019.

[4] Praxair Shielding Gases - Technical Manuals, 1998.

[5] Wikipedia. Gas tungsten arc welding. URL https://en.wikipedia.org/wiki/Gas_tungsten_arc_welding

[6] K. F. Chung. Structural effects of welding onto high strength S690 steel plates and welded sections, Hong Kong Polytechnic University, DEPARTMENT OF CIVIL AND ENVIRONMENTAL ENGINEERING, thesis for the Degree of Doctor of Philosophy, 3–4, 2017.

[7] S690 Welding Factory. URL http://www.nironstaal.nl/facilities/S690-Welding-Factory

[8] L. Pezzato, C. Gennari, D. Chukin, M. Toldo, F. Sella, M. Toniolo, A. Zambon, K. Brunelli, M. Dabalà. Study of the Effect of Multiple Tempering on the Impact Toughness of Forged S690 Structural Steel, Metals, 10, 507, 2020.

[9] H. Ho, K. Chung, M. Huang, D. A. Nethercot , X. Liu, H. Jin, G. Wang, Z. Tian. Mechanical properties of high strength S690 steel welded sections through tensile tests on heat-treated coupons, Journal of Constructional Steel Research 166, 105922, 2020.

[10] J. Mehnen, J. Ding, H. Lockett, P. Kazanas. Design study for wire and arc additive manufacture. Int. J. Product Development , 2–19, 2014.

[11] N. Knezović, A. Topić, Wire and Arc Additive Manufacturing (WAAM) – A New Advance in Manufacturing, Springer International Publishing AG ,65–71, 2019.

[12] G. Venturini, F. Montevecchi, A. Scippa, G. Campatelli, Optimization of WAAM deposition patterns for T-crossing features, Procedia CIRP 55, 95–100, 2016.

[13] Montevecchi F, Grossi N, Takagi H, Scippa A, Sasahara H, Campatelli G. Cutting force analysis in additive manufactured AISI H13 alloy. Procedia CIRP 46:476–479, 2016.

[14] H. Geng, J. Li, J. Xiong, X. Lin, and F. Zhang, Geometric Limitation and Tensile Properties of Wire and Arc Additive Manufacturing 5A06 Aluminum Alloy Parts, JMEPEG 26:621–629, 2017.

[15] M. Rafieazad, M. Ghaffari, A. V. Nemani, A. Nasiri, Microstructural evolution and mechanical properties of a low-carbon low-alloy steel produced by wire arc additive manufacturing, The International Journal of Advanced Manufacturing Technology 105:2121–2134, 2019.

[16] V.N. Lazić, A.S. Sedmak, M.M. Živković, S.M. Aleksandrović, R.D. Čukić, R.D. Jovičić, I.B. Ivanović, Theoretical-experimental determining of cooling time (t8/5) in hard facing of steels for forging dies, Therm. Sci. 14 235–246, 2010.

[17] Y. Shi, Z. Han, Effect of weld thermal cycle on microstructure and fracture toughness of simulated heat-affected zone for a 800 MPa grade high strength low alloy steel, J. Mater. Process. Technol. 207 30–39, 2008.

[18] S.S. Babu, The mechanism of acicular ferrite in weld deposits, Curr. Opin. Solid State Mater. Sci. 8 267–278, 2004.

[19] C. Capdevila, F.G. Caballero, C.G. de Andrés, Determination of Ms temperature in steels: a Bayesian neural network model, ISIJ Int. 42 894–902, 2002.

[20] S.W. Thompson, D.J. Vin Col, G. Krauss, Continuous cooling transformations and microstructures in a low-carbon, high-strength low-alloy plate steel, Metall. Trans. A 21,1493–1507, 1990.

[21] Haden CV, Zeng G, Carter FM et al Wire and arc additive manufactured steel: tensile and wear properties. Addit Manuf 6: 115–123, 2017.

[22] F.G.Caballero, Phase Transformations in Steels, Chapter 12, 436 – 467, 2012.

[23] H. Bhadeshia, R. Honeycombe, Steels: Microstructure and Properties 4th Edition, 2017.

[24] Wikipedia. Bainite. URL https://en.wikipedia.org/wiki/Bainite

[25] H. Bhadeshia, Encyclopedia of Materials: Science and Technology (Second Edition), 1 – 7, 2001.

[26] L. Sun, F. Jiang, R. Huang, D. Yuan, C. Guo, J. Wang, Microstructure and Mechanical Properties of Low-Carbon High-Strength Steel Fabricated by Wire and Arc Additive Manufacturing, Metals, 10, 216, 2020.

[27] N. Sridharana, M. W. Noakesb, A. Nyczb, L. J. Loveb, R. R. Dehoffa, S. S. Babu, On the toughness scatter in low alloy C-Mn steel samples fabricated using wire arc additive manufacturing, Materials Science & Engineering A 713, 18–27, 2018.

[28] C. L. Davis, J. E. King, Effect of cooling rate on intercritically reheated microstructure and toughness in high strength low alloy steel, Materials Science and Technology, Vol.9, 8–15, 1993.

[29] Particle Analytical, Analysis for the Pharmaceutical Industry. URL https://particle.dk/methods-analytical-laboratory/xrd-analysis/

[30] K. Wallin, Upper shelf energy normalisation for sub-sized charpy-V specimens, Int. J. Press. Vessel. Pip. 78, 463–470, 2001.

[31] J. González, I. Rodríguez, J-L.Prado-Cerqueira, J.L.Diéguez, A.Pereira. Additive manufacturing with GMAW welding and CMT technology. Procedia Manufacturing, Volume 13, 840–847, 2017.

[32] S. Suryakumar, K. P. Karunakaran, A. Bernard, U. Chandrasekhar, N. Raghavender, D. Sharma, Weld bead modeling and process optimization in Hybrid Layered Manufacturing, Computer-Aided Design 43, 331–344, 2011.

[33] Wikipedia. Functionally graded material. URL https://en.wikipedia.org/wiki/Functionally_graded_material

[34] H. Gao, Residual Stress Development due to High-Frequency Post Weld Impact Treat- ments for High-Strength Steels, 2014.

[35] G. D. Ouden, M. Hermans, Welding Technology, 2009.

[36] S.C. Gupta S.C. Gupta, The Classical Stefan Problem 1st Edition, Volume 45, 1–38, 2003.

[37] J. Ding, P. Colegrove, J. Mehnen, S. Ganguly, P. M. Almeida, F. Wang, and S. Williams, Thermo-mechanical analysis of Wire and Arc Additive Layer Manufacturing process on large multi-layer parts, Computational Materials Science, vol. 50, no. 12, 3315–3322, 2011.

[38] J. Goldak, C. Aditya, and M. Bibby, A New Finite Element Model for Welding Heat Sources, Metallugical Transactions B, vol. 15B, no. 1, 299–305, 1984.

[39] M. Graf, A. Hälsig, K. Höfer, B. Awiszus, and P. Mayr, Thermo-mechanical modelling of wire-arc additive manufacturing (WAAM) of semi-finished products, Metals, vol. 8, no. 12, 2018.

[40] F. Montevecchi, G. Venturini, N. Grossi, A. Scippa, and G. Campatelli, Finite Element mesh coarsening for effective distortion prediction in Wire Arc Additive Manufacturing, Additive Manufacturing, vol. 18, 145–155, 2017.

[41] J. Ding, P. Colegrove, J. Mehnen, S. Williams, F. Wang, and P. S. Almeida, A computa- tionally efficient finite element model of wire and arc additive manufacture, International Journal of Advanced Manufacturing Technology, vol. 70, no. 1-4, 227–236, 2014.

[42] Q. Wu, J. Lu, C. Liu, H. Fan, X. Shi, J. Fu, and S. Ma, Effect of molten pool size on microstructure and tensile properties of wire arc additive manufacturing of Ti-6Al-4V alloy, Materials, vol. 10, no. 7, 1–11, 2017.

[43] Z. Nie, G. Wang, J. D. McGuffin-Cawley, B. Narayanan, S. Zhang, D. Schwam, M. Kottman, and Y. Rong, Experimental study and modeling of H13 steel deposition us- ing laser hot-wire additive manufacturing, Journal of Materials Processing Technology, vol. 235, 171–186, 2016.

[44] Keyence. Microscope Glossary. URL https://www.keyence.com/ss/products/microscope/glossary/cat1/digital_microscope/

[45] Medical Device Testing Services Incorporated, Optical Microscopy vs. Scanning Electron Microscopy: How Scanning Electron Microscopy Can Take Your Medical Device Inspections to the Next Level, Medical Device Testing Services. URL https://devicetesting.com/index.cfm

[46] Newage Testing Instruments. Vickers Hardness Testing. URL https://www.hardnesstesters.com/test-types/vickers-hardness-testing

[47] Gordon England. Vickers Hardness Test. URL https://www.gordonengland.co.uk/hardness/vickers.htm

[48] J. Norrish, Recent gas metal arc welding (GMAW) process developments: the implications related to international fabrication standards, Weld World 61:755–767, 2017.

[49] C. S. Wu, M. A. Chen and Y. F. Lu. Effect of current waveforms on metal transfer in pulsed gas metal arc welding, Meas. Sci. Technol. 16, 2459–2465, 2005.

[50] P.K. Palani, N. Murugan. Selection of parameters of pulsed current gas metal arc welding, Journal of Materials Processing Technology 172, 1–10, 2006.

[51] Welding Parameters and Techniques. URL https://www.esabna.com/euweb/mig_handbook/592mig7_1.htm

[52] G. Cui, H. Guo, S. Yang, X. He, Influence of interface between grain boundary ferrite and prior austenite on bainite transformation in a low carbon steel, Acta Metall Sin ,680–686, 2009

[53] X. Zhou, J. Dong, Y. Liu, C. Liu, L. Yu, Y. Huang, H. Li, Austenite to polygonal-ferrite transformation and carbide precipitation in high strength low alloy steel, Int. J. Mater. Res. (formerly Z. Metallkd.) 108, 12–19, 2017.

[54] ZYGO, Mx^{TM} Surface Texture Parameters, 2018.

[55] D. Ding, Z. Pan, D. Cuiuri, H. Li, Wire-feed additive manufacturing of metal components: technologies, developments and future interests, Int J Adv Manuf Technol 81:465–481, 2015.

[56] Rahul, H. K. Arya, R. K. Saxena, Effect of Cooling Rate on Microstructure of Saw Welded Mild Steel Plate (Grade C 25 as Per IS 1570), IJMER, 222–228, 2014.

[57] C. Su, X. Chen, C. Gao, Y. Wang. Effect of heat input on microstructure and mechanical properties of Al-Mg T alloys fabricated by WAAM. Applied Surface Science 486, 431–440, 2019.

[58] EWI. Gas metal arc welding basics: Welding current & welding voltage. URL https://ewi.org/gas-metal-arc-welding-basics-welding-current-welding-voltage/

[59] S. Kuo, Y. Le, Nucleation Mechanisms and Grain Refining of Weld Metal, WELDING RESEARCH SUPPLEMENT, 305–313, 1986.

[60] V. Villaret, F. Deschaux-Beaume, C. Bordreuil, A solidification model for the columnar to equiaxed transition in welding of a Cr-Mo ferritic stainless steel with Ti as inoculant, Journal of Materials Processing Technology, Elsevier, 233, 115–124, 2016.

[61] E. K. Hamd, A. S. Alwan, I. K. Irthiea, Study the Effect of Welding Heat Input on the Microstructure, Hardness, and Impact Toughness of AISI 1015 Steel, Al-Khwarizmi Engineering Journal, Vol. 14, No. 1, 118–127, 2018.

[62] BODYCOTE-Heat treatment. URL https://www.bodycote.com/services/heat-treatment/

[63] H. Fredriksson, Mechanism of grain growth in metals, Materials Science and Technology, Vol. 6, 811–817, 1990.

[64] T. Shintani, Y. Murata, Evaluation of the dislocation density and dislocation character in cold rolled Type 304 steel determined by profile analysis of X-ray diffraction, Acta Materialia 59, 4314–4322, 2011.

[65] Wikipedia. Grain growth. URL https://en.wikipedia.org/wiki/Grain_growth

[66] J. R. Weertman, Hall-Petch strengthening in nanocrystalline metals, Materials Science and Engineering, A 166, 161–167, 1993.

[67] S. Jun, O. Kochan, Investigations of Thermocouple Drift Irregularity Impact on Error of their Inhomogeneity Correction, MEASUREMENT SCIENCE REVIEW, Volume 14, No. 1, 29–34,2014.

[68] Six Common Causes for Thermocouple Temperature Measurement Errors. URL https://blog.wika.us/products/temperature-products/six-common-causes-thermocouple-temperature-measurement-errors/

[69] Wikipedia. Thermocouple. URL https://en.wikipedia.org/wiki/Thermocouple#Aging_of_thermocouples

[70] J. LEE, J. K. CHEN, Y. T. PAN, K. C. HSIEH, Evaluation of Transformation Latent Heat in C-Mn Steels, ISIJ International, Vol. 39, No. 3, 281–287, 1999.

[71] Wikipedia. Latent Heat. URL https://en.wikipedia.org/wiki/Latent_heat

[72] Y. Ali, P. Henckell, J. Hildebrand, J. Reimann, J.P. Bergmann, S. Barnikol-Oettler, Wire arc additive manufacturing of hot work tool steel with CMT process, Journal of Materials Processing Tech. 269, 109–116, 2019.

[73] M.Maalekian, M.L.Lendinez, E.Kozeschnik, H.P. Brantner and H.Cerjak, The Influence of Peak Temperature and Deformation on Welding CCT Diagram of Eutectoid Carbon Steel, Advanced Materials Research, Vols 15-17, 1008–1013, 2007.

[74] M. SHOME and O.N. MOHANTY, Continuous Cooling Transformation Diagrams Applicable to the Heat-Affected Zone of HSLA-80 and HSLA-100 Steels, METALLURGICAL AND MATERIALS TRANSACTIONS, VOLUME 37A, 2159–2169, 2006.

[75] X. Di, L. Cai, X. Xing, C. Chen, Z. Xue, Microstructure and Mechanical Properties of Intercritical Heat-affected Zone of X80 Pipeline Steel in Simulated In-Service Welding, Acta Metall. Sin. (Engl. Lett.), 2015.